DISSERTATION

NONLINEAR SPIN WAVES IN MAGNETIC THIN FILMS – FOLDOVER, DISPERSIVE SHOCK WAVES, AND SPIN PUMPING

Submitted by

Pasdunkorale Arachchige Praveen Janantha

Department of Physics

In partial fulfillment of the requirements

For the Degree of Doctor of Philosophy

Colorado State University

Fort Collins, Colorado

Fall 2016

Doctoral Committee:

Advisor: Mingzhong Wu

Richard Eykholt
Mario Marconi
Carl Patton

ABSTRACT

NONLINEAR SPIN WAVES IN MAGNETIC THIN FILMS – FOLDOVER, DISPERSIVE SHOCK WAVES, AND SPIN PUMPING

Three nonlinear phenomena of spin waves and the spin Seebeck effect in yttrium iron garnet (YIG)/Pt bi-layer structures are studied in this thesis and are reported in detail in Chapters 4-7.

In the fourth chapter, the first observation of foldover effect of nonlinear eigenmodes in feedback ring systems is reported. The experiments made use of a system that consisted of a YIG thin film strip, which supported the propagation of forward volume spin waves, and a microwave amplifier, which amplified the signal from the output of the YIG strip and then fed it back to the input of the strip. The signal amplitude vs. frequency response in this ring system showed resonant peaks which resulted from ring eigenmodes. With an increase in the resonance amplitude, those resonant peaks evolved from symmetric peaks to asymmetric ones and then folded over to higher frequencies. The experimental observations were reproduced by theoretical calculations that took into account the nonlinearity-produced frequency shift of the traveling spin waves.

The fifth chapter presents the first experimental observation of the formation of envelope dispersive shock wave (DSW) excitations from repulsive nonlinear spin waves. The experiments used a microwave step pulse to excite a spin-wave step pulse in a YIG thin film strip, in which the spin-wave amplitude increases rapidly. Under certain conditions, the spin-wave pulse evolved into a DSW excitation that consisted of a train of dark soliton-like dips with both the dip width

and depth increasing from the front to the back and was terminated by a black soliton that had an almost zero intensity and a nearly 180° phase jump at its center.

The sixth chapter reports on the spin pumping due to traveling spin waves. The experiment used a micron-thick YIG strip capped by a nanometer-thick Pt layer. The YIG film was biased by an in-plane magnetic field. The spin waves pumped spin currents into the Pt layer, and the later produced electrical voltages across the length of the Pt strip through the inverse spin Hall effect (ISHE). Several distinct pumping regimes were observed and were interpreted in the frame work of the nonlinear three-wave splitting processes of the spin waves.

The seventh chapter presents the first experimental work on the roles of damping in the spin Seebeck effect (SSE). The experiments used YIG/Pt bi-layered structures where the YIG films exhibited very similar structural and static magnetic properties but very different damping. The data indicate that a decrease in the damping of the YIG film gives rise to an increase in the SSE coefficient, and this response shows quasi-linear behavior. The data also indicate that the SSE coefficient shows no notable dependences on the enhanced damping due to spin pumping.

ACKNOWLEDGEMENTS

I would like to sincerely thank my advisor Professor Mingzhong Wu for his support and guidance throughout the graduate studies. My special appreciation is also extended to Professor Boris Kalinikos. Both Professor Wu and Professor Kalinikos spent countless hours doing experiments and discussing ideas with me and answering my questions. If not for their mentoring, the completion of this thesis would have not been possible.

I would like to thank Professor Richard Eykholt and Professor Carl Patton for their support and many discussions that have provided me with invaluable insights about the experiments. I would like to thank Professor Mark Hoefer for his collaboration and support with the theory of dispersive shock waves. I deeply acknowledge Robert Adame for his generous support at the machine shop. My appreciation also extends to Zihui Wang, Yiyan Sun, Lei Lu, Aaron Hagerstrom, Leif Anderson, Young-Yeal Song, Michael Kabatek, Houchen Chang, David Ellsworth, Tao Liu, Daniel Richardson, Jinjun Ding, Jason Liu, Grant Riley, Martin Asmat, and Demann August. Their knowledge, experiences, and skills were very valuable to me and I am grateful to the good friendships which we established during the graduate studies. I also acknowledge the help from undergraduate students Kevin Cline, Ryan Whitcomb, Taylor Thomas, and Bryan Johnson and high-school student Joseph Gelfand. I greatly appreciate the support from Wendy Johnson and Veronica Nicholson on administrative work and keeping me on track during the seven years of graduate school. I thank Colorado State University and the Department of Physics for giving me the opportunity to peruse my Ph.D. program.

Lastly, but certainly not least, I would like to extend my heartfelt gratitude and appreciations to my parents and dearest friends for believing in me. Without their constant support and kindness I wouldn't be where I am today.

TABLE OF CONTENTS

CHAPTER 1

Overview

1.1 Background and Motivations

Started maybe with the observation of simple waves on water traveling as ripples, human curiosity has expanded its knowledge on wave dynamics to extraordinary levels, stretching from the understanding of simple water waves to quantum mechanics and beyond. Yet the branch of nonlinear wave dynamics stays rich and full of new possibilities for discovery. Because of the wide range of nonlinear and dispersion properties that can be explored, spin waves excited in YIG films provide an excellent test bed for the study of nonlinear wave dynamics. Here the extremely low damping in the YIG plays a very important role. Thanks to the absence of conduction electrons and Fe^{2+} ions, magnetic garnets have slower ferromagnetic relaxation rates[1,2] among which, YIG and doped YIG materials have the lowest. This made Dr. Kittel to refer to YIG as the fruit fly of magnetism. Due to low damping, spin waves in YIG films can travel up to tens of millimeters while in most of the other materials they decay within few micrometers.

[1] B. Lax and K. J. Button, *Microwave Ferrites and Ferrimagnetics* (McGraw-Hill, New York, 1962).
[2] Y. Sun, *Yttrium Iron Garnet nano Films: Epitaxial Growth, Damping, Spin Pumping, and Magnetic Proximity Effect*, Ph.D. thesis (Colorado State university, Fort Collins, 2014).

Starting from 1960's, spin waves in YIG have been studied extensively. This includes the study of phenomena such as modulational instability,[3] envelope bright solitons,[4] envelope dark solitons,[5] chaotic soliton trains,[6] and soliton fractals,[7] among others.

As much as spin waves are attractive to the fundamental studies of nonlinear wave dynamics, spin waves in YIG films have also proven their versatility in device applications as well. This includes microwave devices such as nonlinear power limiters,[8] signal to noise enhances,[9,10] nonlinear interferometers,[11] and more. Another branch with new possibilities is the use of spin waves in so-called spintronic devices. In 2010, for the first time the successful transfer of an electrical signal with YIG films[12] and the spin Seebeck effects (SSE) in YIG materials[13] were demonstrated.[2] The main idea behind spintronics is to merge the spin dynamics with electronics. While devices such as magnetic random access memory (MRAM) have already entered the market, logic and computational devices that are based on spin waves are still under development.[14] In these devices, logic operations and computations are carried out by spin waves. For example, one can excite spin waves by different sources and detect their interference patterns which change

[3] M. Wu, A. M. Hagerstrom, R. Eykholt, A. Kondrashov, and Boris A. Kalinikos, Phys. Rev. Lett. **102**, 237203 (2009).
[4] M. M. Scott, B. A. Kalinikos, and C. E. Patton, Appl. Phys. Lett. **78**, 970 (2001).
[5] M. Chen, M. A. Tsankov, J.M. Nash, and C. E. Patton, Phys. Rev. Lett. **70**, 1707 (1993).
[6] A. B. Ustinov, V. E. Demidov, A. V. Kondrashov, B. A. Kalinikos, and S. O. Demokritov Phys. Rev. Lett. **106**, 017201 (2011).
[7] M. Wu, B. A. Kalinikos, L. D. Carr, and C. E. Patton, Phys. Rev. Lett. **96**, 187202 (2006).
[8] C. S. Philip, C. A. Robert, US Patent 3,500,256, (1970).
[9] T. Nomoto and Y. Matsushita, IEEE Trans. Microwave Theory Tech. **41**, 1316 (1993).
[10] J.D. Adam, IEEE Trans on magnetics. **16**, 5 (1980).
[11] A. B. Ustinov, B. A. Kalinikos, Tech. Phs. Lett. **5**, 403 (2001).
[12] Y. Kajiwara, K. Harii, S. Takahashi, J. Ohe, K. Uchida, M. Mizuguchi, H. Umezawa, H. Kawai, K. Ando, K. Takanashi, S. Maekawa, and E. Saitoh, Nature. **464**, 262 (2010).
[13] K. Uchida, J. Xiao, H. Adachi, J. Ohe, S. Takahashi, J. Leda, T. Ota, Y. Kajiwara, H. Umezawa, H. Kawai, G. E. W. Bauer, S. Maekawa, and E. Saitoh, Nature Materials. **9**, 894 (2010).
[14] A. V. Chumak, V. I. Vasyuchka, A. A. Serga and B. Hillebrands, Nature Physics. **11**, 453 (2015).

with the phases of the initial spin waves.[11] Therefore, a growing interest to study and use spin waves in low damping garnets like YIG, for spintronic applications, is also immerging.

The motivation behind the work presented in this thesis is twofold. First, the study of nonlinear dynamics of spin waves is far more than complete and there are many new phenomena that need to be studied. Spin waves in YIG thin films provide a unique system to study some of this nonlinear phenomena. Spin waves excited in YIG films typically operate in the GHz frequency range, which is accessible with fast oscilloscopes, and some of the nonlinear phenomena, such as solitons and dispersive shock waves, occur as the slowly varying envelopes of the spin waves. This enables one to study both the envelope and phase of the carrier wave at the same time. The previous studies of bright and dark solitons are one excellent example. This thesis reports the first experimental observation of two intriguing nonlinear phenomena in spin wave systems, and develops a complete mathematical description for one of them. Second, the YIG/Pt bi-layer structures have proven to be of great importance in spintronic applications. Spin pumping in this bi-layer structure, due to traveling spin wave and other excitations, is still not fully understood. The work presented in this thesis makes the attempt to better understand the spin pumping process in YIG/Pt bi-layers.

1.2 Dissertation Organization

This thesis is organized into eight chapters. The next two chapters present the introductory materials. Chapter 2 gives an introduction to linear and nonlinear spin waves and presents the mathematical description of spin waves. This chapter also introducers the spin wave

experimental setup that was used for the experiments. Chapter 3 introduces the key ideas behind the spin Hall effect, the inverse spin Hall effect (ISHE), spin pumping, and the spin Seebeck effect (SSE). The experimental setups that had been used for the ISHE voltage and the SSE voltage are also described. Chapter 4 presents the experimental work on the foldover of nonlinear eigenmodes in a YIG thin film-based feedback ring and develops the complete mathematical description of it. Chapter 5 presents the first observation of envelope dispersive shock waves in a YIG strip supporting surface spin waves. Chapter 6 presents the spin pumping due to travelling spin waves and explains the observed data under the frame work of so-called nonlinear three-wave interactions. Chapter 7 presents a study on the SSE, where the role of damping in the SSE strength in YIG thin films is studied.

CHAPTER 2

Spin Waves

The goal of this chapter is to provide the necessary background knowledge and introduce the mathematical description of spin waves in magnetic thin films. The chapter is organized into two main sections. In section 2.1, a detailed description of spin waves will be presented, such as the mathematical description of dispersion relations and nonlinearity coefficients for different types of spin waves. Section 2.2 will introduce the experimental setups that were used for the work presented in the later chapters. The materials presented here depend heavily on the text book of Stancil and Prabahkar,[15] the book chapter by Prof. M. Wu,[16] and M. Scott's Ph.D. thesis.

In the macroscopic semi-classical picture, the idea of a magnetic moment can be treated as the starting point of the treatment of spin waves. If one considers an atom from a classical physics stand point, the electrons that orbit the nuclei in a circular path are the elementary particles that give rise to the magnetic properties of the atom, and thereby to the material of which it's a constituent. An electron that orbits the nuclei can be treated as a small current loop. While the electron itself possesses an intrinsic spin angular moment which is of quantum mechanical origin, the resultant total magnetic moment of an atom is the combination of the two. The total magnetic dipole moment of the atom can be written as[17]

[15] D. D. Stancil and A. Prabhakar, *Spin Waves – Theory and Applications* (Springer, New York, 2009).
[16] M. Wu, in *Solid State Physics*, edited by R. Camley and R. Stamps (Academic Press, Burlington, MA, 2011).
[17] J. R. Hook and H. E. Hall, *Solid State Physics* (Wiley, Norfolk, 2006).

$$\boldsymbol{\mu} = -\mu_{\mathrm{B}}(\mathbf{L} + 2\mathbf{S})/\hbar \tag{2.1}$$

where L is the orbital angular momenta, S is the spin angular momenta of the electrons in the atom, and μ_{B} Bohr magneton. In transition metals the **L** is quenched and has very little contribution to **μ**.[15]

If one considers an unbounded magnetic material that is composed of such atoms, the magnetization vector of such a magnetic material can be considered as the density of the individual atomic magnetic moments and can be written as

$$\mathbf{M} = \frac{1}{\Delta V}\sum_{\Delta V}\boldsymbol{\mu} \tag{2.2}$$

where ΔV represents a small volume of the said unbounded magnetic material. When such a magnetic material is subject to an external magnetic field **H**, the magnetic moments and therefore the magnetization tend to align with the field. The potential energy of the magnetization in such a situation is given by

$$E = -\mathbf{M} \cdot \mathbf{H} \tag{2.3}$$

Therefore, the potential energy of the magnetization is a minimum when the magnetization is aligned with the field.

However, if the magnetization is deviated away from this equilibrium direction, a torque is exerted on it, which will drive it to precess around its equilibrium. This precessional motion is depicted pictorially in Fig. 2.1. In this figure, **M** is the magnetization vector, $\mathbf{M_z}$ is the z component of the magnetization, **m** is the dynamical component of the magnetization under precession, and the set of axis is defined such that the applied magnetic field **H** is along the z

direction. The precession of the magnetic moment is counter-clockwise when viewed from the top.

For circular precession the z component of the magnetization can be written in the following form $M_z = \sqrt{M^2 - m^2}$. This can be expanded as follows for small precessional angles where m is small.

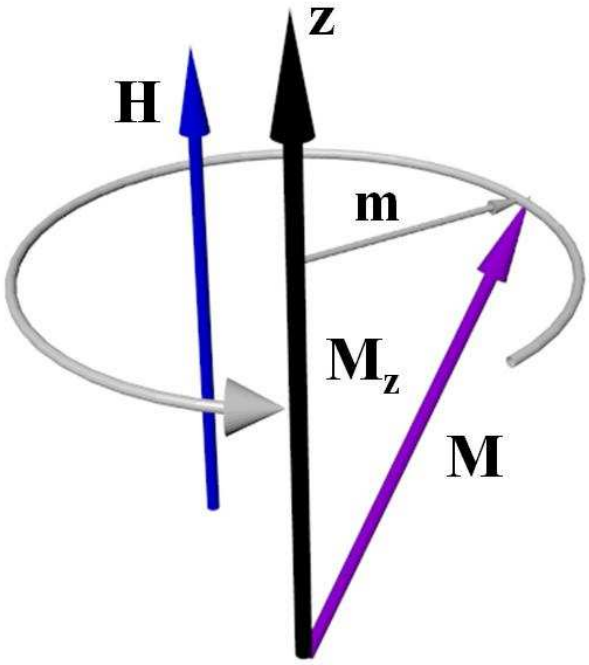

Figure 2.1 Schematic representation of magnetization precession in a uniform static magnetic field. The magnetization and magnetic field vectors are illustrated by the arrows labeled **M** and **H**, respectively.

$$M_z = M\left(1 - \frac{m^2}{2M^2} + \cdots\right) = M(1 - |u|^2 + \cdots) \tag{2.4}$$

Here, for small values of $|u|^2$, one has $M_z \approx M$; while for large angle precessions where $|u|^2$ is big, it is not the case. For large angle precessions M_z decreases with an increase in $|u|^2$.

An equation to describe the precessional motion of the magnetization was first introduced by Landau and Lifshitz in 1935, Eq. (2.5), which is also known as the torque equation

$$\frac{d\mathbf{M}}{dt} = -|\gamma|\mathbf{M} \times \mathbf{H} \tag{2.5}$$

where $|\gamma|$ is the absolute gyromagnetic ratio.

A direct consequence of this is the ferromagnetic resonance (FMR). If one assumes that the dynamic component of the magnetization takes the form $\mathbf{m}(\mathrm{t}) = m_0 \cos(\omega t)\,\hat{x} + m_0 \sin(\omega t)\,\hat{y}$ and the magnetic field *H* is constant, the torque equation can be solved to obtain,

$$\omega = |\gamma|H \tag{2.6}$$

where ω is the magnetization precession frequency about the field. It should be noted that this is true only for an unbounded magnetic medium with no static or dynamic magnetic effects. In the real-world materials with finite dimensions, the situation is more complicated. In that case the magnetic field (***H*)** needs to be replaced with an effective field H_{eff}, which is a combination of the external magnetic field, the demagnetization field, the anisotropy field, and other magnetic fields present.

When the sample geometry is a thin film, which is of the most interest to the work presented in this thesis, one can have two main configurations: (1) the sample is magnetized in a perpendicular direction to the film plane and (2) the magnetization lies in the plane of the sample. Every other configuration is a linear combination of these two. For this situation the solution was found by Kittel[18] and is given by

[18] C. Kittel, Phys. Rev. **73**, 155 (1948).

$$\omega^2 = [\omega_H + (N_x - N_z)\omega_M]\left[\omega_H + (N_y - N_z)\omega_M\right] \quad (2.7)$$

where N_x, N_y, and N_z are the demagnetization factors, ω_H is equal to $|\gamma|H$, and ω_M is equal to $|\gamma|4\pi M_s$. This equation is commonly referred as the Kittel equation.

2.1 Introduction to Spin Waves

Up to this point only the uniform precession of magnetization is considered. A collection of many magnetic moments also enables the possibility for a collective precession, where the magnetic moments precess at the same frequency but with a slightly different phase from one another. This gives rise to a situation as depicted in Fig. 2.2. The figure depicts such a sequence of magnetic moments lying in a straight line that precess with different phase angles but with the

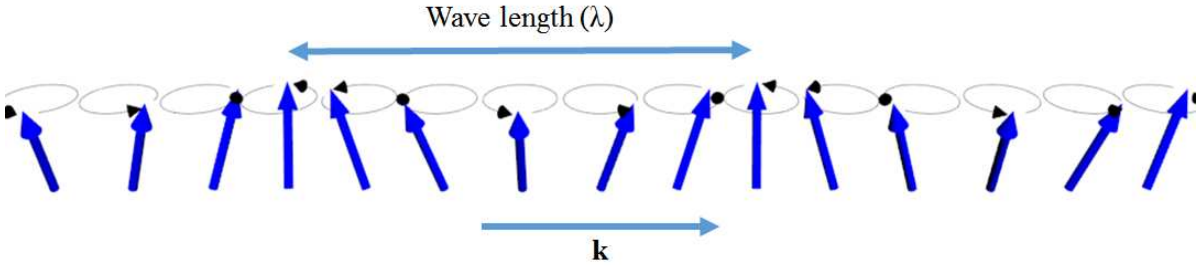

Figure 2.2 A sequence of precessing magnetic moments that form a spin wave, where **k** is the spin wave wavevector and λ is the spin wave wavelength.

same frequency. A collection of such precessions can propagate as a wave in a magnetic material, and is usually termed a spin wave. From the equivalent quasi particle point of view the spin waves are also termed magnons.

Obtaining the dispersion relations of spin waves is a key to the mathematical treatment of spin wave experiments. To obtain the dispersion relations, the Maxwell's boundary value problem

needs to be solved. In such a treatment, two kinds of waves are encountered: the fast electromagnetic waves that are weakly coupled to the magnetic system and the slow waves that are strongly coupled to the magnetic system. This problem can be simplified under the so-called magneto-static approximation, where only the slow waves (strongly coupled to the magnetic system) are considered. Under this approximation, the waves that are treated have a very different wavelength in the medium than that of the electromagnetic waves with the same frequency. This is also the case in all the experimental work presented in this thesis. If one uses this approximation and also treats the dynamic component of the magnetic field **h** (due to the spin wave excitation) as a magneto-static vector potential (Ψ), the so-called Walker's equation, can be obtained, which is written as

$$(1+\chi)\left[\frac{\partial^2\psi}{\partial x^2}+\frac{\partial^2\psi}{\partial y^2}\right]+\frac{\partial^2\psi}{\partial z^2}=0 \qquad (2.8)$$

where χ is the diagonal elements of the susceptibility tensor. This can be considered as the basic equation for magneto-static modes in homogeneous media. Solving the electromagnetic boundary value problem with this equation can yield the relevant dispersion relations for different sample geometries. A descriptive analysis of this is found in the book of "Spin Waves: Theory and applications".[15]

2.1.1 Spin Wave Dispersion

The previous section introduced the idea of spin waves excited in a magnetic material, like YIG. When a YIG thin film strip is magnetized to saturation and magnetic excitations are induced in a localized area, those excitations can propagate along the YIG strip as spin waves. The properties of these spin waves, such as the dispersion, the group velocity, and the phase

velocity, can vary in a wide range, and the properties mainly depend on the magnetization direction of the YIG strip and the magnetic field strength being applied. For the convenience of analysis, the spin waves in magnetic thin films are categorized into three different groups: (1) forward volume spin waves, (2) backward volume spin waves, and (3) surface spin waves. Here, the different categories are decided from the film-field configuration of the YIG strip. The three main configurations in which a YIG film strip can be magnetized are as follows.

(1) YIG strip magnetized perpendicular to the film plane - forward volume spin waves.

(2) YIG strip magnetized in the film plane parallel to the strip length - backward volume spin waves.

(3) YIG strip magnetized in the film plane perpendicular to the strip length - surface spin waves.

Figure 2.3 below shows the film-field configuration, magnetization precession, and dispersion diagrams for the three cases. The axes are defined such that the direction of the magnetic field **H** is along the z direction, and the spin wave wavevector **k** is along the length of the YIG strip and points to the right. The dispersion curves are shown as the dependence of the spin wave frequency ω on the wavenumber k. Therefore, in these plots, the slope along the curves at any given point corresponds to the group velocity v_g at the corresponding k and ω values.

$$v_g = \frac{\partial \omega(k)}{\partial k} \tag{2.9}$$

In Fig. 2.3, the dispersion curves are obtained for a magnetic thin film with saturation induction $4\pi M_s = 1750$ G, magnetic field H=1500 Oe, $|\gamma|$ = 2.8 MHz/Oe, and thickness d = 5 μm. The dashed lines correspond to the characteristic frequencies, $\omega_H = |\gamma| H$, $\omega_B = |\gamma|\sqrt{[H(H + 4\pi M_s)]}$, and $\omega_S = |\gamma| \left(H + {}^{4\pi M_S}/_{2}\right)$.[16]

First, let us consider the case of forward volume waves shown in Fig. 2.3(a) in more detail. The dispersion curve shows a positive slope indicating a positive group velocity. The phase velocity $v_p = {}^{\omega}/_{k}$ is also positive. The term "forward" denotes this fact, that is v_p and v_g are in the same direction. The "volume" denotes that the excitation extends throughout the entire

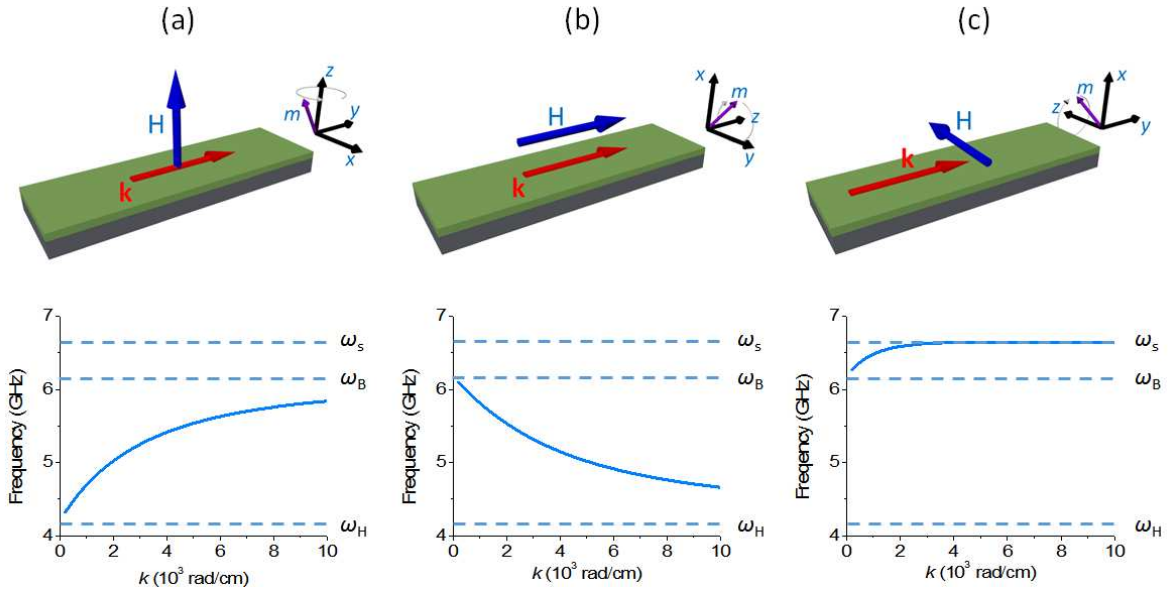

Figure 2.3 Film-field configurations, magnetization precession, and dispersion diagrams for all three classes of spin waves in a long and narrow magnetic thin film strip. In each diagram, the curve gives the relationship between the spin wave frequency and the wavenumber.

film thickness. An approximate dispersion relation for the forward volume spin waves was derived by B. A. Kalinikos[19] and is given by

$$\omega(k) = \sqrt{\omega_H \left[\omega_H + \omega_M \left(1 - \frac{1 - e^{-kd}}{kd}\right)\right]} \tag{2.10}$$

where $\omega_H = |\gamma|(H_0 - 4\pi M_s)$ in the absence of any anisotropy. The dispersion curve in Fig. 2.3(a) was obtained using this equation. The curve indicates that the FMR frequency (k=0) is

[19] B. A. Kalinikos, IEE Proc. **127**, 4 (1980).

equal to ω_H; and with increasing the wavenumber *k*, the frequency increases to ω_B. For all the spin waves the dispersion coefficient *D* is defined as

$$D = \frac{\partial^2 \omega(k)}{\partial^2 k} \tag{2.11}$$

For forward volume spin waves, *D* is negative.

Second, consider the case of backward volume spin waves shown in Fig. 2.3(b). In this case, the dispersion curve indicates that the group velocity (v_g) is negative while the phase velocity (v_p) is positive, hence "backward". Just like in forward volume waves, in backward volume waves "volume" also indicates that the excitation extends throughout the entire film thickness. The approximate dispersion relation for backward volume spin waves is given by the Eq. (2.12).[19] This is the equation that is used to obtain the dispersion curve in Fig. 2.3(b). The FMR frequency (*k*=0) is equal to ω_B. Unlike in the case of forward volume spin waves, for backward volume waves the frequency decreases with an increase in the wavenumber *k*, and the dispersion coefficient *D* is positive.

$$\omega(k) = \sqrt{\omega_H \left[\omega_H + \omega_M \left(\frac{1 - e^{-kd}}{kd} \right) \right]} \tag{2.12}$$

Finally, consider the case of surface spin waves shown in Fig. 2.3(c). In this case, the dispersion curve indicates that the group velocity (v_g) and the phase velocity (v_p) are both positive. But unlike in the previous two cases (forward volume spin waves and backward volume spin waves), the magnetic excitations for surface spin waves do not extend through the entire film thickness. The wave amplitude is not distributed uniformly through the film thickness but decays exponentially from the surfaces of the film.[15]

The surface spin waves are non-reciprocal in the propagation direction. When the field-film configuration is as shown in Fig. 2.3(c), the surface spin waves that travel in the +y direction have the largest dynamic magnetic field close to the top surface of the film while the spin waves that travel in the –y direction have the largest dynamic magnetic field close to the bottom surface.[15] This non-reciprocal effect and the surface nature is pronounced for high wavenumbers ($k > 1/d$). The FMR frequency (k=0) is equal to ω_B, and the frequency increases with an increase in the wavenumber (k). The coefficient D for surface spin waves is negative. The approximate dispersion relation for surface spin waves is given by[19]

$$\omega(k) = \sqrt{\omega_H(\omega_H + \omega_M) + \frac{\omega_M^2}{4}(1 - e^{-2kd})} \tag{2.13}$$

The dispersion curves of the surface spin waves and the backward volume spin waves both start at the same frequency ω_B. The entire frequency pass band of the surface spin waves lie above ω_B while the frequency pass band of the backward volume spin waves lie below ω_B. It should be noted that, in the case of backward volume spin waves, this condition is strictly accurate only when the wavelength is in the range of $k_0 \ll k \ll \pi/a$, where a is the spacing between the two neighboring spins (essentially the lattice constant). In this range, the coupling between the spins is dominated by the dipolar fields. For this reason, these waves are also called dipolar spin waves. For backward volume spin waves, when the wavelength is much shorter, v_g gradually turns from negative to positive and the frequency starts to increase with the increasing wavenumber (k). Therefore, for a given magnetic field (when the field is strong enough to saturate the YIG strip), for backward volume waves there exists a minimum frequency (f_{min}) at which one has $v_g = 0$. Spin waves with higher wavenumbers beyond this point are called

exchange interaction-dominated spin waves. In the experimental work presented in this thesis, this short wave length range was not accessible to the microstrip transducers.

2.1.2 Spin Wave Nonlinearity

In this section details about two types of nonlinearities will be presented. While both the nonlinearities have to do with the spin wave amplitude, the resulting effects are rather different. In the first case, the spin wave dispersion is changed with its amplitude, while in the second it is the transmission loss of the YIG strip that is changed.

a. Amplitude-associated frequency shift

In the following, we consider a YIG thin film strip magnetized perpendicular to the film plane, as in Fig. 2.3(a), which supports forward volume spin waves, where the external magnetic field is along the z axis. Considering the magnetization, it is shown by Eq. (2.4) that, when the precession angle is increased, the longitudinal component (z component) of magnetization is reduced. This results in a shift in the dispersion curve along the frequency axis.

To account for this shift, the M_s in the dispersion equation needs to be replaced with M_z, where $M_z = M_s(1 - |u^2|)$. Now if one defines the nonlinearity coefficient N of a spin wave as[20]

$$N = \frac{\partial \omega}{\partial |u|^2} \tag{2.14}$$

when ω is close to ω_H, N can be estimated as

$$N = \frac{\partial [|\gamma|(H_0 - 4\pi M_z)]}{\partial |u|^2} = \omega_M \tag{2.15}$$

[20] M. Chen, M. A. Tsankov, J. M. Nash, and C. E. Patton, Phys. Rev. B **49**, 12773 (1994).

This indicates two important features: (1) the frequency increases with the amplitude; and (2) the increase is proportional to the film saturation induction but is independent of the external magnetic field. Using the same approach N can also be calculated for backward volume spin waves and surface spin waves as well. It turns out that for both of these two configurations, one has N negative. More Details on this is found in Ref. [16].

This nonlinearity can lead to a phenomena called foldover. For FMR, the foldover effect was first observed by Suhl.[21] In chapter 4, the first observation of the foldover effect for travelling spin waves in a feedback ring configuration will be discussed.

b. Nonlinear three-wave interactions

The nonlinear three-wave interactions can be: (1) three-wave splitting and (2) three-wave confluence. The work presented in this thesis is mainly concerned with the three-wave splitting process.

The interaction can be between high-wavenumber and low-wavenumber backward volume spin waves or between a surface spin wave and two backward volume spin waves.[16] Figure 2.4 illustrates such interactions. Figure 2.4(a) shows the splitting where two backward volume spin waves are produced through the annihilation of a single backward volume spin wave. Figure 2.4(b) shows a splitting where two backward volume spin waves are produced through the annihilation of a single surface spin wave. The important point that should be noted here is that, for the three-wave splitting to take place, two conditions need to be satisfied. First, both the energy (ω) and the momentum (k) should be conserved before and after the splitting process.

[21] H. Suhl, J. Appl. Phys. **31**, 935 (1960).

That is

$$\omega_0 = \omega_1 + \omega_2, \tag{2.16}$$

$$k_0 = k_1 + k_2. \tag{2.17}$$

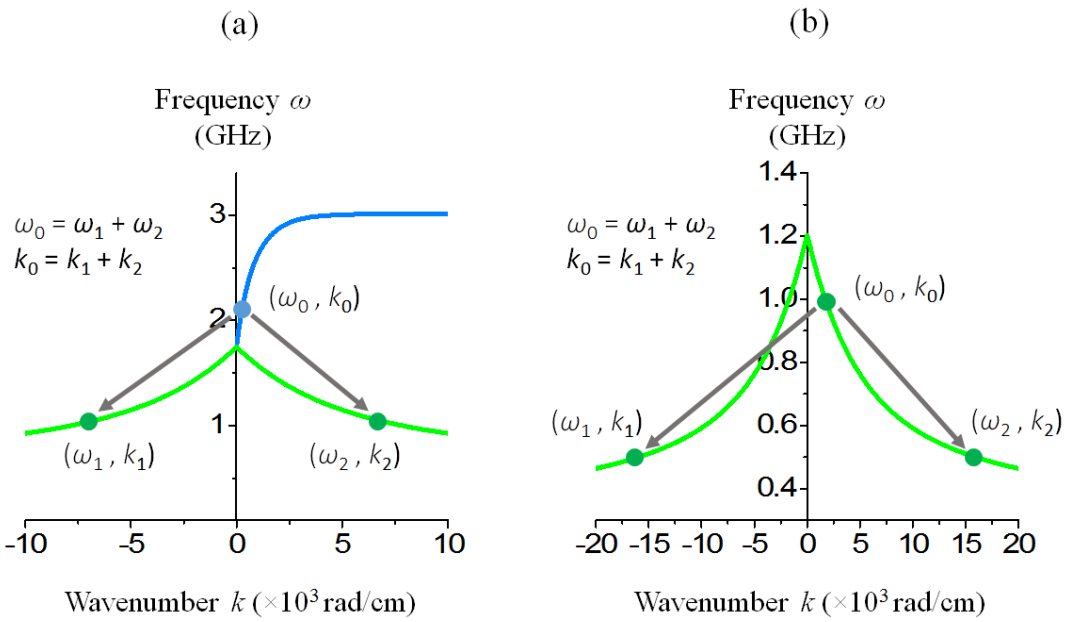

Figure 2.4 (a) Three-wave interactions of backward volume spin waves. (b) Three-wave interactions between surface and backward volume spin waves.

Second, the three-wave splitting occurs only when the spin wave amplitude reaches a certain threshold level. If one tries to excite spin waves in a magnetic thin film like a YIG film, first the amplitude of the spin waves increases linearly with the excitation power that is being used to excite the spin waves. Once the spin wave amplitude reaches a certain threshold level, which enables the three-wave splitting, this linear dependence abruptly stops and the spin wave amplitude starts to show a saturation response. Therefore, this is a nonlinearity that changes the spin wave transmission loss based on its amplitude. When the three-wave splitting occurs in a spin wave experiment, it can be viewed as a an energy transfer from a spin wave with a certain frequency into two different spin waves with lower frequency or frequencies.

The nonlinear three-wave interaction is a well pronounced nonlinearity in YIG films and has already been utilized for microwave applications such as generation of ultrashort pulses,[18] frequency selective power limiting,[19] and signal to noise enhancement [20] in the past. Some detailed studies had already been carried out to better understand this effect.[21, 22]

When a microstrip transducer is used to excite spin waves in a magnetic thin film, the three-wave interaction happens in the film area close to the transducer. Up to now the Brillion light scattering technique is the only technique that enabled the observation of the effect very close to the transducer. In chapter 6 the spin pumping and the ISHE are used to gain new information about this process.

2.2 Spin Wave Experimental Setup

This section provides an overview of the spin wave experimental setups that were utilized for the studies in this thesis. Specifically, the methods for the excitation and detection of spin waves in YIG thin films are introduced. As having already been introduced, the spin waves that are excited at a localized area can propagate along the length of the YIG film strip. For this reason, the YIG film strips are also called YIG waveguides in the literature. In this thesis, these two terms will be used interchangeably.

Figure 2.5 below depicts a typical spin wave excitation and detection arrangement. For many spin wave experiments this arrangement can also be considered as a basic unit. For example, in chapter 4 this arrangement is used as a part of a feedback ring. This excitation/detection experimental arrangement consists of two parts: (1) excitation and detection transducers and, (2) a YIG thin film strip. The YIG strip is typically cut from a low-loss, single-crystal YIG thin film wafer grown on a gadolinium gallium garnet (GGG) substrate. Typically, the GGG substrate is 0.5 mm thick, while the YIG film is 5–15 μm thick. The YIG film is grown

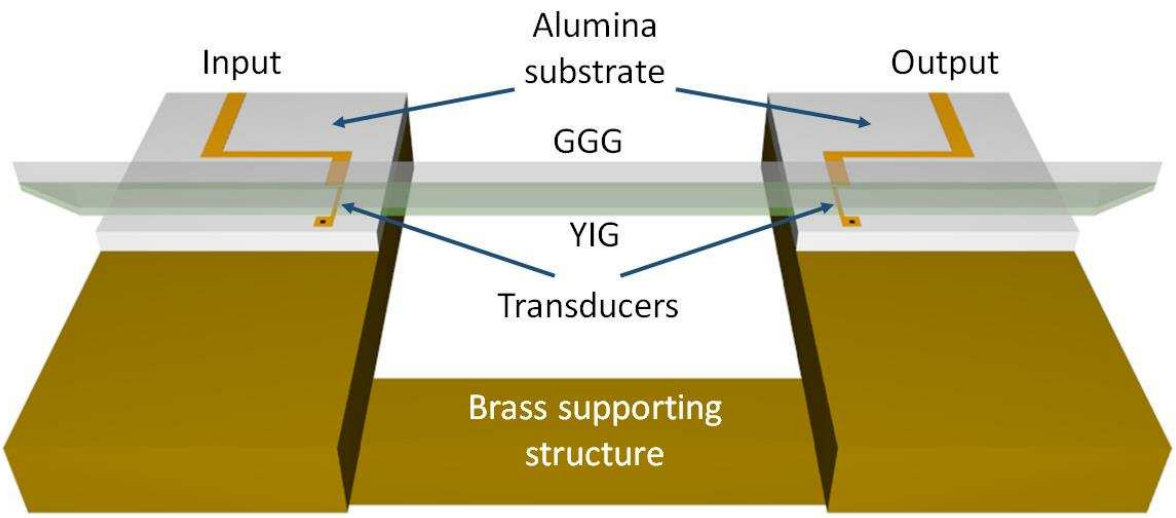

Figure 2.5 YIG strip, excitation transducer, and detection transducer arrangement. The YIG strip is placed on the transducers, with the YIG film facing down and touching the transducers and the GGG substrate facing up.

using the method of liquid phase epitaxy (LPE)[22]. The relevant parameters of the corresponding YIG strips that were used for the experiments are given in detail in chapters 4, 5, and 6.

Consider now the excitation and detection transducers. Microstrip transducers are the most commonly used method for the excitation and detection of spin waves. A microstrip transducer

[22] J. D. Adam, M. R. Daniel, P. R. Emtage, and S. H. Talisa, in *Thin Films for Advanced Electronic Devices*, edited by M. H. Francombe and J. L. Vassen (Academic, Boston, 1991).

is basically a microwave antenna deposited on an alumina substrate. The alumina substrate is typically 0.5 mm thick and has a relative dielectric constant of $\varepsilon_r \approx 10$. One side of it is covered with a metallic layer which acts as the ground plane. On the other side a special conducting line that provides the specific microwave properties is deposited. This line normally consists of three parts: (1) a wide conducting line close to the edge that facilitates the soldering of an SMA connector, (2) a 50-μm-wide, 2-mm-long section that acts as the microwave antenna, and (3) a conducting through hole that electrically connects this line to the ground plane. Figure 2.5 depicts how the YIG strip is placed on the 50-μm-wide, 2-mm-long section, which acts as the microwave antenna. These antennas can serve both the purposes of the excitation and the detection.

The housing that holds everything in place is made of a nonmagnetic material such as aluminum or brass. To apply a magnetic field to the YIG strip, this entire arrangement is placed in the gap of an electromagnet. This excitation and detection arrangement was used for the experimental work presented in chapters 4 and 5.

While the above experimental arrangement suffices for many experiments, this kind of setup provides only frequency and time resolution and cannot provide spatial resolution. To incorporate spatial resolution capability into an experiment, one can use an inductive magneto-dynamic probe.

An inductive probe consists of a 50-μm-diameter wire loop connected to the end of a rigid coaxial line. Figure 2.6 schematically shows such an experimental setup. In Fig. 2.5, the microstrip transducers are used for both the excitation and detection of the spin waves. In the arrangement in Fig. 2.6, the detection microstrip transducer in Fig. 2.5 is replaced with an inductive

magneto-dynamic probe. The spin waves are excited by the microstrip transducer at the left end and the detection is done by the inductive probe. The probe is movable and can be moved above the YIG film surface in both the x and y directions. The small electric loop at the end of the probe picks up the dynamic magnetic components of the spin wave excitations in its vicinity. For

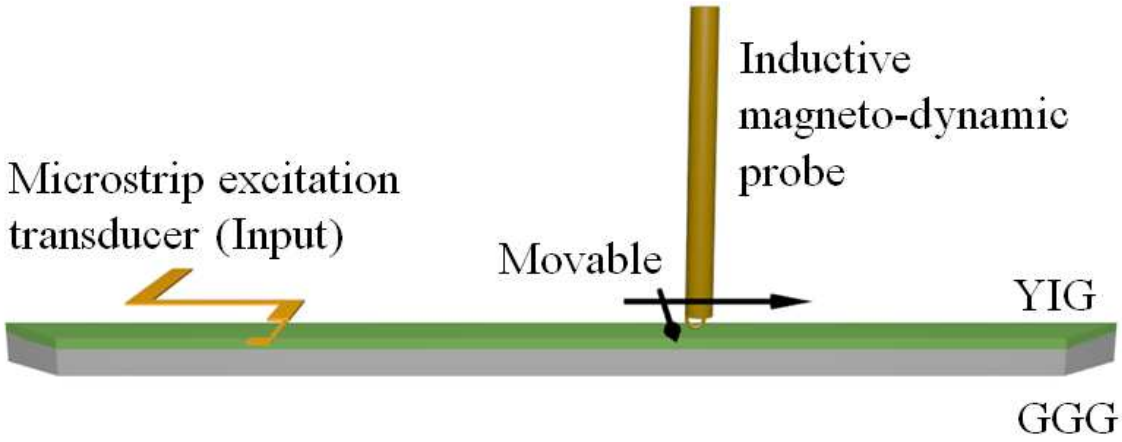

Figure 2.6 A schematic of inductive magneto-dynamic probe experimental setup.

the inductive probe data presented in this thesis, the probe scanning is enabled by Thorlab NRT100 translational stages, which have 5 µm spatial accuracy and 1 µm bidirectional repeatability andare controlled by a Labview program.

CHAPTER 3

Inverse Spin Hall Effect, Spin Pumping, and Spin Seebeck Effect

In this chapter the key ideas behind microwave-induced spin pumping, the inverse spin Hall effect (ISHE), and the spin Seebeck effect (SSE) are introduced. These concepts are essential for a better understanding of the work presented in chapters 6 and 7. In section 3.1, both the spin Hall effect and the ISHE are described in detail. In the work presented in this thesis the ISHE is observed due to two spin pumping mechanisms: (1) microwave-induced spin pumping, and (2) thermal gradient-induced spin pumping, also known as the SSE. Details about these two mechanisms, key experimental techniques, and details on the experimental setups are the subjects of sections 3.2 and 3.3.

3.1 Inverse Spin Hall Effect

The spin Hall effect was first predicted by Dyakonov and Perel in 1971,[23] while the term "spin Hall effect" was first coined by Hirsh in 1999.[24] The first experimental work in this area done by Fleisher's group at Ioffe institute in Saint Petersburg,[25] provided the first observation of

[23] M.I. Dyakonov and V.I. Perel, Sov. Phys. JETP Lett. **13**, 467 (1971).
[24] J. E. Hirsch, Phys. Rev. Lett. **83**, 1834 (1999).
[25] M. I. Dyakonov, arxiv.org/pdf/1210.3200, (2012).

what is now known as the ISHE. In the normal Hall effect, when an electrical conductor is placed in a magnetic field and an electric charge current is run through it, an accumulation of electrons is observed in the orthogonal direction to both the magnetic field and the direction of the current. Unlike in the normal Hall effect, in the spin Hall effect when an electric charge current is made to flow in a heavy metal like Pt, due to the spin dependent scattering of the electrons an accumulation of electrons on lateral boundaries of the conductor is observed.[25] Furthermore, these electrons have a spin polarization that winds around the direction of the charge current. The spin polarization of the electrons in opposite sides point in opposite directions and the direction of winding will reverse if the charge current direction is reversed. What direction the polarization would wind for a given charge current direction depends on the heavy metal being used.

The origin of this effect is widely believed to be the spin dependent scattering, due to strong spin-orbit coupling. Other ideas have also been proposed.[26] Spin-orbit coupling can be understood as follows. Consider an electron passing by the vicinity of a non-magnetic ion. According to the Lorentz transformation, it will experience an effective magnetic field **B** given by

$$\mathbf{B} = -\frac{1}{c^2}\mathbf{v}\times\mathbf{E} = -\frac{1}{c^2}\mathbf{v}\times\left(\frac{kq}{r^3}\mathbf{r}\right) \tag{3.1}$$

where **E** is the electric field due to the ion, **v** is the velocity of the electron, and **r** is the position vector of the electron relative to the ion, *q* is the charge of the ion, and *k* is the Coulomb's constant. If the magnetic moment of the electron is **μ**, the Zeeman energy of the electron in the moving frame can now be written as

$$E_{\mathrm{Z}} = -\boldsymbol{\mu}\cdot\mathbf{B} = \frac{\mu_B kq}{c^2 r^3}(\mathbf{v}\times\mathbf{r})\cdot\hat{\boldsymbol{\sigma}} \tag{3.2}$$

[26] A. Hoffmann, IEEE Trans. Magn. **49**, 5172 (2013).

where E_Z is the Zeeman energy of the electron and $\hat{\boldsymbol{\sigma}}$ denotes a unit vector in the direction of the electron's magnetic moment. Figure 3.1 schematically shows such a scattering. When an

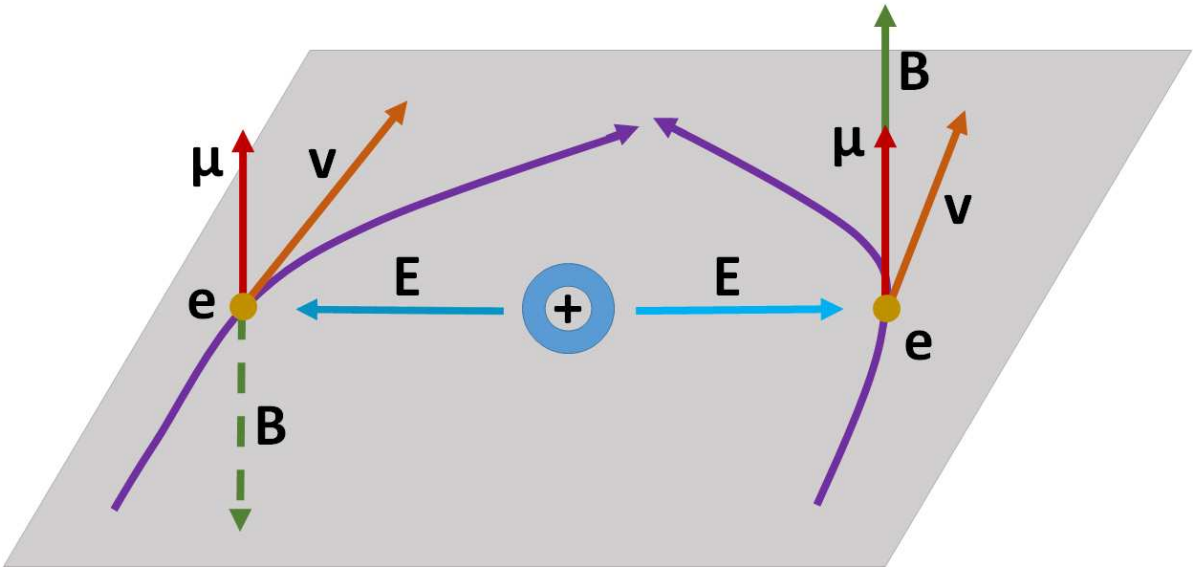

Figure 3.1 Schematic of two electrons scattering by a positively charged non-magnetc ion. The electrons sees a magnetic field (**B ~ -v×E)** perpendicular to the plane of the electron trajectory.[25] The magnetic field is pointed in opposite directions for electrons scattering from the left and the right.

electron scatters from an ion it will deviate into a direction depending on the sign of the polarization. The **B** field exists in the electron's moving frame and is seen by the spin polarization of the electron.

The filed **B** is perpendicular to both the position vector of the electron with respect to the ion and the velocity direction of the electron. Depending on from which side the electron scatters (left or right), **B** has opposite directions. The Zeeman energy of the electron, due to **B** and its spin, is the so-called spin-orbit interaction.[25] Since the electric field due to the ion decreases with **r** as $1/r^2$, |**B**| experienced by an electron decreases as well with **r** in the same way. This inhomogeneity in **B** results in a Zeeman energy gradient. This gradient is what applies a spin dependent force on the scattering electron. As a consequence, if the electrons that scatter are not

polarized, this effect tends to scatter and separate electrons depending on their spin polarization directions. This is the so-called spin Hall effect.

Now consider the situation that is schematically depicted in Fig. 3.2. Figure 3.2(a) depicts a flow of electrons in the x direction (an electric current in the -x direction) in a Pt block with electrons not having any particular spin polarizations. Figure 3.2(b), on the other hand, shows the same situation but with electrons polarized in one direction. In Fig. 3.2(a), in accordance with the spin Hall effect, the electrons with opposite polarizations scatter into opposite sides of the Pt block. The spin-up electrons scatter into the page direction and the spin-down electrons

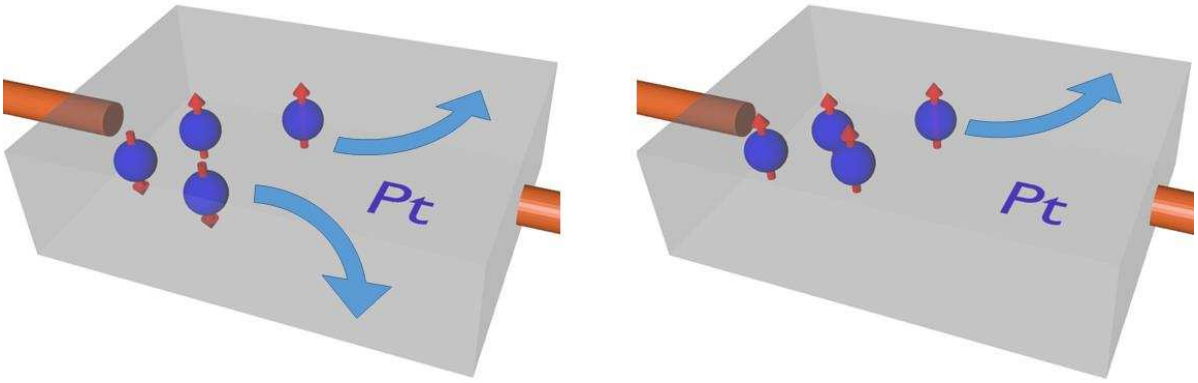

Figure 3.2 (a) Flow of electrons in a Pt block, with spin polarization pointing up and down, scattering to different directions, (b) Flow of electrons in a Pt block, with spin polarization pointing up scattering to only one direction.

scatter out of the page direction. Since no preference in the spin polarization direction for the electrons is assumed, this does not create any measurable potential differences along any direction. If we now consider Fig. 3.2(b), since all the electrons are polarized in the same direction (assumed up) they all tend to scatter in the same direction (into the page) and result in a measurable voltage across the width of the Pt block.

This generation of an electric potential difference due to a spin polarized current is known as the ISHE produced voltage. With this the question arises: How to generate a spin polarized

current? Spin pumping is one of the answers to this question. It has been shown that when a heavy metal with strong spin-orbit coupling like Pt is in contact with a ferromagnetic material like YIG, the magnetic excitations in the ferromagnetic material can generate an angular momentum flow from ferromagnetic material into the heavy metal, through the interface. This effect is widely known as the spin pumping effect. This effect polarizes the conduction electrons in the heavy metal at the interface and thereby gives rise to a spin current inside the heavy metal.[27]

This spin current in turn, produces a measurable voltage in a perpendicular direction to the interface in the heavy metal. In this arrangement there are three important directions: (1) the direction of angular momentum flow, (2) direction of the angular momentum, and (3) the length along which the voltage is measured in the heavy metal. Since the flow of angular momentum is from the ferromagnetic material into the heavy metal, direction (1) is the perpendicular direction to the interface. Direction (2) is parallel to the magnetization direction of the ferromagnetic material. Direction (3) is orthogonal to directions (1) and (2). The specific direction depends on the spin Hall angle of the metal. When the metal has a positive spin Hall angle, directions 1, 2, and 3 form a right handed set of axes, while it is left-handed when the spin Hall angle is negative. The voltage produced due to the ISHE is proportional to[28]

$$\mathbf{j_c} \propto \Theta_{SH} \mathbf{j_s} \times \hat{\boldsymbol{\sigma}} \tag{3.3}$$

where $\mathbf{j_c}$ is the charge current density in the heavy metal and $\mathbf{j_s}$ is the density of the spin current flowing into the heavy metal. Two promising methods to efficiently induce such spin pumping

[27] J. Xiao, G. E. W. Bauer, K. Uchida, E. Saitoh, and S. Maekawa, Phys. Rev. B **81**, 214418 (2010).
[28] H. L. Wang, C. H. Du, Y. Pu, R. Adur, P. C. Hammel, and F. Y. Yang, Phys. Rev. Lett. **112**, 197201 (2014).

and thereby an ISHE voltage have been identified: (1) microwave-induced spin pumping[28] and (2) the spin Seebeck effect-induced spin pumping,[29] which are introduced in detail below.

3.2 Microwave-Induced Spin Pumping

When a bi-layer structure is made by depositing a thin Pt layer on a YIG thin film, the microwave-driven magnetic excitations in the YIG can pump a spin current into the Pt. The excitations can be either FMR excitations, standing spin waves, or traveling spin waves. This technique is one of the most efficient ways to induce a strong spin pumping from the YIG into the Pt.

3.2.1 Experimental Setup

A special experimental setup was developed to measure the microwave induced spin pumping-produced ISHE voltage in YIG/Pt bi-layer structures. In this section, the experimental setup is explained in detail. Similar experimental setups have been used to measure the ISHE voltage of different metal/YIG bi-layer structures, both at low temperature and room temperature, as well as the ISHE voltage of materials in topological phases.

First, a special microstrip transducer structure was built. Figure 3.3 shows a photo of this microstrip transducer structure, with a YIG/Pt sample. The entire structure was made of aluminum and brass. The YIG/Pt sample is placed on the aluminum base with the Pt facing up

[29] T. Kikkawa, K. Uchida, Y. Shiomi, Z. Qiu, D. Hou, D. Tian, H. Nakayama, X.-F. Jin, and E. Saitoh, Phys. Rev. Lett. **110**, 067207 (2013).

and the GGG substrate facing down, and the microstrip antenna facing down is lowered onto the sample. A special microstrip antenna of a small dimension is used. The width of the entire antenna structure was only 2 mm. Since both the microwave excitation and the voltage

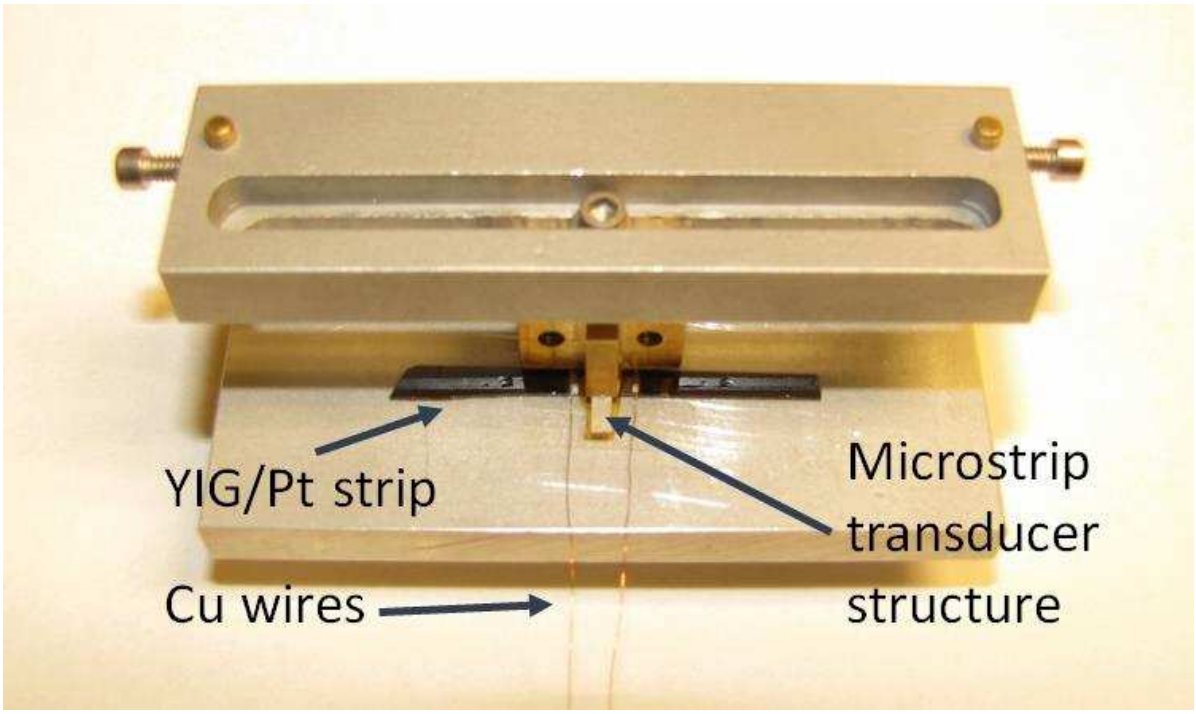

Figure 3.3 Picture of the microstrip transducer structure with a YIG/Pt sample placed underneath the transducer.

measurement need to be done from the same surface, this small profile of the antenna structure allows for the use of small samples.

The microstrip transducer was 50 μm wide and 2 mm long and had a 50 Ω impedance. When the microstrip antenna is placed on the Pt covered section of the sample, an insulating layer is used in-between the microstrip antenna and the sample. To measure the small voltage produced along the Pt length, two fine Cu wires were attached to the end sides of the Pt strip using high-purity silver ink or indium dots. Figure 3.4, shows a schematic of the complete experimental setup. During the experiment, an in-plane magnetic field is applied perpendicular to the length of the YIG/Pt strip. This film-field configuration supports the propagation of surface spin waves in

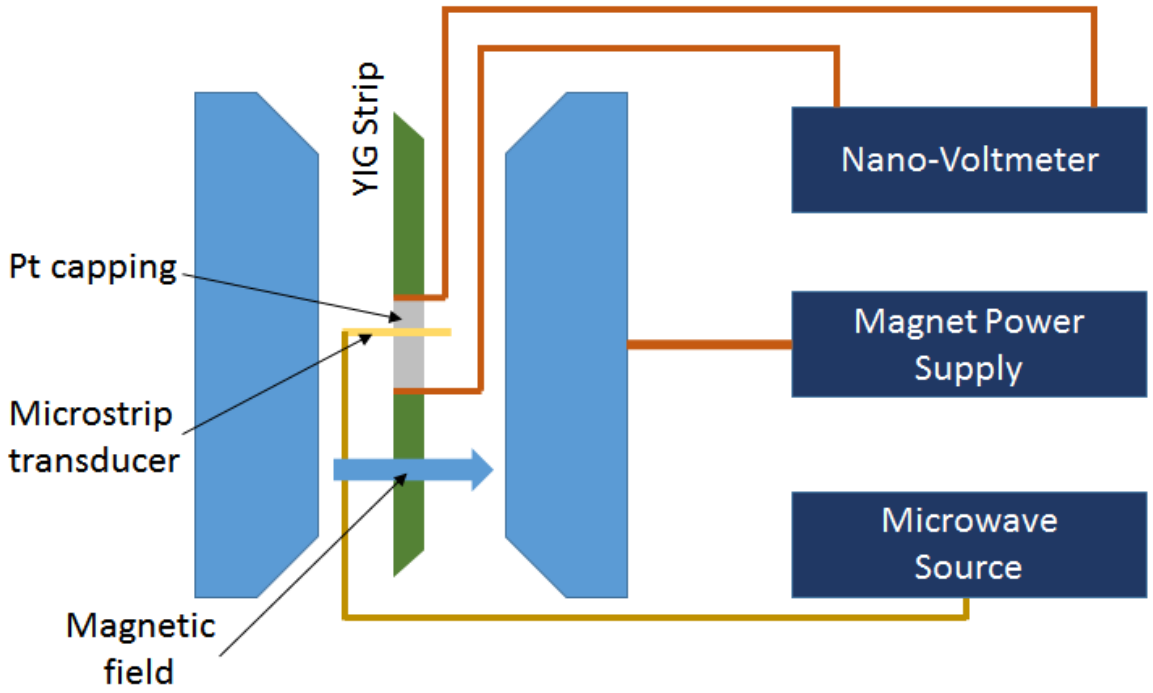

Figure 3.4 Schematic of the experimental setup used to measure the ISHE voltage.

the YIG. To provide the magnetic field an electro magnet is used. An HP 83623B signal generator is used as the microwave source. The typical ISHE voltage that is produced in experiments varies in the range of few tens of nano volts to few hundreds of micro volts. To measure this small voltage, a Keithley 2182A nano voltmeter is utilized. The experimental setup is capable of carrying out ISHE voltage measurements both as a function of the magnetic field and the microwave frequency. To facilitate the measurements in a wide magnetic field range and a wide frequency range, a Labview program was written to fully automate the data collection process which is tested to run reliably and unattended for several days at a time.

Some useful techniques to reduce the noise in this experimental setup are worth a note. The vibration of the Cu wires, which connect the Pt layer to the nano voltmeter was identified as the primary source of the noise. [Here the thin Pt layer, the two Cu wires, and the nano voltmeter form a closed electric loop, with part of it being in the magnetic field.] Any changes in the total

flux enclosed by this loop give rise to voltage noise in the measurements. Therefore, extra efforts were taken to tightly secure the wires to avoid any vibrations. This improved the noise figure by roughly two orders of magnitude, from about ±500 nV to about ±5 nV.

3.3 Spin Seebeck Effect

Consider the same YIG/Pt bi-layer structure discussed in the previous section. It turns out that when a temperature gradient is established across the thickness of this structure, a spin pumping between the YIG and the Pt is generated. This phenomenon can be understood as follows.[30] The phonons in the YIG, the magnons in the YIG, the conduction electrons in the Pt, and the phonons in the Pt can be considered as separate subsystems. The conduction electron subsystem in the Pt, the phonon subsystem in the Pt, and the phonon subsystem in the YIG are coupled to each other strongly. When a temperature gradient is induced, it is these three subsystems that have the gradual change in the temperature along the thickness direction. Assume the case where the temperature gradient across the thickness of the YIG/Pt sample is created, such that the top Pt layer is at a lower temperature and the bottom YIG film is at a higher temperature. When this is the case, the phonons and electrons at the top surface of the Pt layer has the lowest temperature while the phonons at the YIG bottom surface has the highest temperature. Because of the strong coupling, at the YIG/Pt interface the electrons in the Pt and the phonons in both the YIG and the Pt have the same temperature. The magnon subsystem is

[30] W. J. Antel, Jr., M. M. Schwickert, Tao Lin, W. L. O'Brien, and G. R. Harp, Phys. Rev. B **60**, 12933 (1999).

different, as it is weakly coupled to the phonons and strongly coupled within itself. For this reason, the entire magnon subsystem has almost the same temperature throughout the sample thickness, which is close to the average temperature of the YIG film. As a result, since the Pt layer is at a lower temperature than the average temperature of the YIG, at the YIG/Pt interface there will be an angular momentum flow from the YIG to the Pt electrons. This in turn generates the spin current inside the Pt layer which gives rise to an ISHE voltage. This is the so-called SSE.

3.3.1 Experimental Setup

The main objective of the experimental setup is to apply a temperature gradient across the thickness of the YIG/Pt sample and measure the resulting voltage along the Pt length. Figure 3.5 schematically shows the SSE experimental setup. A YIG/Pt bi-layer sample is sandwiched

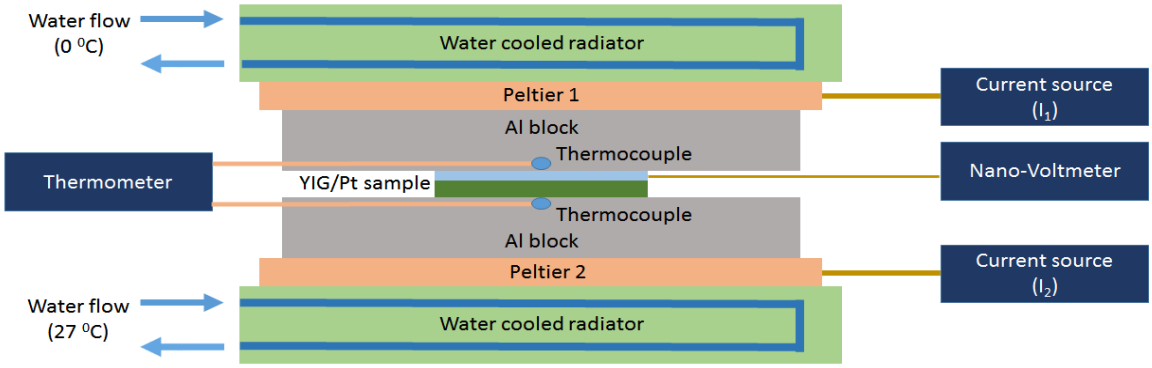

Figure 3.5 Schematic of the experimental setup that is used to measure the SSE-produced ISHE voltage.

between two metal blocks which are held at two different temperatures. The temperature gradient results in a measurable voltage in the Pt due to the SSE.

In order to measure the temperature at the top and bottom surfaces of the sample, two grooves were cut in the metal blocks through which two thermocouples were inserted. These thermocouples were in thermal contact with the top and bottom surfaces of the sample, roughly at

the center. In order to ensure good thermal contact between the metal blocks and the YIG/Pt sample, a thin layer of vacuum grease is used. For electric isolation and prevention of any scratching a thin layer of Kapton tape is used in either side of the sample.

Two Peltier devices (Peltier 1 and Peltier 2) were controlled by two separate current sources I_1 and I_2. The Peltier device is made out of a large number of small semi-conducting N-P junctions and work as an electrically controlled heat pump. When a current is applied to a Peltier device, it pumps heat in one direction, which cools down one side and heats up the other. Therefore it can also be considered as a device that generates a current-dependent temperature difference across itself. The two Peltier devices are used for the fine control of the temperatures of the two metal blocks that sandwich the YIG/Pt sample.

In contact with the Peltier devices are two small water-cooled radiators (radiator 1 and radiator 2). In order to apply a magnetic field to the YIG/Pt sample, the entire setup is placed between two solid state permanent magnets (neodymium). The magnetic field is applied in the plane of the sample perpendicular to the sample length. To measure the voltage produced by the SSE, two thin Cu wires were attached to the two ends of the Pt strip. In this experiment, the tight secure of the Cu wires is also important to reduce the noise, as discussed in the microwave induced spin pumping measurements.

The operation of the experimental setup is as follows. Hot and cold water is run through the water-cooled radiators. A flow of cold water at 0 °C is run through the one in the cold side, while water at room temperature (27 °C) is run through the other. These two radiators determine the temperature of the outer walls of the two Peltier devices (one at roughly 0 °C and the other at 27 °C). Apart from this, the radiators also serve two other purposes: (1) temperature stability and (2) removal of the excess heat generated by the two Peltier devices due to Ohmic heating. With

the application of an appropriate current, the two Peltier devices control the temperature of the metal blocks.

The accurate control of the temperature gradient is achieved with the help from a Labview program. This program served the following purposes: (1) monitor and record the temperatures from the two thermocouples, (2) control the current sources connected to the two Peltier devices to maintain the desired temperature gradient for prolonged time intervals, and (3) record the SSE-produced voltage measured by the nano voltmeter. All the data presented in chapter 7 were obtained with the use of this experimental setup.

CHAPTER 4

Foldover of Nonlinear Eigenmodes in Magnetic Thin Film-Based Feedback Rings

Active feedback ring systems that consist of a closed loop of a dissipative transmission line and an active element to compensate for the dissipation constitute an excellent testbed for exploring nonlinear dynamics in driven damped systems. Example systems include electromagnetic transmission line ring oscillators,[31,32,33,34] optical fiber rings,[35,36,37,38,39] and magnetic thin film-based feedback rings,[40,41,42,43,44] among others. Such systems not only sustain

[31] D. S. Ricketts, X. Li, and D. Ham, IEEE Trans. Microwave Theory Tech. **54**, 373 (2006).
[32] D. Ham, X. Li, and D. S. Ricketts, IEEE Commun. Mag. **44**, 126 (2006).
[33] D. S. Ricketts, X. Li, N. Sun, K. Woo, and D. Ham, IEEE J. Solid-State Circuits. **42**, 1657 (2007).
[34] M. Ponton, A. Suarez, IEEE Trans. Microwave Theory Tech. **64**, 3499 (2014).
[35] L. Luo, T. J. Tee, and P. L. Chu, J. Opt. Soc. Am. B **15**, 972 (1998).
[36] J. M. Soto-Crespo, M. Grapinet, P. Grelu, and N. Akhmediev, Phys. Rev. E **70**, 066612 (2004).
[37] L. M. Zhao, D. Y. Tang, F. Lin, and B. Zhao, Opt. Commun. **252**, 167 (2005).
[38] L. M. Zhao, D. Y. Tang, and A. Q. Liu, Chaos **16**, 013128 (2006).
[39] F. Li, X. Feng, H. Zheng, C. Lu, H.Y. Tam, J. N. Kutz, and P.K.A. Wai, Opt. Commun. **284**, 2336 (2011).
[40] V. E. Demidov and N. G. Kovshikov, Tech. Phys. Lett. **24(4)**, 274 (1998).
[41] S. O. Demokritov, A. A. Serga, V. E. Demidov, B. Hillebrands, M. P. Kostylev, and B. A. Kalinikos, Nature **426**, 159 (2003).
[42] M. Wu, B. A. Kalinikos, L. D. Carr, and C. E. Patton, Phys. Rev. Lett. **96**, 187202 (2006).
[43] A. B. Ustinov, V. E. Demidov, A. V. Kondrashov, B. A. Kalinikos, and S. O. Demokritov, Phys. Rev. Lett. **106**, 017201 (2011).
[44] Z. Wang, A. Hagerstrom, J. Q. Anderson, W. Tong, M. Wu, L. D. Carr, R. Eykholt, and B. A. Kalinikos, Phys. Rev. Lett. **107**, 114102 (2011).

the self-generation of envelope solitons, both bright,[31,36,37,41] and dark,[45] but have also enabled the observation of symmetry-breaking nonlinear modes,[41] chaotic solitons,[32,37,38,43,44] and soliton fractals[42] and have also allowed for the study of the excitation of chaotic dynamics via different nonlinear processes.[32,35,37,39,40,46,47]

This chapter reports that active feedback rings also support another fascinating nonlinear effect - the foldover effect. The nonlinear foldover effect originates from the nonlinearity in which the oscillation frequency varies with the amplitude, and manifests itself as the bending of the resonant peak in an oscillation amplitude vs. frequency plot. It occurs in nonlinear systems as diverse as driven pendula,[48] spring-based mechanical oscillators,[49] electrical RLC resonant circuits,[50] and precessional magnetic moments in both insulating and metallic magnets.[51,52,53] The effect, however, has never been observed in ring systems so far.

The experiments made use of an active feedback ring that consists of a magnetic thin film strip serving as a spin-wave transmission line and a microwave amplifier which amplifies the output signal from the magnetic strip and then feeds it back to the input of the magnetic strip. This ring system has a sequence of resonant eigenmodes for which the phase per round trip satisfies constructive interference conditions.[16] Thanks to these eigenmodes the amplitude vs. frequency

[45] B. A. Kalinikos, M. M. Scott, and C. E. Patton, Phys. Rev. Lett. **84**, 4697 (2000).
[46] A. M. Hagerstrom, W. Tong, M. Wu, B. A. Kalinikos, and R. Eykholt, Phys. Rev. Lett. **102**, 207202 (2009).
[47] M. Wu, A. M. Hagerstrom, R. Eykholt, A. Kondrashov, and B. A. Kalinikos Phys. Rev. Lett. **102**, 237203 (2009).
[48] Y. Xu, T. J. Alexander, H. Sidhu, and P. G. Kevrekidis. Phys. Rev. E **90**, 042921 (2014)
[49] Donoso, Guillermo, and Celso L. Ladera. Eur. J. of Phys **33**, 1486 (2012).
[50] B. Cretin and D. Vernier. E-print: arxiv.org/abs/0801.1301 (2008).
[51] M. T. Weiss. Phys. Rev. Lett. **1**, 239 (1958).
[52] J. Lustikova, Y. Shiomi, Y. Handa, and E. Saitoh. J. Appl. Phys. **117**, 073901 (2015).
[53] Y. S. Gui, A. Wirthmann, N. Mecking, and C.M. Hu Phys. Rev. B **80**, 060402 (2009).

response of the ring shows resonant peaks at certain frequencies, and these peaks fold over to higher frequencies when the peak amplitude is large. This foldover effect is intrinsic and originates from the nonlinearity-caused frequency shift of the traveling spin wave. It is not associated with either high-power heating or four-wave interactions, as evident from the experimental data. To better understand the physical origin of the observed foldover effect, theoretical calculations were carried out that took into account the nonlinearity of the spin waves. The theoretical results not only confirmed the experimental observations, but also showed the rolling over of the top part of the resonant peaks which cannot be measured experimentally.

It is important to highlight that this work further demonstrates the excellent versatility of the feedback rings as a fundamental system for exploring nonlinear dynamics. It should also be emphasized that the foldover effect presented here should be universal and is expected to occur in any feedback ring systems, including electromagnetic transmission line oscillators Ref [31-34] and optical fiber rings Ref [35-39]. Future work that demonstrates the foldover phenomenon in these systems is of great interest.

4.1 Experimental Configuration

The ring setup is shown schematically in Fig. 4.1. It consists of a magnetic $Y_3Fe_5O_{12}$ (YIG) thin film strip and two microstrip transducers placed over the YIG strip for the excitation and detection of spin waves in the YIG strip. The YIG strip is magnetized by a perpendicular magnetic field. This film-field configuration supports the propagation of forward volume spin waves along the YIG strip and, at the same time, also prohibits three-wave nonlinear

interactions.[54,15] The output signal from the detection transducer is fed back to the excitation transducer through an adjustable microwave attenuator and a microwave amplifier. The response in the ring is sampled through two directional couplers and is measured with a vector network analyzer. For the data presented below, the YIG strip was 1.6 mm wide and 55 mm long, the microstrip transducers were 50 μm wide and 2 mm long elements, the transducer separation (l) was held at 10.4 mm, and the magnetic field was fixed at 2990 Oe. Both the microwave amplifier and the attenuator had a linear response over 1-8 GHz.

Figure 4.2 presents the characteristics of the YIG strip and the feedback ring. Figure 4.2(a) shows the transmission coefficient data ($\mathbf{S}_{21}$) measured as a function of frequency (f) for the

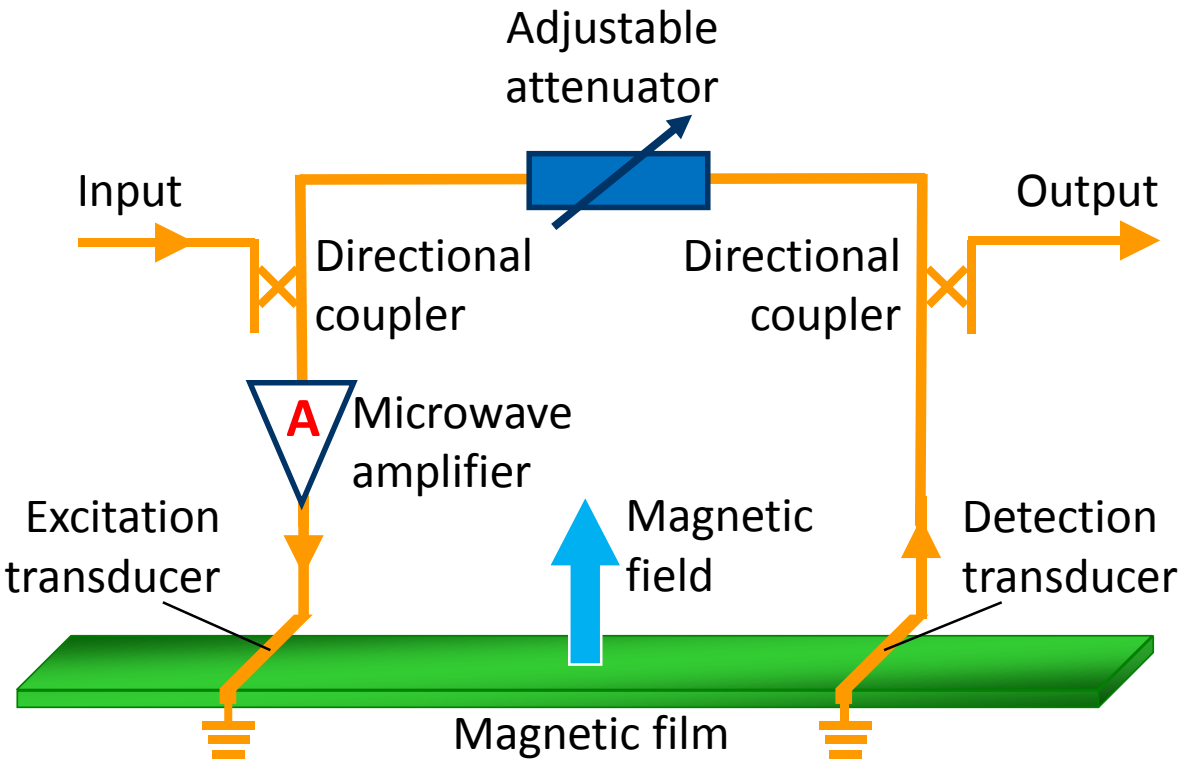

Figure 4.1 Schematic of a magnetic thin film strip-based active feedback ring system.

[54] P. Kabos and V. S. Stalmachov, *Magnetostatic Waves and Their Applications* (Chapman and Hall, London, UK, 1994).

transducer-YIG-transducer structure. The left diagram shows the amplitude vs. frequency response of the structure, namely, the amplitude of $\mathbf{S}_{21}(f)$. In the right diagram, the red curve presents the spin-wave dispersion curve which was determined from the phase of $\mathbf{S}_{21}(f)$, while the green curve shows a theoretical fit to the spin-wave dispersion equation Ref [15, 54]. The data indicate that the spin waves in the YIG film have a passband of about 3.30-3.55 GHz. The fitting used an absolute gyromagnetic ratio $|\gamma|$ of 2.8 MHz/Oe and an effective saturation induction ($4\pi M_s$) of 1750 G. The fitting parameters were the magnetic field (H) and the YIG film thickness (d). For the fit given in Fig. 4.2(a), one has H=2920 Oe and d=10.2 μm. The field value is slightly smaller than the experimental value. Possible reasons for this difference include the errors in measuring the field and determining the low cut-off frequency of the spin wave and the assumption of zero anisotropy field in the YIG film. Note that for all the $\mathbf{S}_{21}$ measurements in this work, the signals from the vector network analyzer had the same power, which was -17 dBm.

Figure 4.2(b) shows the amplitude-frequency response and dispersion curve of the ring in the same format as in Fig. 4.2(a). Figure 4.2(c) presents the same data as in Fig. 4.2(b), but in much smaller frequency scales. One can see that in comparison with the transducer-YIG-transducer case, the amplitude-frequency response in the feedback ring indicates a very similar passband but shows notable resonant peaks, while the dispersion curve shows steps at the frequencies of the resonant peaks. These peaks and steps are indicative of the ring eigenmodes.[16] The vertical dashed lines in Fig. 4.2(c) indicate the wavenumbers (k) of the eigenmodes which were determined by the phase condition $kl+\phi_e=2\pi n$, where kl is the phase change due to the propagation of the spin wave, ϕ_e is the phase shift introduced by the electronic circuits, and n is an integer and denotes the ring eigenmode index. Note that ϕ_e varies with f, and the ϕ_e value used in the k calculations ranged from 2.7 rad to 8.4 rad for n=1-25. It should be mentioned that when the attenuation (α)

of the adjustable attenuator is relatively large and all ring eigenmodes experience an overall net loss (L) for one round trip, there is no spontaneous signal in the ring. However, if α is reduced to a certain level, the ring eigenmode with the lowest decay rate (n=5) can have a zero net loss,

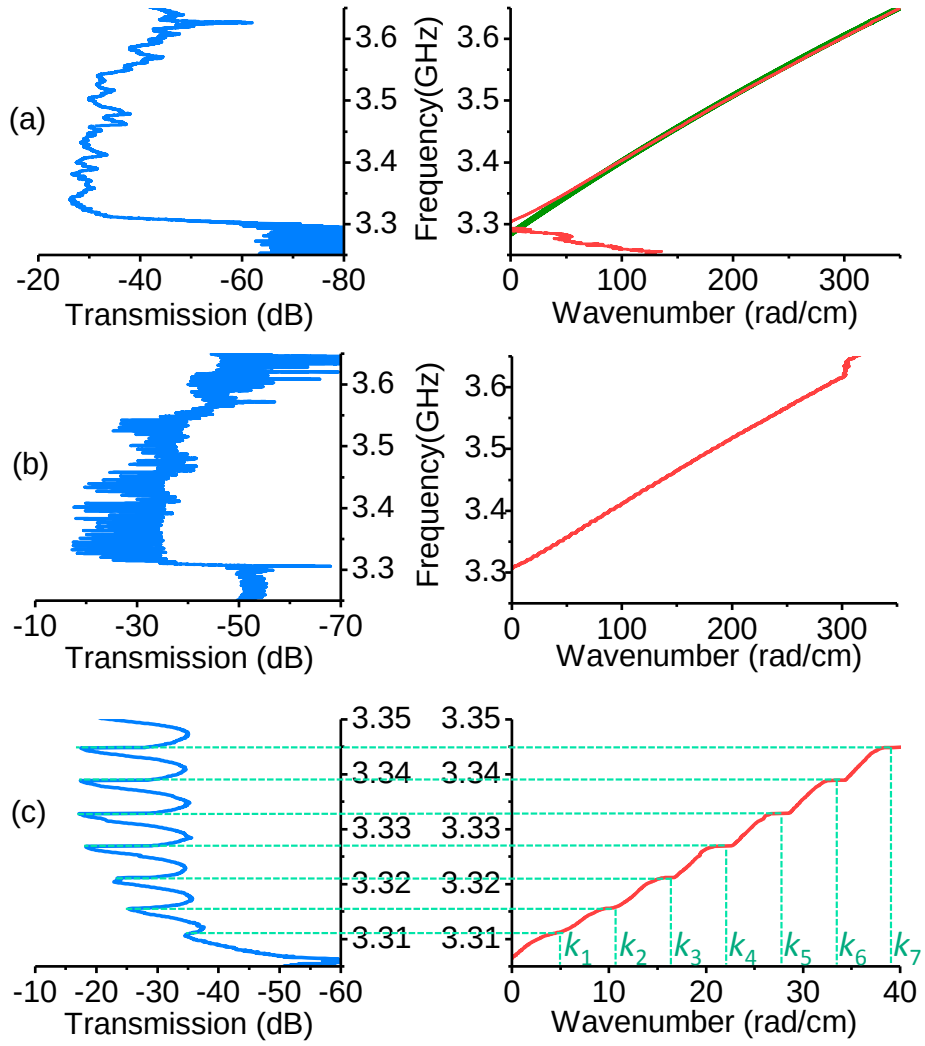

Figure 4.2 (a) Transmission profile (left) and spin-wave dispersion curve (right, red) for a YIG strip. (b) Amplitude-frequency response (left) and spin-wave dispersion curve (right) for a YIG strip-based ring. (c) The same data as in (b) shown in smaller frequency scales. The green curve in (a) is a theoretical fit. The vertical dashed lines in (c) indicate the wavenumbers of the ring eigenmodes.

namely, L=0, and thereby start to self-generate in the ring. The data in Figs. 4.2(b) and (c) were taken at L=1.0 dB, at which there is no self-generation in the ring. Note that in the experiment

one varies L by changing the attenuation of the adjustable attenuator. The larger the L is, the weaker the ring signal is.

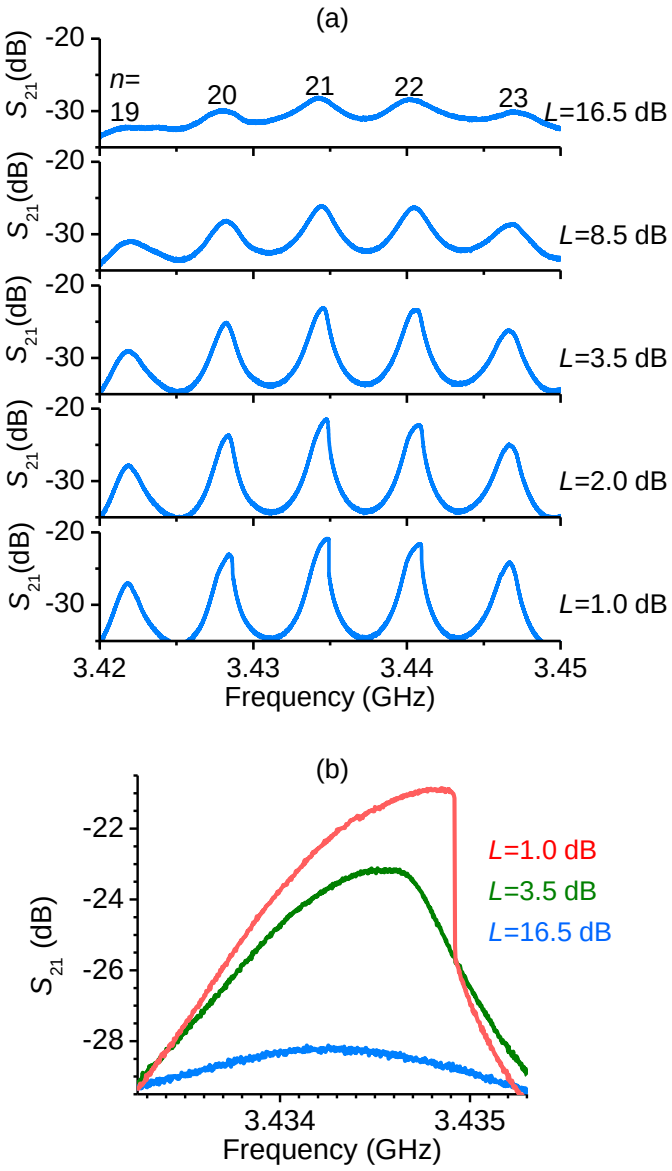

Figure 4.3 Foldover of ring eigenmodes. (a) Ring amplitude-frequency responses measured at different ring overall net loss (L) levels. (b) Amplitude-frequency responses for the n=21 eigenmode measured at three L levels.

Figure 4.3 presents the key results of this work. Figure 4.3(a) shows the effects of the ring net loss L on the ring amplitude-frequency response. The data show five ring resonant peaks,

with the eigenmode index given in the top diagram. These peaks are similar to those shown in the left diagram in Fig. 4.2(c), but for a different frequency range. Figure 4.3(b) shows the resonant peak for the "*n*=21" eigenmode for three different *L* levels, as indicated. One can see that the "*n*=21" peak is almost perfectly symmetric at *L*=16.5 dB and *L*=8.5 dB, evolves to an asymmetric peak at *L*=3.5 dB, and folds over to the high-frequency side at *L*=2.0 dB and *L*=1.0 dB. Very similar behavior can also be seen for the "*n*=20" and "*n*=22" peaks. In contrast, in comparison with these three peaks, the "*n*=19" and "*n*=23" peaks are relatively weak and do not show the same foldover response. Although not shown, similar results are observed for the resonant peaks in other frequency ranges. These results together evidently demonstrate the nonlinear foldover effect of the ring resonances.

4.2 Numerical Modeling

The above-present foldover effect is associated with the nonlinearity-caused spin-wave frequency shift. Assuming $|u|^2$ as the power amplitude of the spin wave, one can write down the dispersion for the forward volume spin wave in the YIG strip as

$$\omega\left(k,|u|^2\right)=|\gamma|\sqrt{\left[H_0-4\pi M_s\left(1-|u|^2\right)\right]\left[H_0-4\pi M_s\left(1-|u|^2\right)\frac{1-e^{-kd}}{kd}\right]} \tag{4.1}$$

where ω is the angular frequency of the spin wave. Note that the fitting of the experimental dispersion curve shown in Fig. 13(a) used Eq. (4.1) and assumed $|u|^2=0$. This assumption was made based on the fact that during the measurements the input power was low and the spin wave was weak, resulting in $|u|^2<<1$. It is evident from Eq. (4.1) that for a given *k*, an increase in $|u|^2$

leads to an increase in ω. This means that if the amplitude of the ring resonant peak becomes large, the peak shifts to higher frequencies. As the top of the peak shifts more than the edges of the peak, the net effect is the bending of the peak to the high-frequency side, giving rise to the foldover behavior.

It is important to highlight that the foldover shown in Fig. 4.3 is towards the high-frequency side, but in principle it is also possible to have a foldover to the low-frequency side. If one defines $N = \partial\omega / \partial\left(|u|^2\right)$ as the nonlinearity coefficient of a system, the sign of N dictates the direction of the foldover. Specifically, the resonant peaks fold towards the high-frequency side if $N>0$ and towards the low-frequency side if $N<0$. For the ring system shown in Fig. 4.1, one can flip the sign of N and thereby reverse the foldover direction simply by rotating the magnetic field to the film plane. For the field-in-plane configuration, the YIG strip supports backward volume spin waves for a field along the YIG strip length and surface spin waves for a field perpendicular to the strip length, both with $N<0$.

The heating of the YIG film can also lead to the foldover-like response. This is because the heating can cause a decrease in $4\pi M_s$, which in turn can result in an increase in ω according to Eq. (4.1). This, however, is not the case for the data presented above. Figure 4.4(a) compares the two amplitude-frequency responses in the ring: the blue curve was measured at L=8.0 dB and shows no foldover, while the red curve was measured at L=0.5 dB and exhibits clear foldover behavior. One can see that in comparison with the peaks in the blue curve, the three stronger peaks in the red curve fold to the right and are also shifted to higher frequencies, while the other two peaks showing no foldover do not have any notable frequency shifts. These results indicate the absence of any heating effects. In the case that the YIG film is heated and $4\pi M_s$ is reduced, one would expect that all the five peaks, not just the three stronger ones, in the red curve shift to higher

frequencies. Note that the absence of heating is very likely considering the fact that the ring had an overall net loss (L>0) and was operated below the self-generation regime.

Further, the presented foldover effect is not associated with the nonlinear interactions of the spin waves. The three-wave interactions are prohibited as mentioned above, while the four-wave interactions are absent as indicated by Fig. 4.4(b). In Fig. 4.4(b), the red curve shows the ring amplitude-frequency response measured at L=0.5 dB, while the vertical dashed lines indicate a uniformly spaced frequency comb which is expected if the two strongest modes undergo four-wave interactions and produce three new modes with relatively weak intensities.[55] One can see that the first and second dashed lines from the left clearly deviate from the centers of the two resonant peaks on the left. This result confirms the absence of the four-wave interactions. If L<0, the four-wave interactions may take place and result in a sequence of modes that are equally spaced in the frequency domain, as demonstrated previously.[42,44] To better understand the physics underlying the foldover effect in feedback ring systems, theoretical calculations were carried out to reproduce the experimental observations. Referring to the ring system shown in Fig. 4.1 and considering a signal A_{in} input to the left directional coupler, after the signal passes through the amplifier and then the YIG strip, it appears at the output of the right directional coupler as

$$A_{\text{out}} = A_{\text{in}} \beta G \left[\eta_e \left(e^{ikl} e^{-\xi_{sw} l} \right) \eta_d \right] \beta \tag{4.2}$$

where β denotes the loss for the directional coupler to transfer a signal into or out of the ring and G is the gain provided by the amplifier. The square bracket term in Eq. (4.2) describes the change of the signal in the transducer-YIG-transducer structure, where η_{e} and η_{d} describe the attenuations

[55] M. Remoissenet, *Waves Called Solitons: Concepts and Experiments* (Springer, Berlin, 1999), 3rd ed.

due to the excitation and detection transducers, respectively, and ξ_{sw} denotes the spatial decay rate of the spin wave. For convenience, the term $\eta_e e^{-\xi_{sw} l} \eta_d$ is replaced by a single attenuation

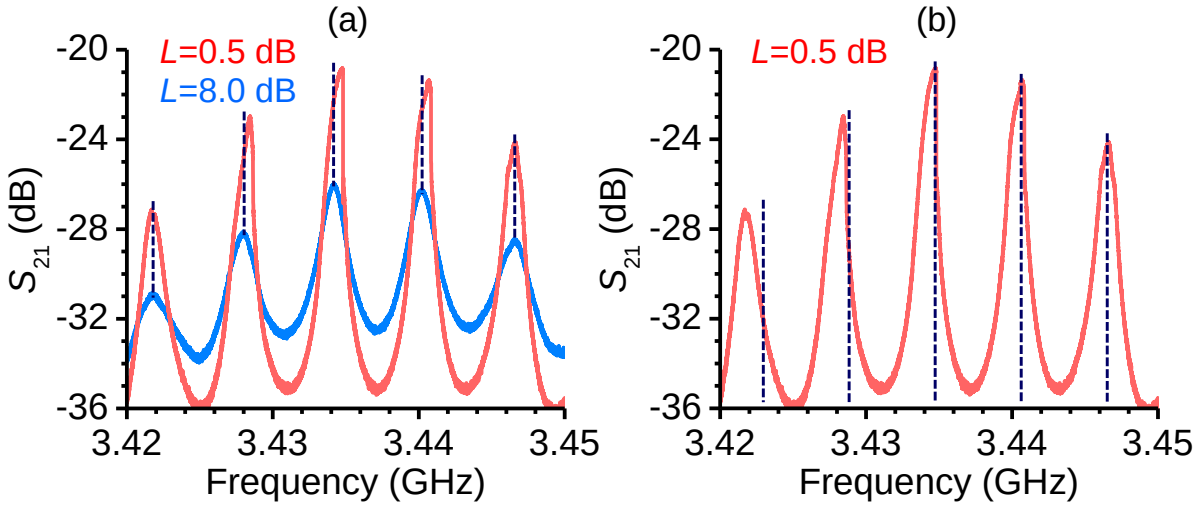

Figure 4.4 (a) Two ring amplitude-frequency responses measured at different net loss levels. The dashed lines indicate the peak frequencies of the blue curve. (b) A ring amplitude-frequency response (red curve) and a frequency comb expected for four-wave interactions (dashed lines).

parameter η in the discussions that follow. A_{out} in Eq. (4.2) is only a small portion of the signal from the YIG strip due to the relatively large loss β, while the majority of the signal propagates to the attenuator and the amplifier and then back to the YIG strip. The net effect is the continuous circulation of the signal in the ring and a signal at the output of the right directional coupler as

$$A_{out} = \sum_{n=1}^{\infty} A_{in} \beta \left[G \eta e^{ikl} \right]^n \left[(1-\beta) \alpha (1-\beta) \right]^{n-1} \beta \tag{4.3}$$

where (1-β) denotes the loss which the ring signal experiences every time it passes through the directional coupler, and α denotes the attenuation of the adjustable attenuator. From Eq. (4.3), one can define the complex ratio

$$\mathbf{S}_{21} = \frac{A_{out}}{A_{in}} = \sum_{n=1}^{\infty} \beta \left[G \eta e^{ikl} \right]^n \left[(1-\beta) \alpha (1-\beta) \right]^{n-1} \beta \tag{4.4}$$

Defining S_{21} as the amplitude of $\mathbf{S}_{21}$, $20\log(S_{21})$ corresponds to the ring amplitude-frequency response measured in the experiment. From Eq. (4.4), one can write S_{21} as

$$S_{21} = \sqrt{\left[\sum_{n=1}^{\infty} \beta^2 G^n \eta^n (1-\beta)^{2(n-1)} \alpha^{n-1} \cos(nkl)\right]^2 + \left[\sum_{n=1}^{\infty} \beta^2 G^n \eta^n (1-\beta)^{2(n-1)} \alpha^{n-1} \sin(nkl)\right]^2} \qquad (4.5)$$

Equations (4.1) and (4.5) together allow for the calculation of the amplitude-frequency response in the ring.

For the theoretical results presented below, the calculations used β=0.15 (-16.5 dB), G=1.78 (45 dB), and α=-(L+7) dB, which are all experimental values. In order to have the frequency positions of the calculated resonant peaks match those of the experimental peaks, the calculations used l=11.3 mm, which is slightly larger than the actual transducer separation. This adjustment was reasonable because the phase change due to the electrical circuit is not taken into account in Eqs. (4.3)-(4.5). Note that this phase change is much smaller than the change due to the spin-wave propagation (kl). The parameter η in Eq. (4.5) is frequency dependent and was determined using Eqs. (4.1) and (4.5) to fit the ring amplitude-frequency response measured at L=40 dB. The fitting assumed that $|u|^2$ was a constant ($|u_0|^2$) independent of ω. This assumption is justified because the amplitude-frequency response at L=40 dB is relatively flat and does not show interference patterns. Note that the "L=40 dB" amplitude-frequency response and its corresponding response in the k domain were used as a reference background in the calculations. The "S_{21} vs. ω" and "S_{21} vs. k" responses can be translated to each other using Eq. (4.1).

The calculations involve the following steps. One first uses Eq. (4.5) to calculate the S_{21} vs. k response for a given L. Then, one obtains $(|u|^2-|u_0|^2)$ as a function of k by examining the difference between the calculated S_{21} vs. k response with the background S_{21} vs. k response mentioned above. Next one uses the $(|u|^2-|u_0|^2)$ vs. k response and Eq. (4.1) to calculate the

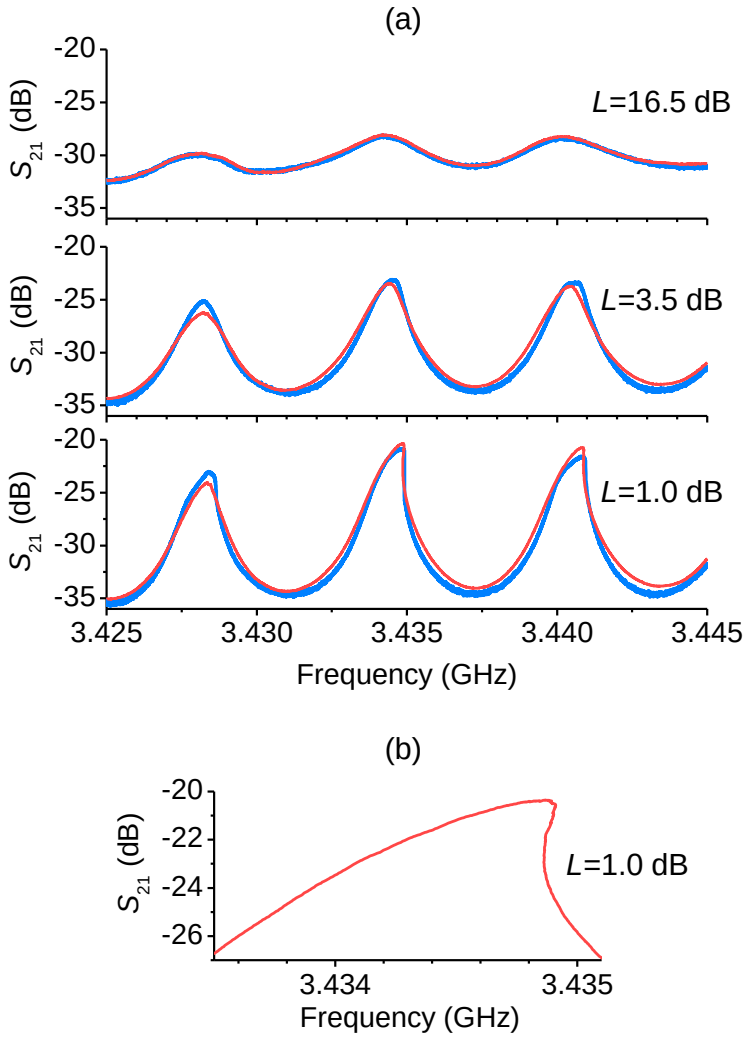

Figure 4.5 Comparison of experiments and calculations. (a) Experimental (blue) and theoretical (red) ring amplitude-frequency responses for three different ring net loss (L) levels. (b) Calculated amplitude-frequency response for L=1.0 dB.

corresponding ω vs. k response. By comparing the ω vs. k response with the S_{21} vs. k response, one finally obtains S_{21} as a function of ω for a particular L.

Figure 4.5 shows representative theoretical results. Figure 4.5(a) compares the calculated amplitude-frequency responses (red curves) with the experimental responses (blue curves) for three *L* levels, as indicated. Figure 4.5(b) shows the same red curve in the bottom diagram in (a), but in a much smaller frequency scale. It is evident that there is an almost perfect agreement between the experimental and calculated responses. What's more, the curve in Fig. 4.5(b) shows the rolling over of the top part of the peak, which is inherent but cannot be demonstrated experimentally. These results clearly justify the above-discussed physical origin of the foldover effect. Note that for the data shown in Figs. 4.3-4.5, the measurements were carried out by sweeping the frequency from low to high, and the amplitude jumped down from a high value to a lower value at the foldover. If the frequency is swept from high to low, it is expected that at the foldover the amplitude would jump up from a low value to a higher value at a frequency slightly lower than that for the down jump, resulting a hysteresis. This hysteresis response was not measured as the frequency sweeping direction was limited in the experiment. However, it is intrinsic and can easily be imaged with the help of the foldover shown in Fig. 4.5(b).

4.3 Summary

In summary, the foldover effect was observed for nonlinear resonances in a YIG thin film strip-based active feedback ring. The amplitude vs. frequency response in the ring showed resonant peaks developed from ring eigenmodes. With an increase in the resonance amplitude, those resonant peaks evolved from symmetric peaks to asymmetric ones and then folded over to higher frequencies. To understand these results, theoretical calculations were carried out that took into account the nonlinearity of the spin waves. The calculated results almost perfectly

agree with the experimental observations, confirming that the observed foldover effect originated from the nonlinearity-produced spin-wave frequency shift. The effect is not associated with either heating or the nonlinear parametric interactions of different spin waves, as evident by experimental data.

CHAPTER 5

Observation of Envelope Dispersive Shock Waves in Yttrium Iron Garnet Thin Films

In nonlinear media where the dispersion dominates over the dissipation, an initial abrupt increase in a physical quantity of the media (for example, the density of a superfluid and the amplitude of water waves) can evolve into an expanding waveform that consists of a leading soliton followed by a diminishing soliton-like train which terminates in weak dispersive waves. Such a wave train is referred to as a dispersive shock wave (DSW).[56] It is a ubiquitous phenomenon in nature, appearing in dispersive media as diverse as the ocean,[57,58] nonlinear optical media,[59,60] rarefied plasma,[61] intense electron beams,[62] and ultra-cold atoms.[63,64] In terms of mathematical description, DSWs are often modeled by the Korteweg–de Vries (KdV) equation or the nonlinear Schrödinger (NLS) equation.[56] The NLS equation is needed for the

[56] G. A. El and M. A. Hoefer, Physica D, in press (2016). (http://dx.doi.org/10.1016/j.physd.2016.04.006).
[57] G. A. El and M. A. Hoefer, arXiv:1601.01071v2 [nlin.PS] (2016).
[58] T. Talipova, E. Pelinovsky, O. Kurkina, and A. Kurkin, Hindawi Publishing Corporation, Shock and Vibration, Article ID **875619**, 7 (2015).
[59] W. Wan, S. Jia, and J. W. Fleischer, Nature Phys. **3**, 46 (2007).
[60] S. Jia, W. Wan, and J. W. Fleischer, Phys. Rev. Lett. **99**, 223901 (2007).
[61] D. R. Baker and H. Ikezi, Phys. Rev. Lett. **24**, 206 (1970).
[62] I. A. Bush, A. P. L. Robinson, R. Kingham, and J. Pasley, Plasma Phys. Ctrl. Fusion **52**, 125007 (2010).
[63] A. M. Kamchatnov, A. Gammal, and R. A. Kraenkel, Phys. Rev. A **69**, 063605 (2004).
[64] J. J. Chang, P. Engels, and M. A. Hoefer, Phys. Rev. Lett. **101**, 170404 (2008).

DSWs that result from modulations of a carrier wave and therefore cannot be described with the KdV approach.

The NLS model predicts that an initial, steep increase in the amplitude of a carrier wave with repulsive or defocusing nonlinearity can develop into an envelope DSW that consists of oscillations with both the amplitude and width increasing from the front to the back and is terminated by a dark soliton.[56,65] Further, the model also predicts that the derivative profile of the DSW phase oscillates too, with the oscillation period and amplitude both increasing as one goes from the front to the back. Such predictions have never been demonstrated experimentally in any nonlinear media yet.

This chapter reports the experimental observation of envelope DSWs for spin waves in magnetic thin films. The experiments used surface spin waves in a magnetic $Y_3Fe_5O_{12}$ (YIG) thin film strip that had a repulsive nonlinearity. The spin waves were excited by placing a microstrip transducer at one end of the YIG strip and feeding it with microwave signals, and were detected by a secondary transducer at the other end of the strip. An abrupt jump in the spin-wave amplitude was realized by inputting a microwave step pulse in which the power increases sharply at the step. The features of the excited nonlinear spin waves are dictated by the power levels right before and after the step. In a certain power regime, pronounced DSW excitations were observed that consisted of a train of dark soliton-like dips with increasing depths and terminated with a black soliton, as predicted by the NLS model. The phase derivative profile showed oscillations whose frequency decreased and amplitude increased, also as predicted. These results represent the first experimental demonstration of envelope DSWs in repulsive nonlinear systems. The results will

[65] M. A. Hoefer, M. J. Ablowitz, I. Coddington, E. A. Cornell, P. Engels, and V. Schweikhard, Phys. Rev. A **74**, 023623 (2006).

not only advance the fundamental understanding of universal DSWs in general, but will also help the interpretation of many effects such as turbulence and de-coherence in the NLS systems, which include surface ocean waves, waves in electromagnetic transmission lines, and light waves in optical fibers, in addition to the spin waves concerned here.

5.1 Experimental Configuration

Figure 5.1(a) shows a schematic diagram of the experimental setup. The setup includes a long and narrow YIG thin film strip and two microstrip line transducers placed on the top of the YIG strip for the excitation and detection of spin waves. The YIG film strip is magnetized to saturation by an external magnetic field which is in the plane and perpendicular to the length of the YIG film strip, as indicated. This film/field configuration supports the propagation of surface spin waves[66, 15] whose nonlinearity is repulsive or defocusing.[16] For the DSW measurements, the excitation transducer is fed with a microwave step pulse that is produced by merging the signals from two phase-locked microwave sources. One of the microwave sources provides a weak signal that abruptly goes to zero at a certain time, while the other produces a relatively strong signal whose amplitude jumps rapidly to a larger value at the time the weak signal goes to zero. Such a microwave pulse excites a spin-wave step pulse in the YIG strip, and the latter is then probed by the detection microstrip transducer. The output signals from the detection transducer are measured directly with a fast oscilloscope, without using any microwave amplifiers or diodes.

[66] P. Kabos and V. S. Stalmachov, *Magnetostatic Waves and Their Applications* (Chapman and Hall, London, UK, 1994).

For the experimental data presented below, the YIG film strip was 1.3 mm wide and 36.5 mm long. It was cut from a larger single-crystal YIG wafer grown on a gadolinium gallium garnet substrate by liquid phase epitaxy. The magnetic field was set to 1323 Oe. The microstrip line transducers were 50 μm wide and 2 mm long and were end-shorted. The separation of the two transducers (l) was set to 20.8 mm. The input microwave signals applied to the excitation transducer were step pulses whose power was P_1 right before the step and P_2 right after, as indicated in Fig. 5.1(a). During the measurements, P_1 and P_2 were varied over a range of 1 μW–80 mW, but the carrier frequency was fixed to f_0=6.045 GHz.

Figures 5.1(b), 5.1(c), and 5.1(d) show the characteristics of the YIG device shown in Fig. 5.1(a). Figure 5.1(b) presents the transmission response, namely, the amplitude of the S-parameter $\mathbf{S_{21}}(f)$, measured at a microwave power level of 20 μW over a frequency (f) range of 5.75-6.30 GHz. In Fig. 5.1(c), the blue curve presents the spin-wave dispersion curve determined from the phase of $\mathbf{S_{21}}(f)$, namely, $\Phi(f)$, while the red curve shows a theoretical fit to the spin-wave dispersion equation. To obtain the experimental dispersion curve, the spin-wave wavenumber $k(f)$ was calculated from $k(f)$ using the relation $\Phi(f)=k(f)l+\Phi_0$ (Φ_0, a phase constant) and taking k=0 at the low cut-off frequency f_{cut} = 5.792 GHz of the transmission. The theoretical fitting used [15,16]

$$2\pi f = |\gamma|\sqrt{H_0\left(H_0 + 4\pi M_s\right) + \left(\tfrac{1}{2}4\pi M_s\right)^2\left(1 - e^{-2kd}\right)} \tag{5.1}$$

where $|\gamma|$ is the absolute gyromagnetic ratio, H_0 is the magnetic field, $4\pi M_s$ is the effective saturation induction of the YIG film, and d is the YIG film thickness. The horizontal dotted and dashed lines in Figs. 5.1(b) and 1(c) indicate the locations of f_0 and f_{cut}, respectively. Figure 5.1(d) gives the output power as a function of the input power measured at f_0. The shaded area indicates the P_2 range in which pronounced DSW excitations were observed.

The data in Fig. 5.1(b) indicate a spin-wave passband from 5.79 GHz to about 6.20 GHz, in which f_0 is located in about the middle. The transmission profile is relatively smooth. This

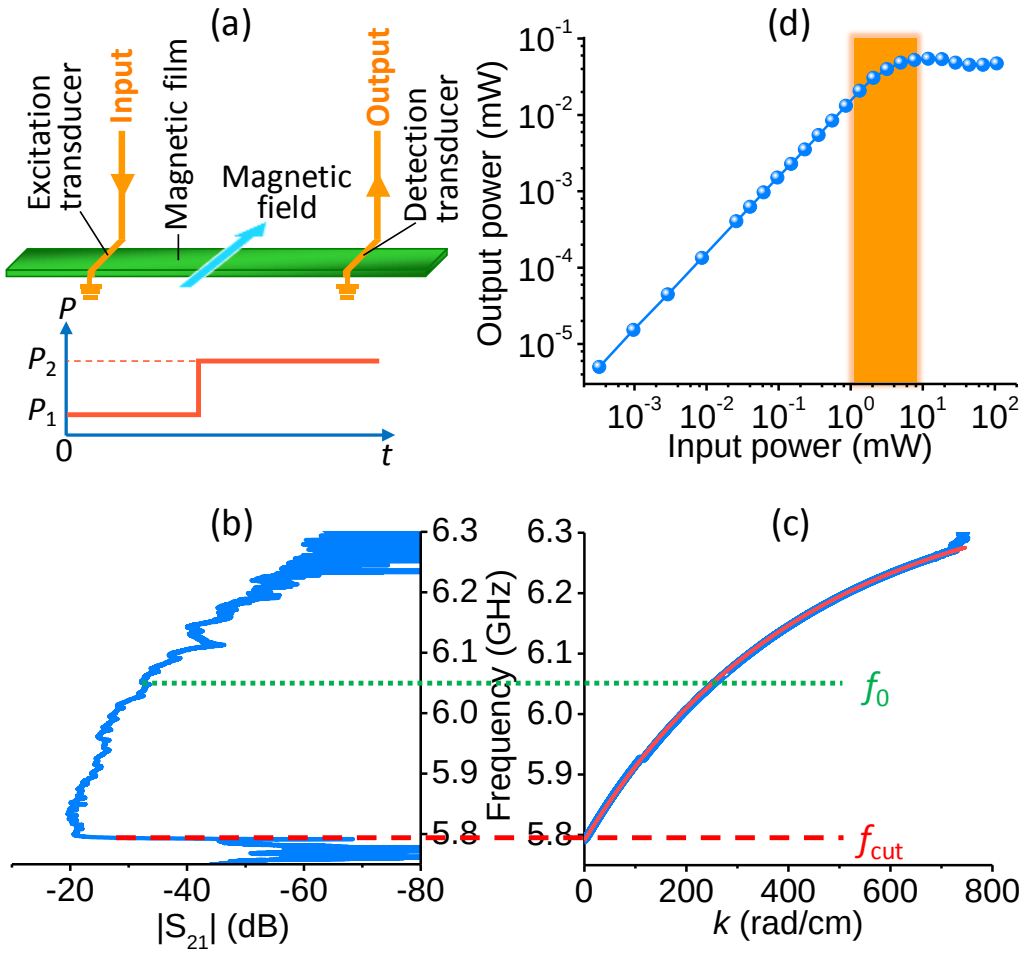

Figure 5.1 Experimental configuration and spin-wave characteristics. (a) Schematic of the experimental setup. (b) Transmission response of the YIG film strip device measured at an input power of 20 μW. (c) Experimental (blue) and theoretical (red) dispersion curves of spin waves in the YIG film strip. (d) Output power of the YIG film strip device measured as a function of the input power at 6.045 GHz.

indicates that the spins on the YIG film surfaces are unpinned and a repulsive nonlinearity is expected for the entire 5.79-6.02 GHz frequency range. In films with strongly pinned surface

spins, one has a repulsive nonlinearity only in narrow frequency ranges.[67,68] The fit in Fig. 5.1(c) is nearly perfect. The fitting yield $|\gamma|$=2.88 MHz/Oe, $4\pi M$s=1870 G, and d=11.0 μm. The $|\gamma|$ value is close to the standard value (2.80 MHz/Oe). The $4\pi M_s$ value is slightly larger than the bulk value (1750 G), and this difference is mainly due to the assumption of a zero anisotropy field in Eq. (5.1). One usually describes the dispersive characteristics of a wave by defining a dispersion coefficient as

$$D = \frac{\partial^2(\omega)}{\partial k^2} \tag{5.2}$$

Using the experimental dispersion curves in Fig. 5.1(c), one obtains D = -11.8×10^3 cm^2/(rad/s) at f_0=6.045 GHz. This value is very close to the theoretically calculated value which is -11.3×10^3 cm^2/(rad/s). The data in Fig. 5.1(d) indicate that the spin wave is linear in the 10^{-4}-10^0 mW input power range but is highly nonlinear for the input power higher than 10 mW. The nonlinearity here derives mainly from four-wave interactions in terms of nonlinear waves, or four-magnon scattering in terms of quantum language.[16,69]

5.2 Experimental Results and Discussions

Turn now to the DSW experimental data, which are presented in Figs. 5.2-5.5. Figure 5.2 shows the main results of this work that demonstrate for the first time the envelope DSW for repulsive nonlinear spin wave systems. Figures 5.2(a) and 5.2(b) present the input and output

[67] B. A. Kalinikos and A. N. Slavin, J. Phys. C: Solid State Phys. **19**, 7013 (1986).
[68] B. A. Kalinikos, N. G. Kovshikov, and A. N. Slavin, Zh. Eksp. Teor. Fiz. **94**, 159 (1988).
[69] A. D. Boardman and S. A. Nikitov, Phys. Rev. B **38**, 11444 (1988).

signals, respectively. In both figures, the top and bottom diagrams present the amplitude and phase profiles, respectively. The phase profiles show the phase values relative to the phase of a continuous wave with a frequency the same as f_0=6.045 GHz. In Fig. 5.2(c), the top diagram shows the square of the amplitude data in Fig. 5.2(b), the middle diagram shows the same phase data in Fig. 5.2(b), and the bottom diagram presents the time derivative of the phase profile in the middle diagram. Note that the time scales in Figs. 5.2(a) and 5.2(b) are the same but are smaller in Fig. 5.2(c). The red curve shows a fit to the square of a black soliton envelope profile[70]

$$u(t) = u_0\sqrt{1-\operatorname{sech}^2\left[u_0 v_g\sqrt{\frac{N}{D}}(t-t_0)\right]} \tag{5.3}$$

where u denotes the spin-wave amplitude, u_0 is the spin-wave amplitude for the black soliton background, v_g is the group velocity, N is the nonlinearity coefficient, and t_0 is a time constant. The fitting used v_g=5.0×10^6 cm/s and N=-2.9×10^9 rad/s, which were both calculated with the experimental parameters. Here u_0 and t_0 are two fitting parameters and were taken to be 3.28×10^{-2} and 277 ns, respectively, for the fit shown in Fig. 5.3(c). The vertical dashed line in Fig. 5.3(c) indicates the location of the black soliton center. All the data in Fig. 5.3 were taken at P_1=0.81 mW and P_2=3.47 mW.

The data in Fig. 5.2 clearly indicate that an envelope DSW is formed that consists of a train of dark soliton-like dips, with the width broadening and the depth increasing from the front to the back, and is terminated with a black soliton. The black soliton has an almost zero amplitude at its center, a profile that can be fitted nicely with the standard black soliton function Eq. (5.3), and a phase jump of 175° at its center which is very close to 180°. All of these three features are the

[70] M. Remoissenet, *Waves Called Solitons: Concepts and experiments* (Springer, Berlin, 1999).

signatures of envelope black solitons. The fact that the DSW is terminated by a black soliton, not a gray soliton, indicates the formation of a vacuum point right before the large jump. The derivative of the phase profile in Fig. 5.1(c) shows a notable oscillation behavior, with both the

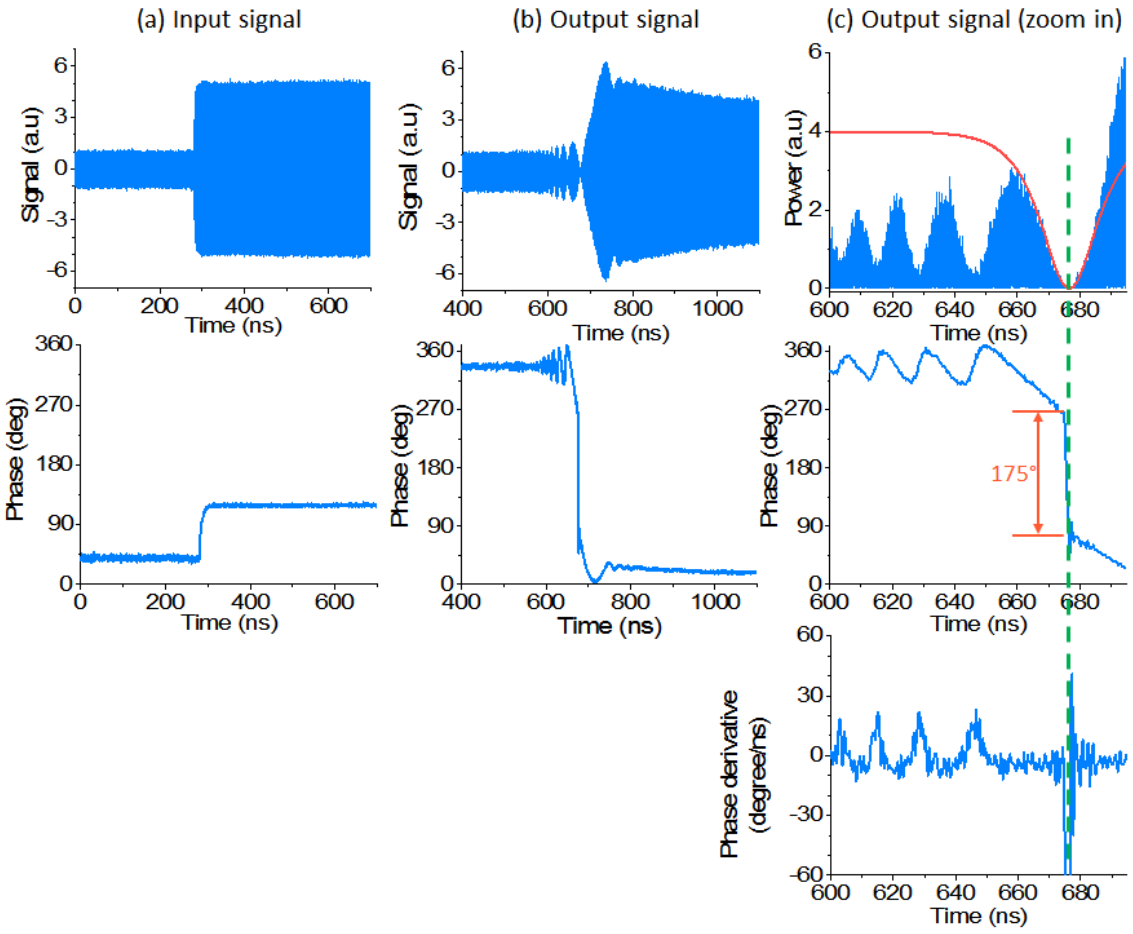

Figure 5.2 Demonstration of an envelope DSW. (a) Input signal: top – amplitude; bottom - phase. (b) Output signal: top – amplitude; bottom - phase. (c) Zoom-in display of the output signal shown in (b): top – power (amplitude square); middle – phase; bottom – phase derivative. The red curve in (c) shows a numerical fit to a black soliton profile.

oscillation period and amplitude increasing from the front to the back. Note that in the bottom diagram in Fig. 5.1(c), the values at the black soliton center are beyond the vertical scale. These observations confirm for the first time the NLS predictions reported in Refs. [56] and [65].

Figures 5.3 and 5.4 show further data that show that the formation of the DSW excitations is sensitive to the characteristics of the spin-wave steps, the same as other types of shock waves. Figure 5.3 presents the data measured with the power P_2 fixed at 3.47 mW while the ratio P_2/P_1

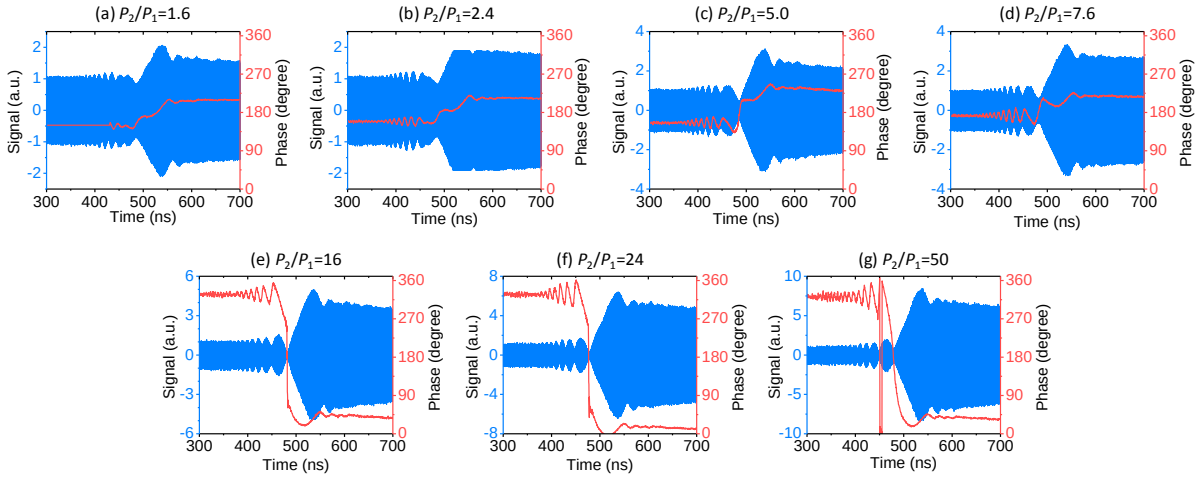

Figure 5.3 Dependence of DSW formation on P_2/P_1. In each diagram, the signal is shown in blue while the phase is shown in red; the P_2/P_1 ratio is indicated on the top. For all the measurements, P_2 was fixed at 3.47 mW.

ranged from about 1.6 to 50. One can see that the DSW is fully developed at P_2/P_1=16 and 24, characterized by a black soliton right before the large amplitude jump. When the ratio is lower than 16 or higher than 24, the DSW is under-developed. This result indicates that the amplitude of the jump is important for the DSW development. This importance derives from the fact that at the jump, the group velocity and dispersion coefficient of the spin wave, which are both critical parameters for the DSW formation vary due to nonlinearity-produced dispersion curve shift. Figure 5.4 shows the data measured when P_1 and P_2 were both increased but their ratio was kept constant at P_2/P_1≈24. It is evident that the DSW is pronounced when P_1=0.14 mW and P_2=3.47

mW but is not at other power levels, indicating that appropriate nonlinearity is a pre-requisite for the formation of the DSW.

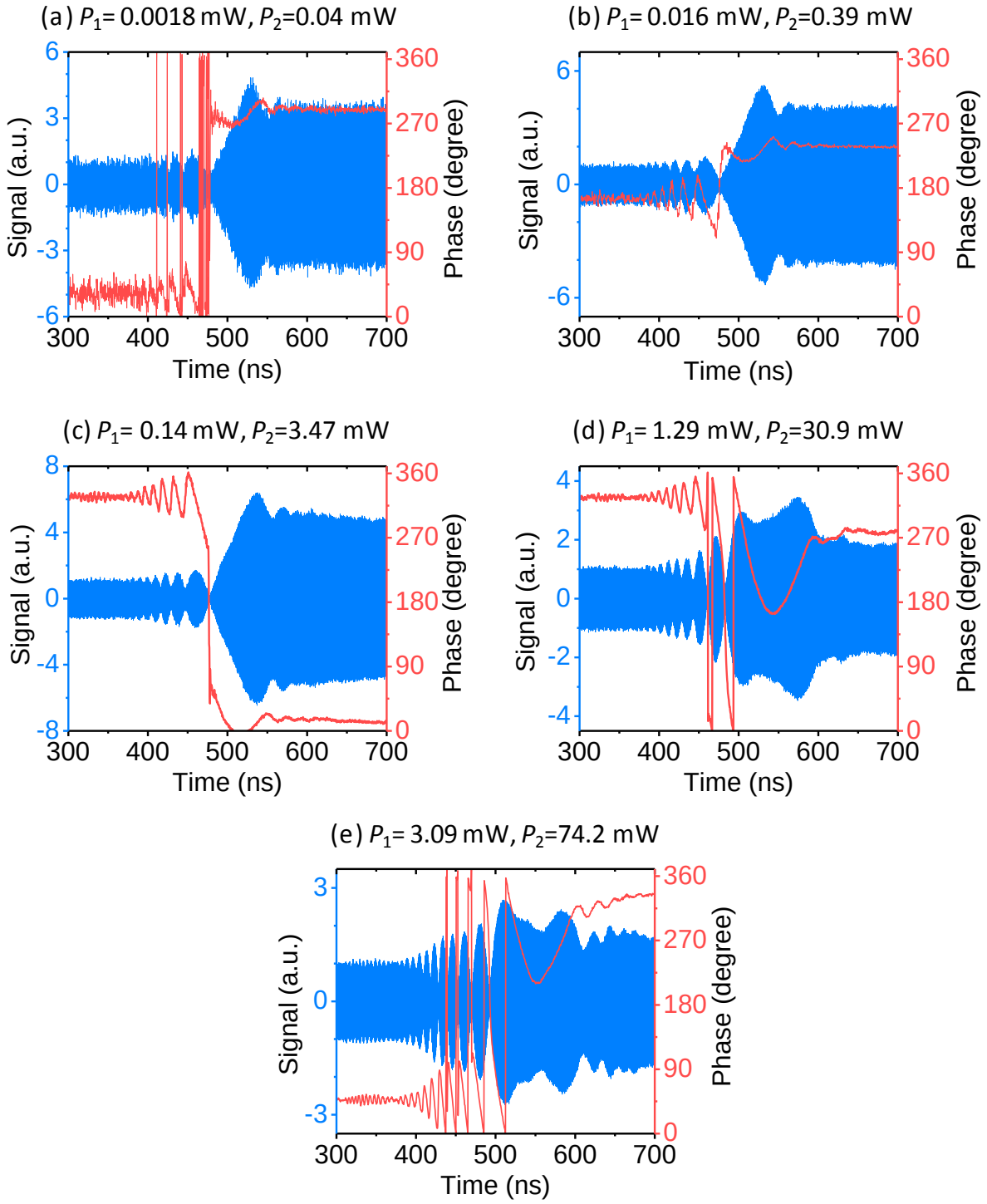

Figure 5.4 Dependence of DSW formation on P_1 and P_2. In each diagram, the signal is shown in blue while the phase is shown in red; the input power levels are indicated on the top. For all the measurements, the P_2/P_1 ratio was kept constant at about 24.

Figure 5.5 presents the data measured at different positions (x) along the spin-wave propagation. In contrast to those shown in Figs. 5.1-5.4, these data were obtained using a scan-able inductive probe,[71,72] not a microstrip line transducer. The data clearly indicate how an initial spin-wave step gradually evolved into a DSW during its propagation along the YIG film strip. The DSW became fully developed at x=4.5 mm, as shown in the middle diagram in Fig. 5.5. The fact that the DSW formation needs a certain propagation length is because the spin-wave nonlinearity takes a certain propagation time or distance to develop.[73,74] Note that the signal after the step has an amplitude of about 4.5, which is beyond the vertical axis scale. Note also that, different from the black solitons shown in Figs. 5.2-5.4, the dark solitons in the DSW excitations in Fig. 5.5 do not show nearly zero intensity at their center. This is mainly because the inductive probe dimension is larger and is therefore less sensitive than the microstrip transducer, resulting in the smoothing of the time-domain signals.

[71] M. Wu, M. A. Kraemer, M. M. Scott, C. E. Patton, and B. A. Kalinikos Phys. Rev. B **70**, 054402 (2004).
[72] V. Eisler and Z. Zimborás , New J. Phys. **17**, 053048 (2015).
[73] N. G. Kovshikov, B. A. Kalinikos, C. E. Patton, E. S. Wright, and J. M. Nash, Phys. Rev. B **54**, 15210 (1996).
[74] M. Chen, M. A. Tsankov, J. M. Nash, and C. E. Patton, Phys. Rev. B **49**, 12773 (1994).

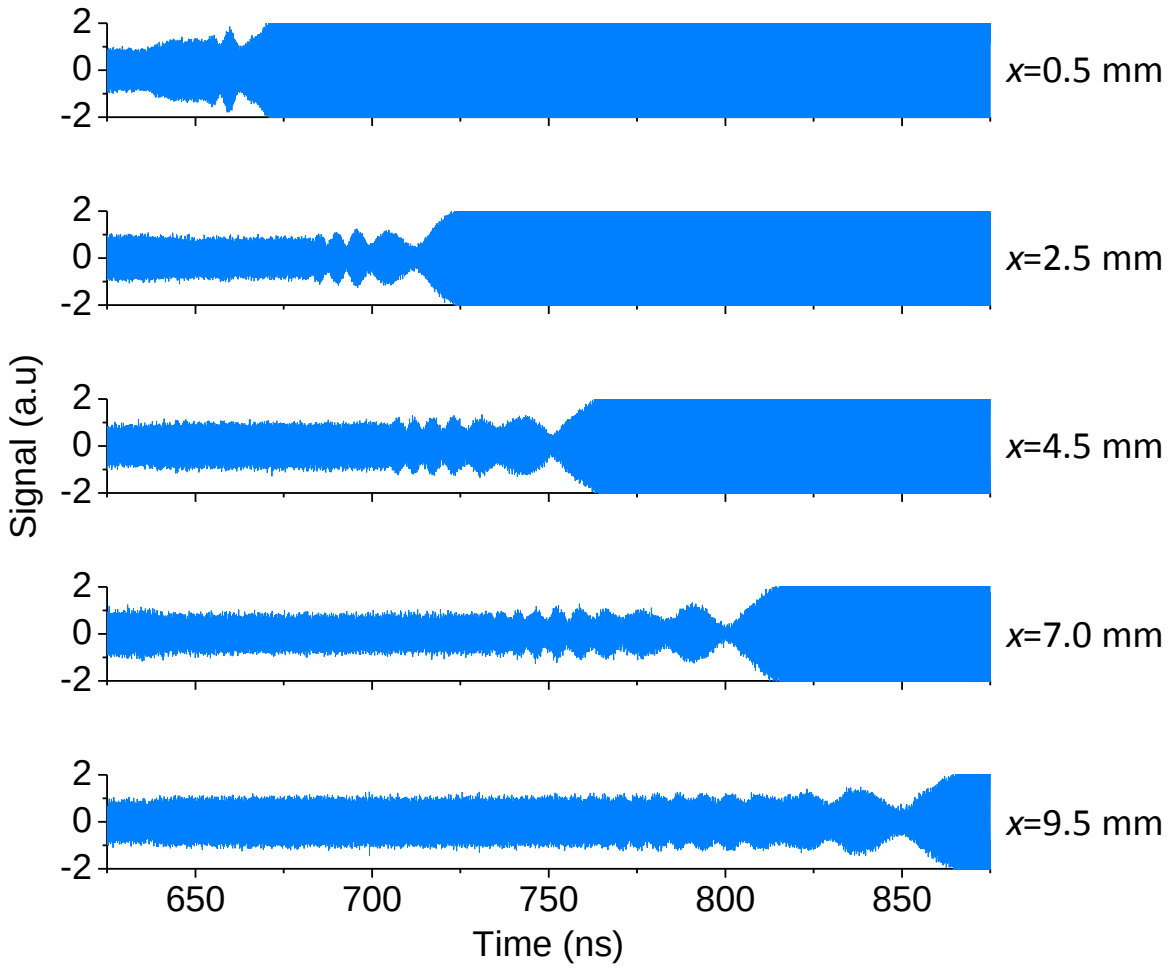

Figure 5.5 Spatial development of DSW. Each diagram shows the spin-wave signal measured by an inductive probe at a distance of x away from the excitation transducer. The measurements were carried out at P_1=0.14 mW and P_2=3.47 mW.

5.3 **Summary**

In summary, this work demonstrates envelope DSWs for surface spin waves in YIG thin film strips. The DSW consists of a train of dark soliton-like dips with both the width and depth increasing from the front to the back and is terminated by a black soliton with its center intensity close to zero and its phase jumping close to 180°. The formation of such DSW excitations is

sensitive to the characteristics of the initial spin-wave step pulse. It also takes a certain propagation distance for the initial step pulse to evolve into a DSW. Future work is of great interest that makes use of the NLS model and the experimental parameters to reproduce these experimental results. Future work is also very interesting that demonstrates similar DSW phenomena in other NLS systems, including surface ocean waves, waves in electromagnetic transmission lines, and light waves in optical fibers.

CHAPTER 6

Spin Pumping due to Traveling Spin Waves

In this chapter, an experimental study on spin pumping due to nonlinear surface spin waves is presented. In ferromagnetic material/heavy metal bi-layer structures like YIG/Pt, magnetic excitation in the ferromagnetic material can induce a flow of angular momentum into the adjacent heavy metal layer.[75,76] This is known as a spin pumping. The spin pumping in turn gives rise to a spin current in the heavy metal which, due to strong spin orbit coupling, can give rise to an ISHE voltage.[77,78]

This phenomena provides a means to turn magnetic excitations in insulators into electric signals. This possibility to couple spin dynamics in an insulator to electrons in a metal plays a major role in the newly developed area of technology called spintronics. The main idea behind spintronics is to develop more energy efficient logic and computational devices that could replace the conventional electronic devices.[79,80,81,82] Because of the extremely low damping and the rich

[75] B. Heinrich, C. Burrowes, E. Montoya, B. Kardasz, E. Girt, Young-Yeal Song, Yiyan Sun, and Mingzhong Wu, Phys. Rev. Lett. **107**, 066604 (2011).
[76] V. Castel, N. Vlietstra, B. J. van Wees, and J. Ben Youssef, Phys. Rev. B **86**, 134419 (2012).
[77] J. E. Hirsch, Phys. Rev. Lett. **83,** 1834 (1999).
[78] S. O. Valenzuela and M. Tinkham, Nature **442**, 176 (2006)
[79] A. V. Chumak, V. I. Vasyuchka, A. A. Serga and B. Hillebrands, Nature Phys. **11**, 453 (2015).
[80] J Wang, H Meng, and J-P Wanga, J. Phys. **97**, 10D509 (2005).
[81] M. P. Kostylev, A. A. Serga, T. Schneider, B. Leven, and B. Hillebrands, Appl. Phys. Lett. **87**, 153501 (2005).
[82] S. A. Wolf, D. D. Awschalom, R. A. Buhrman, J. M. Daughton, S. von Molna, M. L. Roukes, A. Y. Chtchelkanova, D. M. Treger, Science. **294**, 1488 (2001).

dispersive properties, YIG[83] has been identified as a material of choice for many of these applications.[79, 81] Despite the fact that spin waves in YIG demonstrate characteristics that are attractive for many applications, the nonlinear properties of spin waves complicate this picture and need to be studied carefully.[84,85]

Apart from spintronics, the fact that the spin pumping induces voltage can also be used as a technique to probe the magnetic excitations in ferromagnetic materials, to gain more insight about magnetic excitations such as spin waves.

The importance of the work presented here is twofold. Firstly, the ISHE voltage produced in a YIG/Pt bi-layer structure due to microwave induced spin pimping, in a wide range of magnetic field and microwave frequency, is studied. Several distinct magnetic field and frequency ranges, where the ISHE voltage is strong and weak, were identified. A clear nonlinear behavior in the ISHE signals is seen, which adds to the versatility of spin waves and opens up a new degree of freedom for the design of spintronic devices.

Secondly, the nonlinear behavior of the ISHE voltage is explained under the framework of the so-called three-wave nonlinear splitting. The careful study of the nonlinear behavior of the ISHE voltage has in return provided new information about the threshold power that is required for the three-wave nonlinear splitting. Though some studies had already been carried out to better understand the three-wave nonlinear splitting,[86,87] most of those studies have been focused on narrow frequency and magnetic field ranges. The data presented in this chapter cover almost the

[83] C. Kittel, Introduction to Solid State Physics (Wiley, New Jersey, 2005).
[84] O. Bu¨ttner, M. Bauer, S. O. Demokritov, and B. Hillebrands, Phy. Rev. Lett. B **61**, 11576 (2000).
[85] V. E. Demidov, J. Jersch, K. Rott, P. Krzysteczko, G. Reiss, and S. O. Demokritov, Phy. Rev. Lett. **102**, 177207 (2009).
[86] C. L. Ordóñez-Romero, B. A. Kalinikos, P. Krivosik, W. Tong, Pavel Kabos, and C. E. Patton, Phys. Rev Lett. B **79**, 144428 (2009).
[87] C. Mathieu, V. T. Synogatch, and C. E. Patton, Phys. Rev. Lett. B **67**, 104402 (2003).

entire passband of the surface spin waves, accessible to commonly used 50 µm wide microstrip transducers, in a wide magnetic field range.

The experiment was carried out with the use of a 9.7-µm-thick YIG strip which was partly covered with Pt, in surface spin wave configuration. Section 6.1 provides the experimental details and the observations. The experimental observations were understood in the framework of the three-wave nonlinear splitting, and a discussion on the qualitative explanation of the experimental data is presented in section 6.2. Finally section 6.3 gives a summary of the work.

6.1 Experimental Configuration

A suitable YIG/Pt bi-layer sample was prepared for the experiment. For this purpose a narrow YIG thin film strip was used on which a rectangular section at the middle was covered by a thin layer of Pt. As the first step, a 2.0-mm-wide and 45-mm-long, high-quality, single-crystal YIG strip grown by standard liquid phase epitaxy was papered. The ends were cut in a roughly 45° angle to the length, to avoid the reflections of spin waves. With the use of two microstrip transducer structures and a vector network analyzer, the transmission data ($\mathbf{S}_{21}$) of the YIG strip was measured as a function of the frequency. Figure 6.1 presents the characteristics of the YIG strip. During the measurements, the microstrip transducers were held 10 mm apart and the YIG strip was placed on top of them with the YIG side facing down and touching the transducers. Figure 6.1 shows the transmission coefficient data ($\mathbf{S}_{21}$) measured as a function of frequency (f). The left diagram shows the amplitude vs. frequency response, namely, the amplitude of $\mathbf{S}_{21}(f)$. In the right diagram, the green curve presents the spin-wave dispersion determined from the phase of

$\mathbf{S}_{21}(f)$, while the blue curve shows an analytical fit that was made to the spin-wave dispersion using equation, Eq. (6.1).

$$\omega(k) = \sqrt{\omega_H(\omega_H + \omega_M) + \frac{\omega_M^2}{4}(1 - e^{-2kd})} \tag{6.1}$$

To obtain the experimental dispersion curve, the spin-wave wavenumber $k(f)$ was calculated from the phase of experimental $\mathbf{S}_{21}(f)$, namely, $\Phi(f)$, using the relation $\Phi(f)=k(f)l+\Phi_0$ where l is the distance between the two microstrip transducers and Φ_0 is a phase constant. The calculation took k=0 at the low cut-off frequency f = 4.78 GHz of the transmission.

The data indicate that the spin waves in the YIG film have a passband of about 4.78-5.2 GHz.

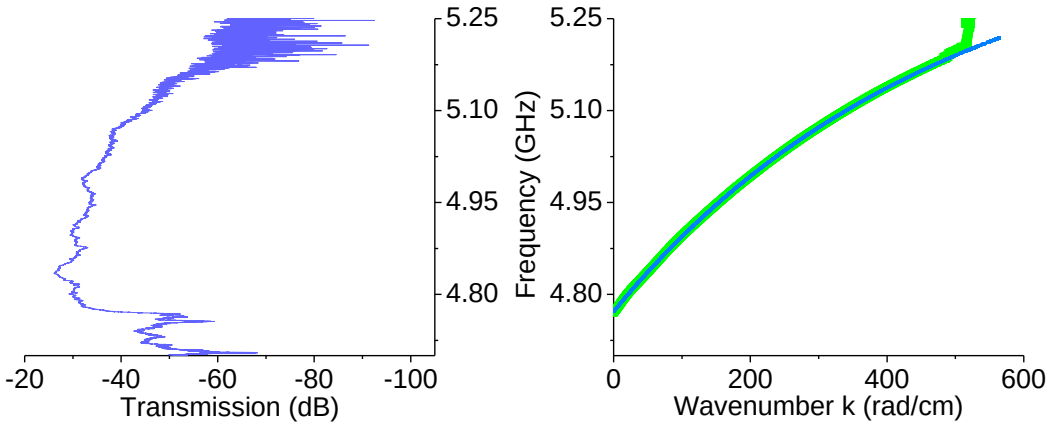

Figure 6.1 Transmission profile (left) and spin wave dispersion curve (right) for a YIG thin film strip.

The calculations used $|\gamma|$=2.8 MHz/Oe and $4\pi M_s$=1850 G. The fitting parameters were H_0 and d. For the fit given in Fig. 6.1(a), one has H_0=1015 Oe and d=9.7 μm. The field value obtained here is slightly smaller than the experimental value. Possible reasons for this difference include the errors in measuring H_0 and determining the low cut-off frequency of the spin wave and the assumption of zero anisotropy field in the YIG film. Note that for all the $\mathbf{S}_{21}$ measurements in this work, the signals from the vector network analyzer input had the same power, which was -17

dBm. This permits one to use Eq. (6.1) for the fitting. It should be noted that at this magnetic field the three-wave interaction is prohibited.

After the characterization, a thin Pt layer was deposited on the YIG strip covering a rectangular part of it at the center. Pulse laser deposition technique at room temperature was used for the Pt deposition. The Pt layer covered a 5.5 mm long section of the strip in its entire width and had a thickness of 20 nm and a resistance of 90 Ω. Finally, to measure the ISHE voltage across the Pt length direction, two Cu wires were attached to the two ends of the Pt strip with the use of high-purity silver ink.

The experimental setup, which is used to measure the ISHE voltage is schematically shown in Fig 6.2. It consisted of the YIG/Pt sample, with a microstrip transducer placed on top of the sample to excite spin waves in YIG, and a nano-voltmeter to measure the ISHE voltage. To obtain the strongest possible ISHE voltage signal, the following three directions should be orthogonal to each other: (1) direction of magnetization, (2) direction of spin pumping-produced spin flow, and (3) the Pt length along which the voltage is measured. Therefore, the YIG strip is magnetized by a magnetic field lying in the film plane perpendicular to the strip length. This film-field configuration supports the propagation of surface spin waves along the YIG strip and at the same time allows for three-wave nonlinear interactions at low enough magnetic fields.

When spin waves are excited in the YIG film, underneath the Pt layer, these magnetic excitations generate a spin current that flows from the YIG into the Pt.[75, 76] The spin current in turn, due to the ISHE[77, 78] produces a small electrical voltage in the Pt layer. This voltage is subsequently measured with the use of a nano-voltmeter.

The magnetic field is swept from 0 Oe to 1100 Oe in 12.4 Oe steps, while the frequency is swept from 20 MHz to 5 GHz in 10 MHz steps. The ISHE voltage is recorded for all the field and frequency values. For better visualization the data are presented in the form of color maps.

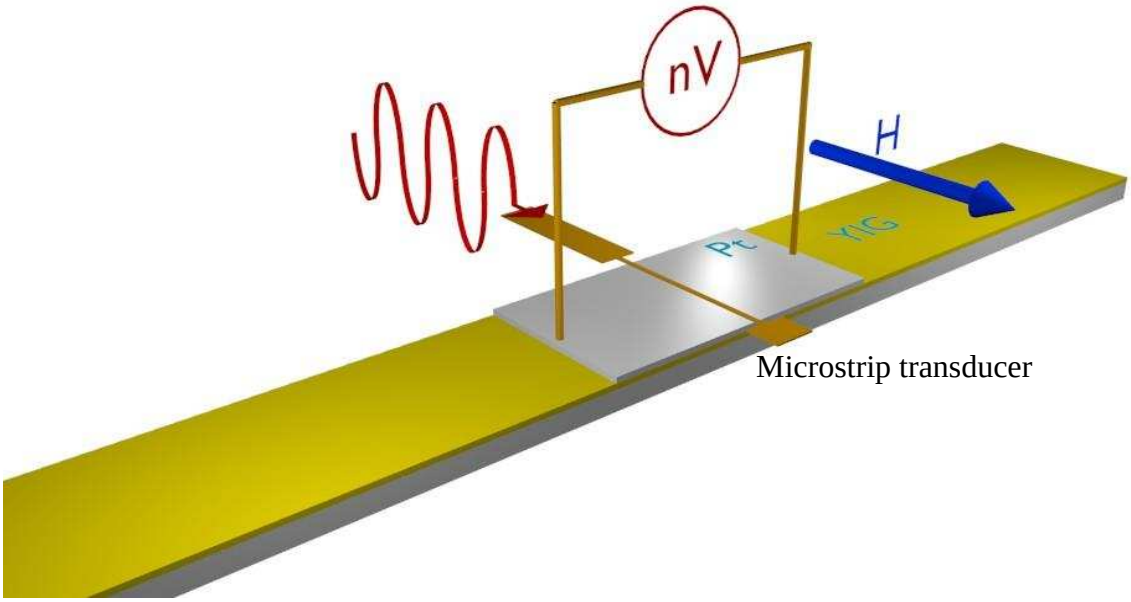

Figure 6.2 Schematic of the experimental setup for spin-wave-induced spin pumping measurements in YIG/Pt structures.

Figure 6.3 shows such a color map obtained for one of the data sets. The x-axis corresponds to the external magnetic field strength, the y-axis corresponds to the excitation frequency, and the color corresponds to the observed ISHE voltage (blue being no voltage and red a strong voltage) as indicated by the color bar. For these data the microwave power applied to the input transducer was set to 20 dBm.

Several key observations were made from the data presented in this ISHE voltage color map:

1) A prominent sharp line was observed in the middle of the ISHE voltage map, which started at the left bottom corner and stretched almost diagonally to the upper right corner. This signal was found to be corresponding to the uniform precession mode or the FMR

frequency mode of the YIG strip (in the surface wave configuration). This agrees well with the Kittel equation.

2) Below the FMR frequency, no ISHE voltage is observed.

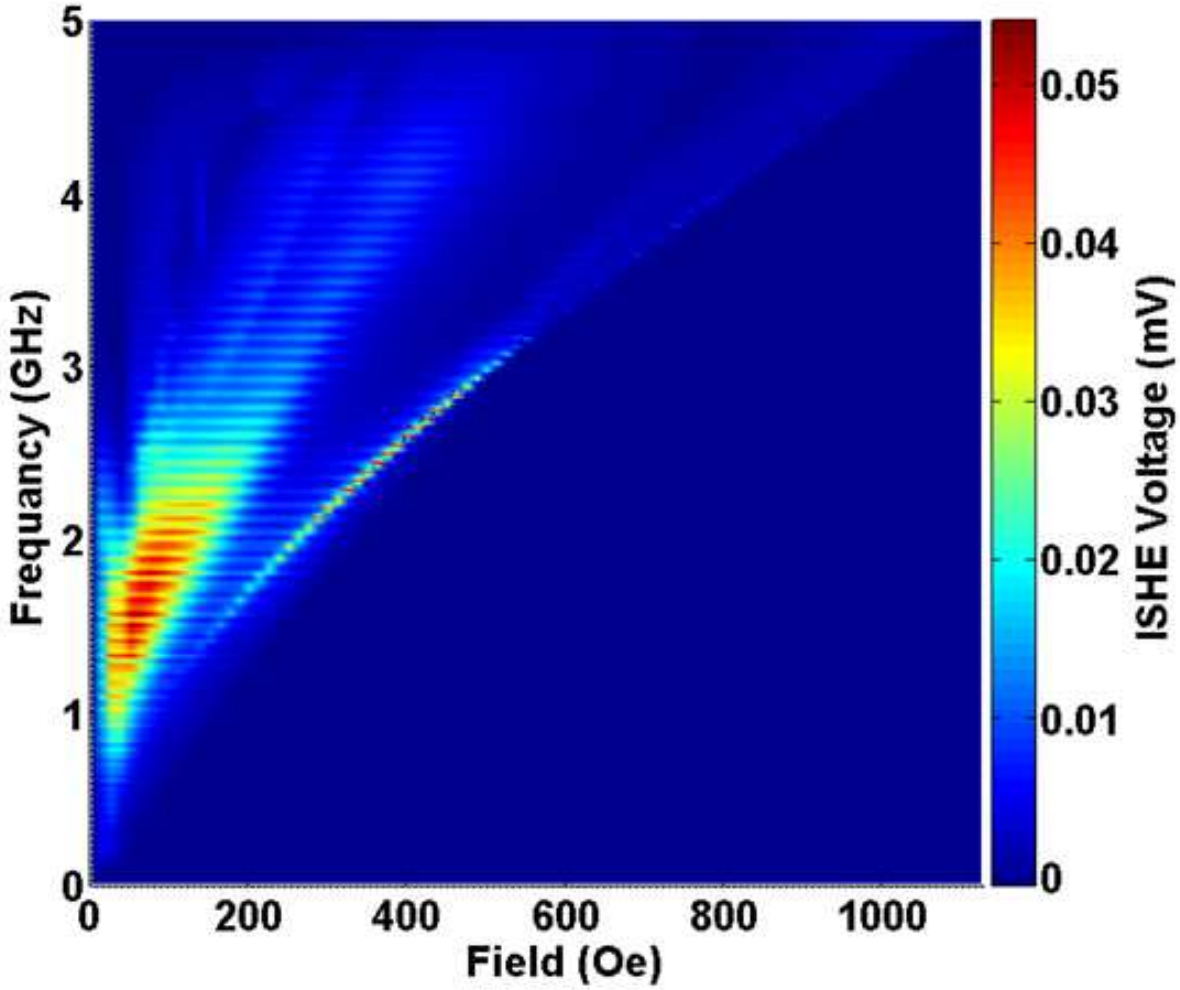

Figure 6.3 The color map constructed from the ISHE data.

3) Right above the FMR frequency, no ISHE voltage is observed, and this region with no voltage signal grows wider along the frequency axis with an increase in the magnetic field.

4) At even higher frequencies (above the last mentioned region with no voltage), again a voltage signal is seen.

5) The strongest ISHE voltage is observed well-above the FMR frequency at low magnetic fields.

6) A vague upper cut-off frequency is observed at all magnetic field values above which the voltage signal drops drastically. This upper cut-off agrees well with the highest wave number spin waves that could be efficiently excited by the microstrip transducer.

To better understand the underlying mechanisms, the experiment is repeated for a second experimental configuration in which the microstrip transducer is placed outside of the Pt covered section of the YIG strip. For the purpose of clarity, the first configuration, where the microstrip antenna is placed on top of the Pt, will be called as configuration 1; the configuration with the microstrip antenna placed outside of the Pt region, will be called as configuration 2. Figure 6.4 shows the results from both the configurations with the corresponding configuration numbers and the microstrip transducer placements. The format of the color map is the same as that in Fig. 6.3.

The surface spin waves are non-reciprocal and efficiently propagate only in one direction close to the top surface of the YIG film.[15,16] Therefore, in configuration 2 it should be noted that the correct placement of the microstrip transducer, to the left or the right of the Pt covered section, depends on the magnetic field direction. For surface spin waves, the following three directions form a right handed set of axis: (1) the normal direction of the film plane, (2) the external field direction, and (3) the direction of the spin wave propagation close to the top surface of the YIG.[15,16] Therefore, when the microstrip transducer is placed outside of the Pt covered section, it is placed in such a way that the spin waves excited close to the top surface would efficiently propagate towards the Pt covered section. The separation of the microstrip transducer and the Pt covered section is about 2 mm.

In Fig. 6.4, the yellow dashed lines indicated as $2f_{min}$ correspond to twice the lowest backward volume spin wave frequency. The red dashed lines indicated as f_{FMR} correspond to the FMR frequency calculated with the Kittel equation.

The different regions in the color maps are marked with capital letters for better clarity and easy identification in the text. In the data obtained from configuration 2, while some of the

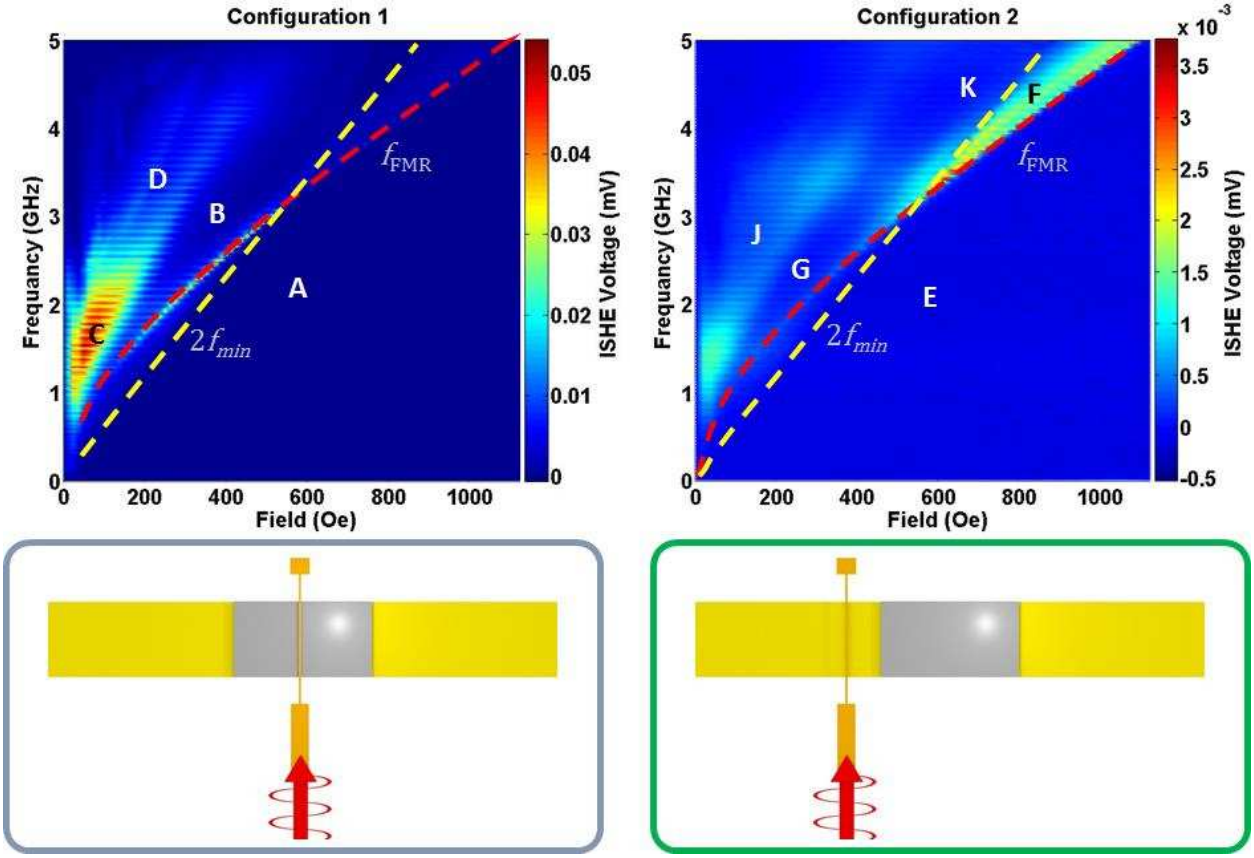

Figure 6.4 ISHE voltage maps and the antenna placement. (a) configuration 1, (b) configurattion 2.

features are the same as that from configuration 1, some differences should be noted.

1) The ISHE voltage signal that is observed is an order of magnitude smaller than that for configuration 1.

2) The curve that correspond to FMR is still present but very weak.

3) At higher fields an ISHE voltage signal is seen just above the FMR frequency, and it starts appearing only after a certain field strength (roughly 500 Oe). See region F.
4) The left part of region F has a very distinct wedge shape.
5) In the region where the signal is the strongest in configuration 1 (region C), a weak ISHE voltage signal is seen in configuration 2 (region J).
6) The strongest ISHE voltage signal for configuration 2 is observed in region F.

Observations (4) and (5) clearly distinguishes the results of configuration 1 from configuration 2. The physics behind these differences is discussed in detail below.

6.2 Experimental Results and Discussions

The ISHE voltage response seen in configuration 1 is clearly nonlinear. Despite the numerous efforts that were made to explain it in terms of different nonlinear phenomena the data from configuration 1 alone was not enough to obtain a clear picture of the specific mechanisms. As a result the experiment was repeated for configuration 2 to obtain more information about the physics behind the observations. In the data obtained from configuration 2, clear indications of the nonlinear three-wave splitting process is observed.

As it is explained in the material that follows, the data can be well understood under the frame work of three-wave interactions. As much as it provides valuable information about the different nonlinear regimes, which are important for spintronic device applications, this experiment also provides more insight into the three-wave processes and the different regions where it is most effective.

The effects are explained not in the order by which they are listed in section 6.1, but in the order that provides the most clarity. One important point that should be noted for the clear understanding of the data is the fact that, even though not strictly linear the ISHE voltage being produced is proportional to the strength of the magnetic excitations in the YIG film. That is a larger angle of precession in the YIG will result in a higher ISHE voltage in the Pt. The exact relationship between the ISHE voltage vs. the excitation power depends on the Pt and YIG thicknesses.[88]

The sharp line in the ISHE voltage map that begins at the bottom left corner at low fields and extends towards the upper right hand corner in Fig. 6.4 (which is also denoted as f_{FMR}) corresponds to the ISHE voltage produced due to the FMR mode in the YIG. This line agrees almost perfectly with the FMR frequency calculated using the equation, Eq. (2.13) with (k=0), shown by the red color dashed line. The region below the FMR frequency in both the configurations show no voltage. In this experiment, the magnetic field is in the film plane perpendicular to the YIG strip. This configuration supports surface spin wave propagation and does not support the backward volume spin wave propagation. The surface spin wave frequency pass band lies above the FMR frequency, while the backward volume spin wave frequency pass band lies below the f_{FMR}. Therefore no ISHE voltage signal in the region below the FMR frequency is due to the absence of the spin wave excitations in this region.

The voltage signal from configuration 2 is much weaker than that in configuration 1 and this can easily be understood by considering the strength of the magnetic excitation underneath the Pt in the two configurations. In configuration 1 the excitation from the antenna happens right

[88] V. Castel, N. Vlietstra, J. Ben Youssef, and B. J. van Wees, Appl. Phys. Lett. **101**, 132414 (2012).

underneath the Pt covered section, but in configuration 2 the spin waves are excited outside of the Pt covered section and spin waves travel ~2 mm before it reaches the Pt covered section. Due to the damping in the YIG, as the spin waves propagate in the ~2 mm distance, the spin waves attenuate exponentially.[15,16] Therefore, the magnetic excitations underneath the Pt in configuration 2 is significantly weaker than that in configuration 1. Therefore the ISHE voltage is significantly weaker in configuration 2. It should be noted that strictly speaking the FMR mode corresponds to the uniform precession and does not propagate, and the mode discussed here refers to the quasi-uniform spin wave that has a frequency very close to the FMR frequency and a wavenumber close to zero.

The clearest indication of the three-wave splitting is seen in the data from configuration 2. At higher magnetic fields, in configuration 2 region F an ISHE voltage signal is seen right above the FMR frequency. This signal starts appearing at a certain field strength (roughly 500 Oe), and at the beginning it is seen only in a small frequency range. As the magnetic field increases, the signal spreads wider along the frequency axis and shows a very distinct wedge shape that is enclosed between the two dashed lines, labeled as "f_{FMR}" and "$2f_{min}$". This by far is the clearest of indication of the three-wave process.

For magnons at the FMR frequency (f_{FMR}) the three-wave splitting is prohibited at higher magnetic fields. The absence of available spin wave modes at or below $f_{FMR}/2$ and therefore the inability to split into two new spin wave modes that will conserve both the energy and momentum are the reasons behind this. The same reasons hold true for surface spin waves as well. When the frequency of a surface spin wave lies below $2f_{min}$, the three-wave splitting for that spin wave is prohibited. Therefore, when $2f_{min}$ lies above the FMR frequency, the region sandwiched between f_{FMR} (red dashed line) and $2f_{min}$ (yellow dashed line) gives the range of frequencies for

which the three-wave splitting is prohibited. Therefore when the surface spin wave frequency lies in this range, the spin waves travel much further with no three-wave splitting-associated losses. As a result, the ISHE voltage is stronger. However, above this range (above $2f_{min}$) the three-wave splitting is allowed. For this reason, when the surface spin wave frequency is in this range (above $2f_{min}$), they experience relatively large losses due to the three-wave splitting-associated losses and thereby decay fast. This results in a weak or no signal in region K.

In configuration 1 region B, right above the FMR frequency at low fields, there appears a region with no ISHE voltage signal which widens along the frequency axis as the field increases. It is known that the surface spin wave frequency pass band starts at the FMR frequency and extends into higher frequencies. In accordance with this, an ISHE voltage is expected to be observed for the entire surface spin wave frequency pass band, which starts at the FMR frequency and extends into higher frequencies. This, however, is not observed. The discrepancy here can also be understood well in the frame work of the three-wave splitting. When the magnetic field is low (configuration 1 region B), since $2f_{min}$ lies below the FMR frequency, the conservation of energy and momentum can be satisfied in a three-wave splitting and the three-wave splitting can occur for all the surface spin wave frequencies. The reason for a weak ISHE voltage signal in region B is the weakening of the spin wave excitations due to the three-wave splitting-associated losses.

In Fig. 6.4(a) the strongest voltage signal, which appears in dark red, is observed between 1.2 GHz and 2.2 GHz for a field range of 50 Oe -150 Oe (configuration 1 region C). This observation raises an interesting question - why the ISHE voltage is strong even when the three-wave processes are allowed in this region? The reason for this is a fine balance between the group velocity, the precession angle, and the conditions required by the three-wave process. At the first glance, this seems to contradict the explanation given for configuration 1 region B. The discrepancy can be

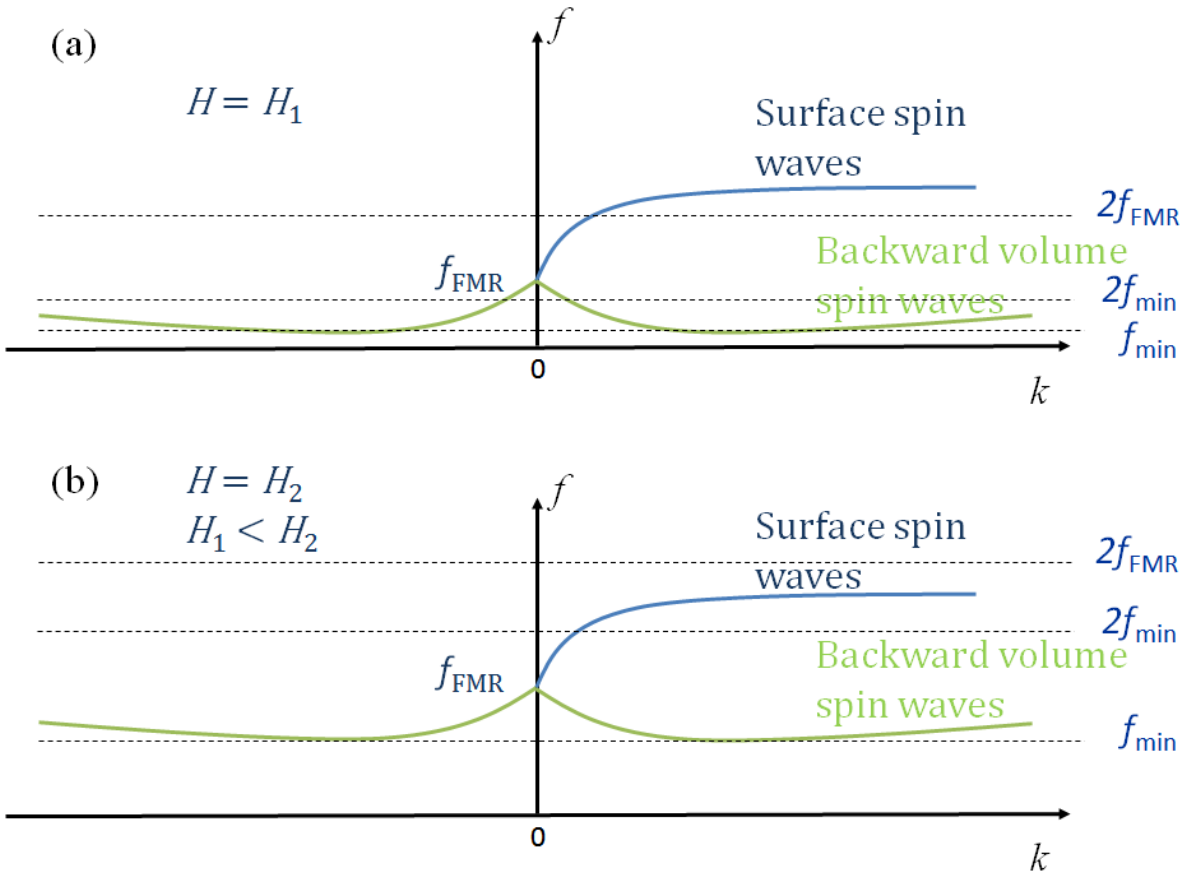

Figure 6.5 Qualitative pictures of dispersion curves for surface spin waves and backward volume spin waves for two different magnetic fields.

cleared out when all the factors that affect the three-wave splitting are considered. Specifically, in this region (configuration 1 region C), from the point of view of the energy and momentum conservations the three-wave splitting is allowed, but the threshold power required for the three-wave splitting to take place in this region is higher, as explained below.

Figure 6.5 (a) and (b) show dispersion curves for surface spin wave and backward volume spin wave excitations for two different magnetic fields H_1 and H_2, where $H_2 > H_1$. The x axis is the wavenumber k and the y axis is the frequency. In both (a) and (b) the frequency axes represent the same frequency range. All dispersion curves are qualitative curves and are made only for illustration purposes. Three dashed lines are drawn to indicate the following frequencies: (1) f_{min}

– the minimum frequency of the backward volume spin wave passband, (2) $2f_{min}$, and (3) $2f_{FMR}$. At the low magnetic field H_1 the FMR frequency, the surface spin wave passband, and the backward volume spin wave passband are all at lower frequencies; and at the higher magnetic field H_2, they are all at higher frequencies. Due to the non-reciprocal nature, the dispersion curve for the surface spin wave is shown only for the positive k values in both the graphs.[15,16] Because of the non-reciprocity of the surface spin waves, the creation of a surface spin waves with negative k values through the three-wave splitting is not allowed.

When the surface spin wave frequency is higher than $2f_{FMR}$, the three-wave splitting is prohibited. For this reason, the surface spin waves with frequencies larger than $2f_{FMR}$ does not suffer the losses due to the three-wave splitting, and an ISHE voltage signal is expected to be seen in the region where the frequency is $2f_{FMR}$ or higher.

Previous work has demonstrated that as the frequency of the secondary spin waves that are produced as a result of the three-wave splitting becomes closer to the FMR frequency, the threshold power needed for the three-wave splitting increases.[87] Therefore, even though the exact cut-off frequency for the three-wave splitting is at $2f_{FMR}$ (when only the energy and momentum conservations are considered), the efficiency of the three-wave splitting at relatively low excitation power levels (20 dBm in this experiment) should drop as it gets closer to $2f_{FMR}$, or in other words, the threshold power required for the three-wave splitting increases. Figure 6.6 shows the voltage map of Fig. 6.4 (a) with three dashed lines corresponding to: f_{FMR} (white dashed line), $2f_{FMR}$ (green dashed line), and $1.35f_{FMR}$ (red dashed line). In Fig. 6.6 a drastic increase in the ISHE voltage is seen above $1.35f_{FMR}$. This implies an absence of losses due to the three-wave splitting above $1.35f_{FMR}$.

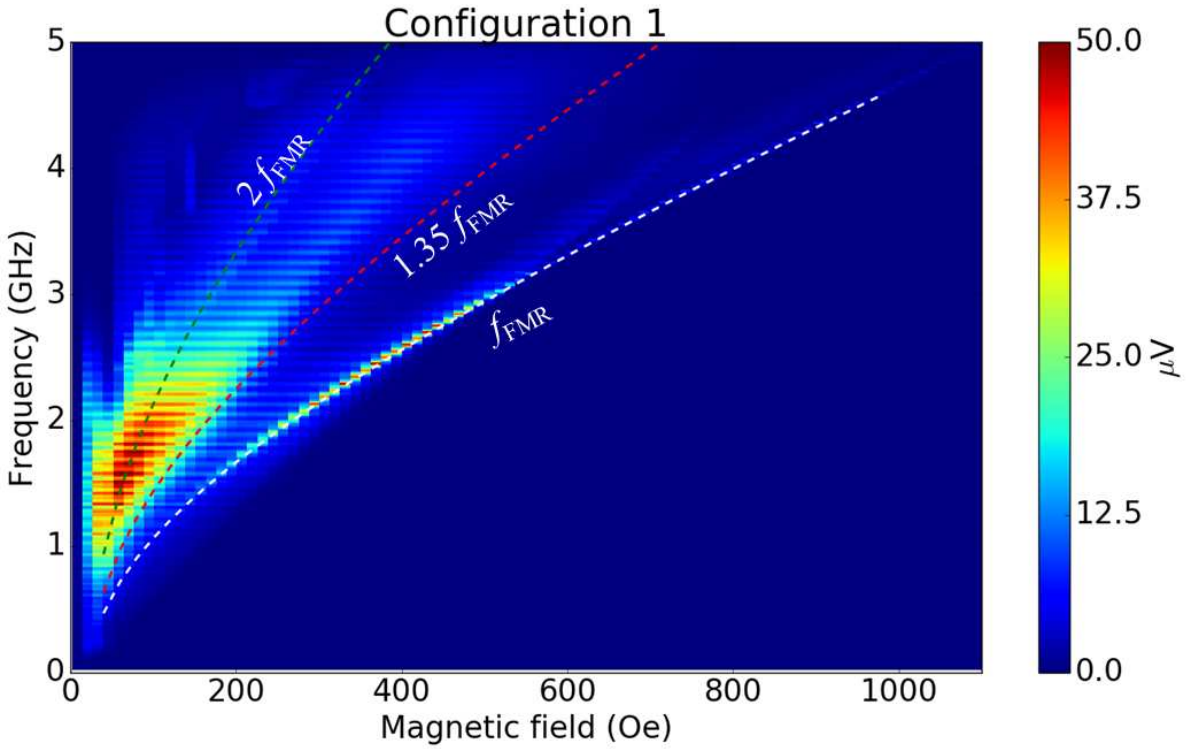

Figure 6.6 Comparison of the boundary of configuration 1 region C with different multiples of the FMR frequency.

To confirm this understanding, the experiment was repeated for four different power levels in configuration 1. For the data to be consistent with the above explanation, a narrowing of configuration 1 region B, is to be expected with a decrease in the excitation power. Figure 6.6 indicates that, when the excitation power is 20 dBm, this boundary is roughly at $1.35f_{FMR}$. If the excitation power is lowered, this boundary should move towards f_{FMR}.

Figure 6.7 shows the color maps that were obtained using four different input power levels which were 20 dBm, 15 dBm, 10 dBm, and 5 dBm. In all these figures the color range (blue to red) is normalized between the corresponding minimum and maximum ISHE voltages. The region that corresponds to configuration 1 region B, shrinks in size with decreasing the input power. The boundaries, above which the three-wave splitting stops, for the four different power levels, approximately correspond to $1.35f_{FMR}$, $1.316f_{FMR}$, $1.283f_{FMR}$, and $1.25f_{FMR}$. This confirms the

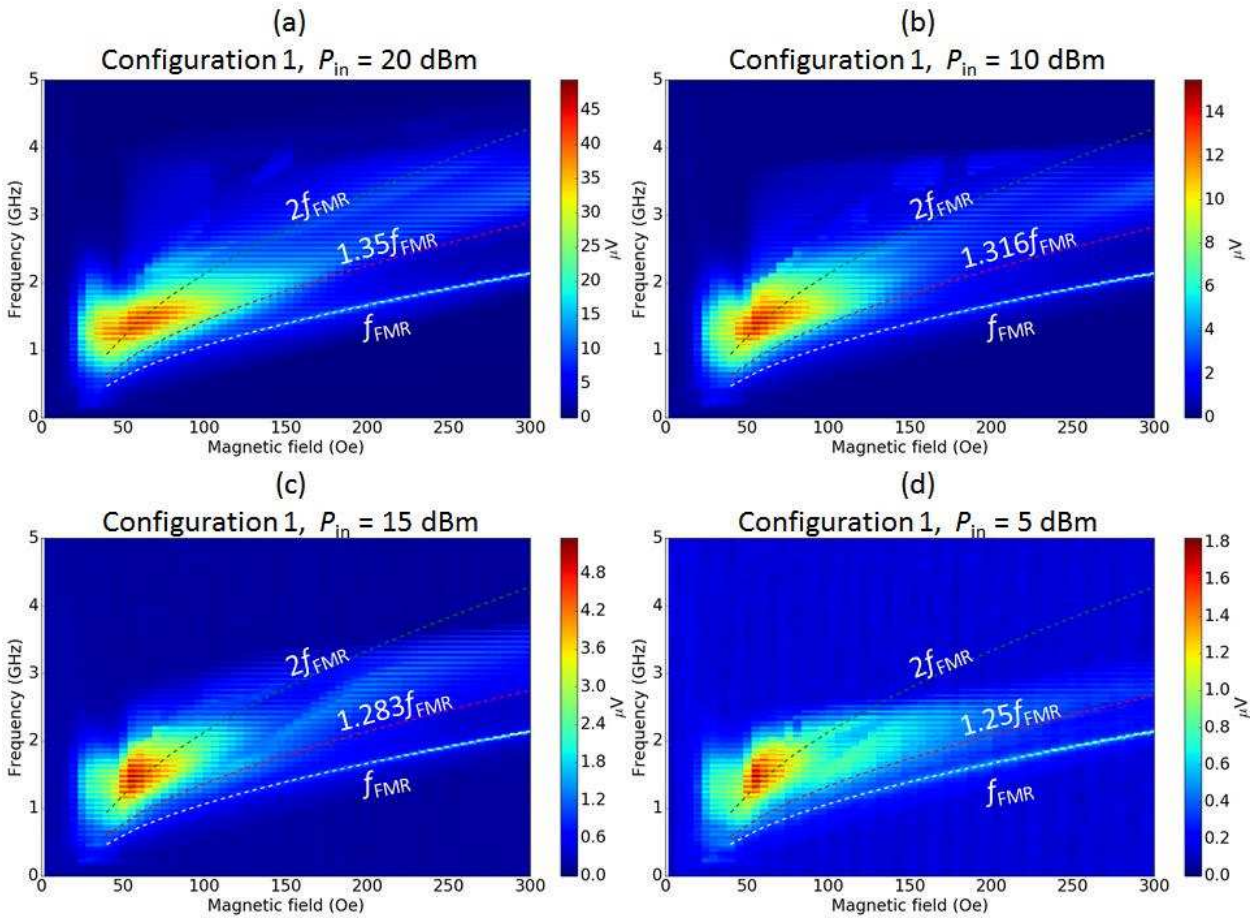

Figure 6.7 Color maps of the ISHE voltage for four different excitation power levels: (a) 20 dBm, (b) 15 dBm, (c) 10 dBm, and (d) 5 dBm.

explanation given above for configuration 1 region C. The strength of the ISHE voltage produced in the region, configuration 1 region C, is determined by two factors: (1) magnetic excitation strength (precession angle) and (2) the group velocity of the spin waves. At low fields the precession angle excited by a given excitation power, from the transducer, is larger than that at higher magnetic fields. The group velocity of the spin waves determines the rate at which the spin wave energy flows away from the antenna and the time which the spin waves spend underneath the Pt. Therefore, the dark red region in Fig. 6.4(a), region C, is believed to be due to the fine balance of the above two factors coming together to produce a very strong voltage.

6.3 Summary

In summary the spin pumping due to travelling spin waves in the surface spin wave configuration has been studied in a wide magnetic field range and a wide frequency range. The experiments were carried out in the nonlinear regime of the surface spin waves. It is observed that the ISHE voltage response of the system deviates significantly from what the linear theory predicts. As a result of these nonlinear effects several distinct regions emerged in the ISHE voltage color maps. The main reason for this behavior was identified as the nonlinear three-wave splitting process, which produces backward volume spin waves as a result of the annihilation of surface spin waves. The main features of these voltage maps were qualitatively understood in the frame work of the three-wave splitting and the standard spin wave theory. The results provide helpful information for the design and use of spintronic devices. This also opens a new degree of freedom for innovation, to design and build nonlinear spintronic devices. The data clearly indicate that the successful operation of any spintronic device in a surface spin wave configuration depends on the fine control of the operation power, apart from the right frequency and the right bias field. So far, to the best of my knowledge, there exists no analytical theory to model this regime of nonlinear surface spin waves. Therefore, this work also provides more information about the nonlinear three-wave splitting process to help develop a complete theory.

CHAPTER 7

Role of Damping in Spin Seebeck Effect in Yttrium Iron Garnet Thin Films

The SSE refers to the generation of a spin voltage in a ferrimagnet due to a temperature gradient. This spin voltage can produce a pure spin current in a heavy metal that is in contact with the ferrimagnet. The SSE was first discovered in ferromagnetic metals,[89,90,91] but not long after was also observed in magnetic insulators[92,93,94,95,96,97,98] and semiconductors.[99,100] The experiments usually utilize a ferrimagnet/heavy metal bi-layered hetero-structure with the magnetization in the ferrimagnet layer saturated in-plane and often take a longitudinal

[89] K. Uchida, S. Takahashi, K. Harii, J. Ieda, W. Koshibae, K. Ando, S. Maekawa, and E. Saitoh, Nature **455**, 778 (2008).
[90] K. Uchida, T. Ota, K. Harii, S. Takahashi, S. Maekawa, Y. Fujikawa, and E. Saitoh, Solid State Comm. **150**, 524 (2010).
[91] K. Uchida, H. Adachi, T. An, T. Ota, M. Toda, B. Hillebrands, S. Maekawa, and E. Saitoh, Nature Mat. **10**, 737 (2011).
[92] D. Qu, S. Y. Huang, J. Hu, R. Wu, and C. L. Chien, Phys. Rev. Lett. **110**, 067206 (2013).
[93] K. Uchida, J. Xiao, H. Adachi, J. Ohe, S. Takahashi, J. Ieda, T. Ota, Y. Kajiwara, H. Umezawa, H. Kawai, G. E. W. Bauer, S. Maekawa, and E. Saitoh, Nature Mat. **9**, 894 (2010).
[94] H. Adachi, K. Uchida, E. Saitoh, J. Ohe, S. Takahashi, and S. Maekawa, Appl. Phys. Lett. **97**, 252506 (2010).
[95] K. Uchida, T. Nonaka, T. Ota, and E. Saitoh, Appl. Phys. Lett. **97**, 262504 (2010).
[96] E. Padrón-Hernández, A. Azevedo, and S. Rezende, Phys. Rev. Lett. **107**, 197203 (2011).
[97] M. B. Jungfleisch, T. An, K. Ando, Y. Kajiwara, K. Uchida, V. I. Vasyuchka, A. V. Chumak, A. A. Serga, E. Saitoh, B. Hillebrands, Appl. Phys. Lett. **102**, 062417 (2013).
[98] D. Qu, S. Y. Huang, J. Hu, R. Wu, and C. L. Chien, Phys. Rev. Lett. **110**, 067206 (2013).
[99] C. Jaworski, J. Yang, S. Mack, D. Awschalom, J. Heremans, and R. Myers, Nature Mat. **9**, 898 (2010).
[100] C. M. Jaworski, J. Yang, S. Mack, D. D. Awschalom, R. C. Myers and J. P. Heremans, Phys. Rev. Lett. **106**, 186601 (2011).

configuration in which a temperature gradient is established along the thickness direction of the ferrimagnet/heavy metal structure.

Although a complete understanding of the SSE effect has not been realized yet, various different theoretical models have been proposed to interpret the effect.[100,101,102,103,104,105] Among the early models, the one attracting slightly more interest is the so-called magnon-driven SSE model proposed in Ref. [100]. The essence of this model is that the magnon subsystem in a ferrimagnet can become thermalized internally before it equilibrates with the phonon subsystem. As a result, the spatial distribution of the magnon temperature T_m in the ferrimagnet deviates from that of the phonon temperature T_p, although the average of T_m may be the same as that of T_p. This temperature distribution difference can further result in a difference between T_m in the ferrimagnet and the electron temperature T_e in a neighboring heavy metal at the interface and a corresponding pure spin current in the heavy metal.

More recent models include those proposed in Refs. [101-104]. Specifically, the authors in Ref. [101] studied the origin of the SSE using the stochastic Landau-Lifshitz theory and identified several length scales that govern the SSE strength. According to their model, the magnons in the ferrimagnet film establish a non-equilibrium steady state by equilibrating with phonons in the ferrimagnet via bulk damping and electrons in the neighboring heavy metal via interfacial spin pumping. In parallel, the authors in Ref. [102] analyzed the SSE phenomenon through microscopical calculations using the Boltzmann equation of the magnons. In their model, the

[101] J. Xiao, G. E. W. Bauer, K. Uchida, E. Saitoh, and S. Maekawa, Phys. Rev. B **81**, 214418 (2010).
[102] S. Hoffman, K. Sato, and Y. Tserkovnyak, Phys. Rev. B **88**, 064408 (2013).
[103] S. M. Rezende, R. L. Rodríguez-Suárez, R. O. Cunha, A. R. Rodrigues, F. L. A. Machado, G. A. Fonseca Guerra, J. C. Lopez Ortiz, and A. Azevedo, Phys. Rev. B **89**, 014416 (2014).
[104] U. Ritzmann, D. Hinzke, and U. Nowak, Phys. Rev. B **89**, 024409 (2014).
[105] A. Kehlberger, U. Ritzmann, D. Hinkzke, E. Guo, J. Cramer, G. Jakob, M. C. Onbasli, D. Kim, C. A. Ross, M. B. Jungfleisch, B. Hillebrands, U. Nowak, and M. Kläui, Phys. Rev. Lett. **115**, 096602 (2015).

temperature gradient leads to the generation of the magnons in the bulk of the ferrimagnet, and the magnon spin current into the metal is needed to ensure the continuity of the spin flow at the ferrimagnet/heavy metal interface. Lastly, the model described in Refs. [103] and [104] takes into account the linear dependence of the SSE strength on T_m-T_p in the ferrimagnet near the interface[100] and considers the decay of T_m-T_p with a certain characteristic length scale from the interface into the bulk of the ferrimagnet. Although proposed separately, these models all involve magnon flows across the ferrimagnet thickness and emphasize the bulk origin of the SSE. The bulk origin is supported by SSE experiments using ferrimagnet films of different thicknesses.[102,104]

The four models mentioned above also engage the magnetic damping (α) in the ferrimagnet film as a critical ingredient of the SSE, though in very different ways. In detail, in the model proposed in Ref. [100] the spin current pumped from the ferrimagnet to the heavy metal is inversely proportional to $1+\alpha^2$. The characteristic length scales identified in the model in Ref. [101] all depend on α. In the model in Ref. [102], the spin current into the heavy metal increases with a decrease in the magnon relaxation rate, while the latter increases with α. Finally, the model in Ref. [104] predicts an increase and subsequent saturation of the SSE signal with an increase in the ferrimagnet thickness, and this characteristic behavior shows a rather strong α dependence. In spite of these theoretical aspects, however, there have been no experiments on the effects of the damping on the SSE so far, to the best of my knowledge.

This chapter reports the first experiments on the role of the damping in the SSE in $Y_3Fe_5O_{12}$ (YIG) thin films. The experiments used YIG films grown on $Gd_3Ga_5O_{12}$ (GGG) substrates by

sputtering.[106,107] The films showed very similar structural and static magnetic properties but rather different α values, resulting from careful control of fabrication conditions. In order to probe the strength of the SSE, a Pt capping layer was grown on each YIG sample. During the SSE measurements, the temperature on the Pt side of the sample was kept constant, while that at the GGG side was changed to realize a temperature difference (ΔT) across the sample thickness. Owing to the presence of ΔT, the SSE takes place and produces a pure spin current in the Pt layer. Via the inverse spin Hall effect (ISHE),[108,109,110] the spin current then produces an electric voltage (V) across one of the lateral dimensions of the Pt layer. The SSE-produced voltage V was measured as a function of ΔT. The data show that the slope of the V vs. ΔT response increases with a decrease in α. This indicates that the smaller the damping is, the stronger the SSE is. This result is qualitatively consistent with the theoretical models proposed in Refs. [100, 102, 103 , 104]. Further, the SSE coefficient vs. α response shows almost linear behavior, which was not predicted explicitly in previous studies and therefore calls for new theoretical investigations. The experiments also indicate that the SSE strength shows no notable dependences on the enhanced damping due to spin pumping at the YIG/Pt interface. This can be understood in the frame work of the models described in Refs. [100] and [104].

[106] T. Liu, H. Chang, V. Vlaminck, Y. Sun, M. Kabatek, A. Hoffmann, L. Deng, and M. Wu, J. Appl. Phys. **115**, 17A501 (2014).
[107] H. Chang, P. Li, W. Zhang, T. Liu, A. Hoffmann, L. Deng, and M. Wu, IEEE Magn. Lett. **5**, 6700104 (2014).
[108] J. E. Hirsch, Phys. Rev. Lett. **83**, 1834 (1999).
[109] S. O. Valenzuela and M. Tinkham, Nature **442**,176 (2006).
[110] A. Hoffmann, IEEE Trans. Magn. **49**, 5172 (2013).

7.1 **Sample Characteristics**

The YIG films were grown on 0.5-mm-thick (111) GGG substrates by RF sputtering. The general details on the growth, structure, and static magnetic properties of the films are provided in

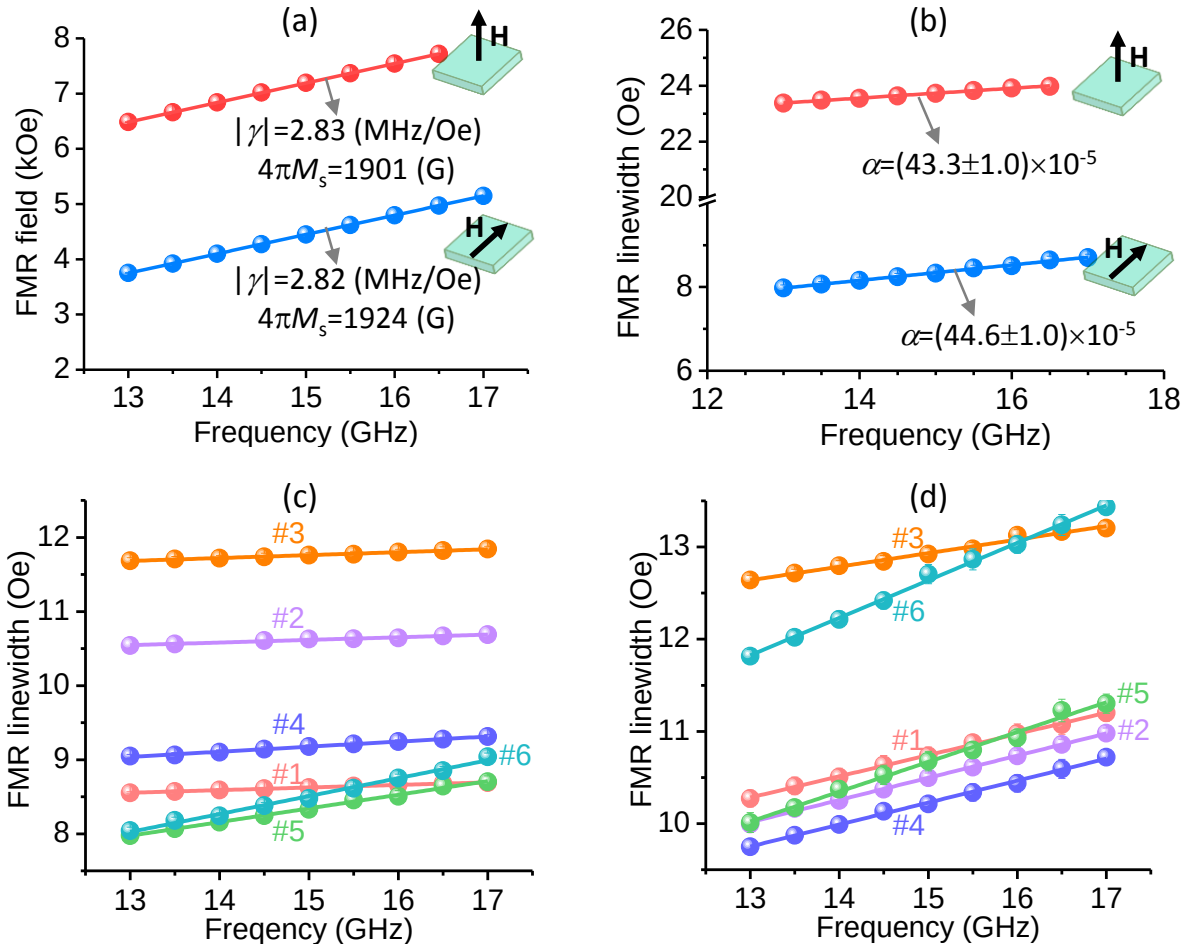

Figure 7.1 FMR properties of bare YIG thin film samples and YIG/Pt bi-layered samples. Graphs (a) and (b) show the FMR field and linewidth, respectively, as a function of frequency for two different field (**H**) configurations for bare YIG film sample #5. The dots show the data, and the lines show the fits. The fitting-yielded parameters are also given. Graph (c) presents the FMR linewidth data (dots) and fits (lines) for six bare YIG film samples, while graph (d) presents the data and fits for the corresponding YIG films after the growth of a 5-nm-thick Pt capping layer.

Refs. [105], [106], and [111]. The Pt capping layers were grown by DC sputtering at room temperature and were all 5 nm thick. The main properties of the YIG and YIG/Pt thin film samples are given in Fig. 7.1 and Table I.

Figure 7.1 presents the ferromagnetic resonance (FMR) data. Figures 7.1(a) and 7.1(b) present the FMR field H_{FMR} and peak-to-peak linewidth ΔH, respectively, as a function of frequency f for bare YIG film sample #5 for two different field configurations. The dots show the data. The lines in Fig. 7.1(a) show fits to the Kittel equation. The gyromagnetic ratio $|\gamma|$ and effective saturation induction $4\pi M_s$ values in Fig. 7.1(a) were obtained from the fitting. The lines in Fig. 7.1(b) show fits to

$$\Delta H = \frac{2\alpha}{\sqrt{3}|\gamma|} f + \Delta H_0 \tag{7.1}$$

where ΔH_0 accounts for inhomogeneity linewidth broadening and does not represent a loss. The fitting-produced α values are also given in Fig. 7.1(b). From Figs. 7.1(a) and 7.1(b), one can see that the $|\gamma|$, $4\pi M_s$, and α values obtained for the field-in-plane configuration are almost the same as those obtained for the out-of-plane configuration. This consistency clearly shows the reliability of the FMR results obtained with either field configuration. Further, the consistency of the α values for the two field configurations indicates that the contribution of two-magnon scattering to α is negligible in the sputtered YIG films. In the case that two-magnon scattering

[111] E. Jakubisova-Liskova, S. Visnovsky, H. Chang, and M. Wu, J. Appl. Phys. **117**, 17B702 (2015).

occurs, one would expect the α values measured with in-plane fields to be notably larger than those measured with out-of-plane fields.[112,113]

Figure 7.1(c) presents the ΔH vs. f data for six bare YIG film samples. As in Fig. 7.1(b), the dots show the ΔH data and the lines show the fits to Eq. (7.1). One can see that all of the six sets of data can be fitted very well. The fitting-yielded damping values, termed as α_{YIG}, are listed in Table I. Figure 7.1(d) shows the ΔH vs. f data, in the same format as in Fig. 7.1(c), for the YIG samples after the deposition of a Pt capping layer. One can see that the growth of a Pt layer not only enhances ΔH but also results in notable increases in the slopes. As in Fig. 7.1(c), all of the six sets of data in Fig. 7.1(d) can be fitted very well. The fitting-yielded damping values, termed as $\alpha_{YIG/Pt}$, are given in Table I. Note that the data in Figs. 7.1(c) and 7.1(d) were measured with in-plane fields.

Table I. Properties of six YIG thin film samples before and after the growth of a 5-nm-thick Pt capping layer.

Sample	#1	#2	#3	#4	#5	#6
d (nm)	23.4	23.4	23.4	23.4	19.7	22.3
$4\pi M_s$ (G)	1820	1956	1757	1827	1924	1913
α_{YIG} ($\times 10^{-5}$)	8.5±0.2	8.7±0.5	9.4±0.3	16.5±0.3	45±1	59±2
$\alpha_{YIG/Pt}$ ($\times 10^{-5}$)	55.8±0.8	58.4±0.8	35±1	58±1	77±2	99±2
α_{sp} ($\times 10^{-5}$) ($=\alpha_{YIG/Pt}-\alpha_{YIG}$)	47.3	49.7	25.6	41.5	32	40

Table I lists the fitting-yielded $4\pi M_s$, α_{YIG}, and $\alpha_{YIG/Pt}$ values as well as the YIG film thickness (d) values of the six samples. It is evident from Table I that the six YIG films have very similar thicknesses and comparable $4\pi M_s$ values, but their α_{YIG} values differ by a factor of about 7. Since

[112] R. D. McMichael and P. Krivosik, IEEE Trans. Magn. **40**, 2 (2004).
[113] P. Krivosik, N. Mo, S. Kalarickal, and C. E. Patton, J. Appl. Phys. **101**, 083901 (2007).

magnon-electron scattering does not occur in insulators, two-magnon scattering is negligible as discussed above, three-magnon scattering is prohibited as the FMR frequency is relatively high, and four-magnon scattering is relatively weak due to low microwave power (≤3 dBm) in the FMR measurements, one can conclude that α_{YIG} denotes the intrinsic magnetic damping in the YIG film and results mainly from magnon-phonon scattering. Note that the magnon-phonon scattering refers to a relaxation process in which a magnon is annihilated and a phonon is created and by which the energy of the magnons dissipates into the lattice of the material. This relaxation process is intrinsic and universal, and is usually non-trivial in magnetic insulators but is over-dominated by magnon-electron scattering in ferromagnetic metals.

Considering the facts that the six YIG films exhibit very similar structural and static magnetic properties but show very different damping (α_{YIG}), one can conclude that the films constitute a good system for exploring the role of damping in the SSE. The difference in α_{YIG} is likely due to the difference in the microstructure properties of the YIG films. What's more, there exists a clear correlation between the YIG surface texture and the α_{YIG} value. It is believed that the YIG films with different surface textures exhibit dissimilar granular properties, while the dissimilarity in the surface morphology and grain properties gives rise to a difference in the level of magnon-phonon coupling and a corresponding variation in α_{YIG}. The fact that the films show different surface morphology is because they were prepared under different sputtering and annealing conditions.

After the growth of a Pt capping layer, however, the damping in the YIG also contains a contribution due to spin pumping from the YIG to the Pt. As a result, the damping consists of two components, namely, $\alpha_{YIG/Pt}=\alpha_{YIG}+\alpha_{sp}$, where α_{YIG} describes the contribution from the relaxation in the bulk of the YIG and α_{sp} describes the interfacial spin pumping contribution. It is fortunate that these two components, α_{YIG} and α_{sp}, can be separated, as listed in row 4 and row

6 in Table I, facilitating the examination of the effects of each component on the SSE, as discussed shortly. Note that α_{sp} can be considered as a result of the coupling between the magnons in the YIG and the electrons in the Pt; it should also contain a contribution from the coupling of the magnons to the phonons in the Pt, but this contribution is expected to be much weaker than that of the magnon-electron coupling at the interface.

7.2 Experimental Configuration and Results

Turn now to the SSE experiments on the YIG/Pt samples. Figure 7.2(a) shows a schematic of the experimental setup. During the SSE measurement, an external field of about 930 Oe was applied in the plane of and perpendicular to the length of the YIG/Pt strip. The temperature on the Pt side of the YIG/Pt sample, T_{Pt}, was kept constant, while temperature on the GGG side of the sample, T_{GGG}, was varied. When the difference $\Delta T=T_{GGG}-T_{Pt}$ is non-zero, the SSE occurs in the YIG film and produces a pure spin current flowing into the Pt layer. The spin current then gives rise to a measurable voltage V across the length of the Pt strip via the ISHE.[108,109,110] Note that the purpose of keeping T_{Pt} constant is to minimize the change of the average temperature in the YIG film and thereby to avoid the effects due to the change of the absolute temperature.

Figures 7.2(b), 7.2(c), and 7.2(d) give SSE data obtained with YIG/Pt sample #1. Figure 7.2(b) presents the T_{Pt} and T_{GGG} data, while Fig. 7.2(c) presents ΔT (left axis) and the corresponding V data (right axis). One can see that during the measurements T_{Pt} was kept constant at 15.5 °C, T_{GGG} was varied over a range of 15-33 °C, and V changed in the almost same manner as ΔT.

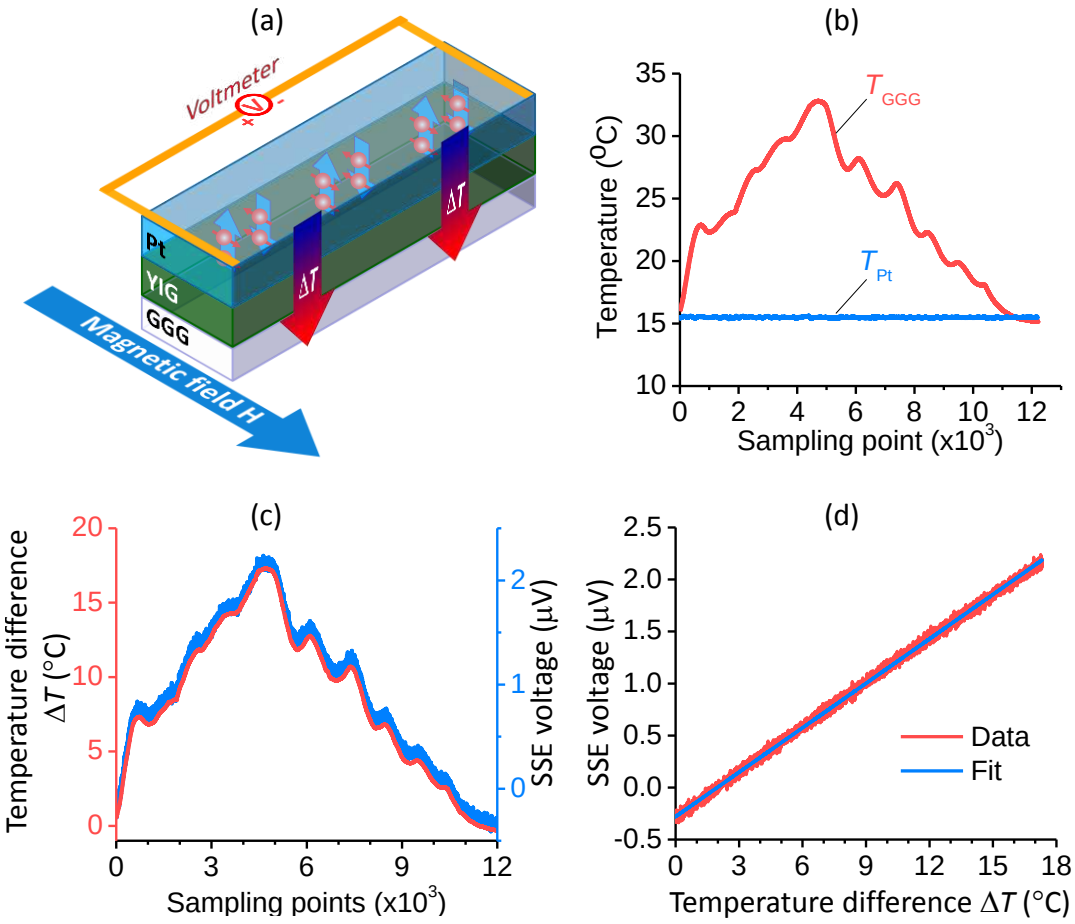

Figure 7.2 SSE measurements. Graph (a) shows a schematic of the experimental setup. Graphs (b)-(d) give the data obtained with YIG/Pt sample #1. Graph (b) presents the temperatures on the Pt and GGG sides of the sample, T_{Pt} and T_{GGG}. Graph (c) presents ΔT ($=T_{GGG}-T_{Pt}$) and the corresponding voltage signal V. The horizontal axes in (b) and (c) show sampling points, and 1000 points correspond to a period of 4 minutes. Graph (d) shows the V vs. ΔT response plotted using the data in (c). The thin blue line in (d) shows a linear fit.

These results indicate that the voltage signal is associated with the temperature gradient in the YIG film, rather than the absolute temperature of the YIG or the Pt. Note that one can consider that the average temperature in the YIG was almost constant just as T_{Pt}, based on the fact that the GGG substrate (0.5 mm) is considerably thicker than the YIG film (≈20 nm). Figure 7.2(d) plots V as a function of ΔT, using the data in Fig. 7.1(c). The red coarse line consists of the experimental data points, and the blue thin line shows a fit. One can see that the V vs. ΔT response is almost

perfectly linear. This linear behavior is expected by all the three SSE models described in the introduction.[102, 103, 105]

7.3 Data Analyses and Discussions

Figure 7.3 presents the key results of this work. Figure 7.3(a) present the SSE-produced V as a function of ΔT for six YIG/Pt samples, as indicated. Figure 7.3(b) presents the linear fits to the data in Fig. 7.3(a). In Fig. 7.3(b) the y-axis intercepts are all removed for a better presentation. Those intercepts are independent of ΔT and are therefore not associated with the SSE. If one takes D as the sample thickness and L as the distance between the two electrodes (see Fig. 7.2(a)) and defines[114]

$$\xi_{\mathrm{SSE}} = \frac{\left(V/L\right)}{\left(\Delta T/D\right)} = \frac{V}{\Delta T}\frac{D}{L} \tag{7.2}$$

as the geometry-free SSE coefficient, one can then use the slope of the V vs. ΔT lines in Fig. 7.3(b) to determine the ξ_{SSE} values for different samples and thereby examine how ξ_{SSE} varies with the damping by plotting ξ_{SSE} as a function of α_{YIG} or α_{sp}. Such plots are presented in Figs. 7.3(c) and 7.3(d).

It is evident from the data in Fig. 7.3(c) that ξ_{SSE} increases with a decrease in α_{YIG}, indicating that the SSE is stronger if the damping is lower. This result is qualitatively consistent with and

[114] A. Sola, M. Kuepferling, V. Basso, M. Pasquale, T. Kikkawa, K. Uchida, and E. Saitoh, J. Appl. Phys. **117**, 17C510 (2015).

thereby supports the theoretical models proposed in Refs. [100,102 -104]. It is also consistent with simulation results presented in Ref. [104]. In terms of the model proposed in Ref. [100], the underlying physics for this result is that the damping in the YIG films originates mainly from magnon-phonon scattering as discussed above; the weaker the magnons are coupled to the phonons, the more T_m deviates from T_p at the YIG/Pt interface.

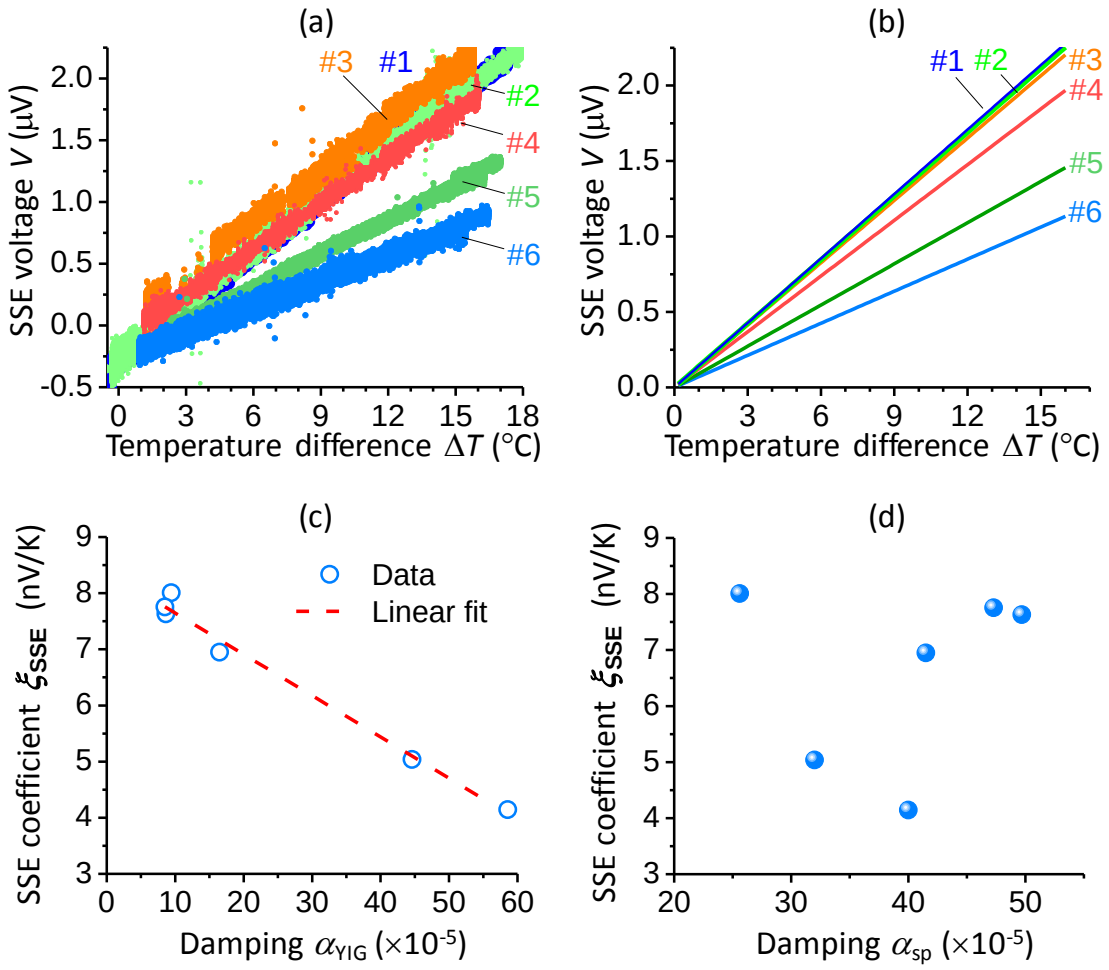

Figure 7.3 Graph (a) shows the SSE-produced voltage as a function of ΔT (=T_{GGG}-T_{Pt}) measured on six different YIG/Pt samples. Graph (b) shows the linear fits to the data in (a). Graphs (c) and (d) give the SSE coefficient, which is defined by Eq. (7.2), as a function of α_{YIG} and α_{sp}, respectively.

Note that previous work has demonstrated a good agreement between the simulations using this model and the experiments using YIG/Pt heterostructures.[115] In the terminology described in Refs. [102-104], the underlying physics is that the weaker the damping is, the more the magnons propagate from the bulk to the interface and contribute to the SSE signal. Further, the data in Fig. 7.3(c) also indicate that the ξ_{SSE} vs. α_{YIG} response shows quasi-linear behavior for the given damping range, as suggested by the dashed line. Understanding of this quasi-linear response calls for new theoretical studies.

In a stark contrast, the data in Fig. 7.3(d) do not show any obvious dependences of ξ_{SSE} on α_{sp}. This can be understood in the frame of the models described in Refs. [100] and [104]. Specifically, α_{sp} plays two roles in the process in which the SSE in the YIG produces spin currents in the Pt. On one hand, a larger α_{sp} value indicates a more efficient spin transfer at the YIG/Pt interface,[116] and one should expect larger spin currents in the Pt in samples with larger α_{sp}. On the other hand, the spin transfer at the YIG/Pt interface at the same time causes a decrease in the difference between T_m in the YIG and T_e in the Pt near the interface, resulting in a weaker SSE. One can see that these two roles are opposite, and as a result ξ_{SSE} does not show an explicit dependence on α_{sp}.

Two important points should be made about the above-presented results. First, the agreement of the results with the existing models is qualitative, and future quantitative theoretical analysis of the results is of great interest. Second, it is expected that similar results can be

[115] M. Schreier, A. Kamra, M. Weiler, J. Xiao, G. E. W. Bauer, R. Gross, and S. T. B. Goennenwein, Phys. Rev, B **88**, 094410 (2013).

[116] B. Heinrich, C. Burrowes, E. Montoya, B. Kardasz, E. Girt, Y. Y. Song, Y. Sun, and M. Wu, Phys. Rev. Lett. **107**, 066604 (2011).

observed in other magnetic insulator/heavy metal heterostructures, while the results might be different in ferromagnetic metal/heavy metal heterostructures due to the facts that (1) in ferromagnetic metals magnon-electron scattering plays critical roles in the intrinsic damping and (2) the spin transfer at a ferromagnetic metal/heavy metal interface is significantly more efficient than that at a magnetic insulator/heavy metal interface.

7.4 Summary

In summary, the effects of the intrinsic damping in the YIG bulk (α_{YIG}) and the enhanced damping due to interfacial spin pumping (α_{sp}) on the SSE in the YIG/Pt bi-layered structures have been studied experimentally. The experimental data show that the lower the damping α_{YIG} is, the stronger the SSE is. This observation is consistent with some of the existing theoretical models. The SSE coefficient vs. α_{YIG} response is almost linear. This quasi-linear behavior was not predicted explicitly by previous models. The data also show no explicit dependence of the SSE on α_{sp}, which can be interpreted using the terminology of two existing models.

CHAPTER 8

Summary and Outlook

8.1 Summary and Conclusions

Four topics that are relevant to the fundamental understanding of physics and technological advancement for magnetization dynamics have been studied.

Foldover effect due to nonlinear spin wave eigenmodes in a feedback ring configuration was observed for the first time. The data were successfully modeled analytically, and an almost perfect match between the data and the theory was seen, consolidating the understanding of the phenomena. The analytical modelling of the foldover effect completes the mathematical description of yet another fascinating nonlinear effects seen in feedback ring systems.

This thesis also reports the first observation of dispersive shock waves in a spin wave system. This is also the first observation of an envelope dispersive shock wave which enables the extraction of phase information and can also be modeled with the nonlinear Schrödinger equation. This work has provided useful insight into the phenomena under different conditions such as different excitation powers and different power ratios between the strong and weak signals, which deepens the knowledge about the formation and propagation of a shock wave in dispersive media.

The final two projects are strongly connected to the newly developed area of technology called spintronics. Work presented in chapter 6 explores the spin pumping of surface spin waves in YIG films in a wide range of the frequency and a wide range of the magnetic field strength, as well as

in different nonlinear spin wave regimes. A clear nonlinear behavior in the produced ISHE voltage was observed and was qualitatively explained under the frame work of three-wave nonlinearities. The observed nonlinear behavior opens up a new degree of freedom for the future design and development of spintronic devices.

In chapter 7 the dependence of the SSE on the damping of YIG films is explored. The data provide critical information about the SSE and will help develop a complete mathematical description of the SSE, which is still lacking.

8.2 Future Work

Chapter 5 presents the first observation of dispersive shock waves for spin waves. While the experiment has provided comprehensive data which qualitatively agree with the existing theory, the numerical modelling of the data to obtain further understanding is of great interest. In chapter 4, the foldover of spin wave eigenmodes in a feedback ring system was observed. The observation of the same effect in surface spin waves and backward volume spin waves is of interest. In chapter 6, the nonlinear behavior of the spin pumping due to spin waves was studied. The nonlinear three-wave splitting was identified as the driving force behind the nonlinear behavior. For the best of my knowledge, still a complete mathematical model does not exist to explain the three-wave splitting process and the threshold power levels required in a wide frequency range. Future theoretical work to give a complete mathematical description to enable the quantitative analysis of the data, which are well explained qualitatively, is of great interest.